

Centrifuge Modelling of Permeability in a Heterogeneous Coal Mine Backfill Sequence

by

Warren Deon van Tonder

10091981



UNIVERSITEIT VAN PRETORIA
UNIVERSITY OF PRETORIA
YUNIBESITHI YA PRETORIA

Department of Geology

Faculty of Natural and Agricultural Sciences

University of Pretoria

Submitted in partial fulfilment of the requirements for the degree Master of Sciences

July 2015

Supervisors: Prof S.W. Jacobsz and Dr M.A. Dippenaar

Declaration and Acknowledgements

I, Warren Deon van Tonder, student number 10091981, declare that the dissertation, which I hereby submit for the degree Master of Sciences at the University of Pretoria, is my own work and has not been previously submitted by me for a degree at this or any other tertiary institution.

I would like to acknowledge the meaningful contributions made by the following individuals and institutions:

- Prof S.W.Jacobsz, thank you for your guidance, leadership and the extensive amount of knowledge you have shared. Your devotion to my investigation and patience throughout the research is truly appreciated and your experience has proved to be invaluable, the research would not have been possible without your input.
- Dr. M.A. Dippenaar, your guidance and input to my research is greatly appreciated, thank you for your patience and supervision throughout the investigation.
- Prof J.L. van Rooy and the University of Pretoria, thank you for the funding of my investigation and for providing me with the opportunity to use the facilities of the University, in particular the geotechnical centrifuge laboratory.
- Exxaro Resources Ltd, thank you for sponsoring my studies and providing me with the opportunity to continue my post graduate research, your input is duly acknowledged and I feel privileged to be part of your bursary programme.
- Mr H. Lingenfelder and his team at Exxaro Geosciences, in particular Mr R. Reyneke, Mr F. Koen and Mr G. Brink, thank you for your support and valuable input to my research.
- The Geology team at Leeuwpan Coal Mine, thank you for your patience and providing me with access to the mine and transport to the testing and sampling locations.
- Mr. P. Le Roux, your patience in assisting me with the pore pressure transducers and willingness to help was outstanding, the effective use of the transducers would not have been possible without your input and guidance, thank you.
- Mr. R. Kok and the centrifuge lab assistants, thank you for your patience and assistance, you were always there when needed and assisted me significantly in the centrifuge lab.
- Mr K. Roux for assistance with the field measurements at the mine, your assistance made the field permeability tests much more manageable.
- My parents, mom and dad thank you for your support and motivation throughout my studies, I could not have done this without you. You have both been inspirational role models to me and I thank you for always being there when I needed you.
- My beautiful Fiancé, thank you Willemien for all the drawings that you perfected and the long hours you devoted to assisting me with the editing of my dissertation, but most of all thank you for being there and supporting me whenever I needed you, I could not have done this without you.

Signature:

Date:

ABSTRACT

Opencast mining has been and continues to be a favoured method for the extraction of the vast coal reserves in the Highveld of South Africa. Previously backfilled and restored open cast areas are generally zoned for agricultural uses, but with growing pressures on land use, such areas are increasingly being considered for the expansion of infrastructure and regional development. Understanding the backfill permeability and hydraulic behaviour is therefore an important component in defining the land use restrictions placed on a previously backfilled area. Centrifuge modelling provides a means of better understanding the hydraulic behaviour and measuring the permeability of opencast backfill under controlled laboratory conditions. Based on a preselected backfill prototype, an appropriate centrifuge model was developed. Using miniature pore pressure transducers, the pore pressures were measured at discrete locations in the model during falling head tests in a geotechnical centrifuge. Using the measured volumetric discharge, spacing between the transducers and the measured pore pressures, the permeability of the backfill was calculated. Due to polarized opinions on the scaling of permeability in a centrifugal field, a control model was tested at 1g and 23g to validate this scaling law. It was demonstrated that the respective permeabilities calculated at 1g and 23g were effectively the same and that it is in fact the hydraulic gradient that is scaled N times in the centrifuge. Knowing this allowed the calculated centrifuge permeabilities to be directly related to the prototype represented by the model. To determine the accuracy of the centrifuge model, the results of field percolation tests were compared to the results of an analogous centrifuge model. There was no correlation between the results and it was not considered meaningful to compare the results, as the model and percolation test site (prototype) conditions differed significantly. To simulate the preselected prototype backfill sequence, a model configuration that represented the geometry and material properties of the prototype was tested at 35g (half scale) and 70g (full scale) in the centrifuge. The results of the centrifuge model were used to make reasonable predictions on the long term permeability and hydraulic behaviour of the backfill prototype. It was found that the permeability of the backfill is likely to decrease over time due to consolidation settlement. The bottom of the backfill sequence is expected to have the lowest permeability and the top is likely to maintain a higher permeability. It was further demonstrated that the horizon interfaces acted as flow restrictors and resulted in poor vertical permeability between the horizons in the backfill sequence. Overall the centrifuge methodology provided a unique and efficient means of modelling the long term permeability and hydraulic behaviour of the backfill sequence.

LIST OF ABBREVIATIONS

AEV = Air Entry Value

ASTM = American Standard Test Method

HAE = High Air Entry

HD = High Definition

LCM = Leeuwpan Coal Mine

MAP = Mean Annual Precipitation

PPTs = Pore Pressure Transducers

PSD = Particle Size Distribution

Re = Reynolds number

SANAS = South African National Accreditation System

SPI = Standard Practice Instruction

SSCM = Steady State Centrifuge Method

WMA = Water Management Area

TABLE OF CONTENTS

ABSTRACT	ii
LIST OF ABBREVIATIONS.....	iii
TABLE OF FIGURES.....	vii
LIST OF TABLES	x
1. Introduction	1
1.1. Background	1
1.2. Aim	2
1.3. Objectives.....	2
2. Literature Review	3
2.1. Seepage flow.....	3
2.1.1. The basic concepts of seepage flow.....	3
2.2. Hydraulic Behaviour and Settlement of Opencast Backfill.....	5
2.2.1. Introduction	5
2.2.2. Backfill settlement	5
2.2.3. Backfill hydraulic behaviour	7
2.3. Centrifuge Modelling.....	10
2.3.1. Concept of centrifuge modelling	10
2.3.2. Fundamental scaling laws	10
2.3.3. Water flow in a centrifugal field and associated scaling laws	12
2.3.4. Modelling permeability in a centrifuge.....	14
3. Study Area	19
3.1. Climate and Surface Water Drainage	19
3.2. Regional Geology	20
3.3. Hydrogeology	24
3.4. Backfilling Material and Typical Backfill Sequence.....	25
4. Materials and Methods.....	28
4.1. Field Methodology	28
4.1.1. Field permeability testing.....	28
4.1.2. Backfill material sampling	30
4.2. Laboratory Methodology	30
4.2.1. Grain size analysis	30
4.3. Centrifuge Model	31
4.3.1. Developing the centrifuge model	31
4.3.2. Model setup and construction.....	34



4.3.3. Instrumentation.....	38
4.3.4. Material preparation.....	41
4.3.5. Test configurations	42
4.3.6. Test procedures	45
4.4. Analysis Methods	47
4.4.1. Calculating field permeability from percolation test data	47
4.4.2. Processing pore pressure data and calculating model permeability.....	47
4.4.3. Calculation of centrifugal accelerations	49
5. Results.....	52
5.1. Particle Size Distributions	52
5.1.1. Control test material	52
5.1.2. Correlation test material	53
5.1.3. Top soil material	54
5.1.4. "Softs" material.....	55
5.1.5. Slurry material	56
5.1.6. Discard material	57
5.2. Field Percolation Tests	58
5.3. Centrifuge Tests	59
5.3.1. Control test.....	59
5.3.2. Correlation test.....	64
5.3.3. Modelling full scale profile	68
5.3.4. Validation of Darcy's law	80
6. Discussion.....	81
6.1. Particle Size Distributions	81
6.1.1. Control test material	81
6.1.2. Correlation material	81
6.1.3. Topsoil material	81
6.1.4. "Softs"material.....	82
6.1.5. Slurry.....	82
6.1.6. Discard material	82
6.1.7. Summary.....	83
6.2. Field Percolation Tests	84
6.3. Centrifuge Tests	86
6.3.1. Theoretical pore pressure responses	86
6.3.2. Control test.....	88

6.3.3. Correlation test.....	92
6.3.4. Modelling full scale profile	94
6.3.5. Summary.....	102
7. Conclusions	103
8. References.....	106
Appendix.....	A

TABLE OF FIGURES

Figure 1: The components of total settlement (Day and Wardle, 1996).	5
Figure 2: The resulting heterogeneity of backfill as a result of end-tipping backfilling procedures. (a) Gravity sorting of end tipped backfill material, with coarse material at the base and fine material at the top of the slope. (b) The typical systematic layering of an end-tipped backfill (Youger <i>et al.</i> , 2002).	8
Figure 3: Inertial stresses in a centrifuge model are induced by rotation about a fixed axis correspond to gravitational stresses in the corresponding prototype (Taylor, 1995).....	11
Figure 4: The SSCM apparatus used by Nimmo <i>et al.</i> (1992) to measure unsaturated permeability in a small centrifuge which has subsequently been implemented as ASTM DD6527 (Nimmo <i>et al.</i> , 1992).	15
Figure 5: Simplified cross-sectional view of the test configuration used by Nimmo and Mello (1991) to measure the permeability in a centrifuge through falling and constant head tests. r_x denotes the radius from the axis of rotation to a specific point in the assembly (Nimmo and Mello, 1991).	16
Figure 6: The centrifuge model assembly used by Singh and Gupta (2000).	17
Figure 7: Site locality and topographical map outlining the study area and illustrating local surface water features.	22
Figure 8: Regional geology map indicating the outline of the study area in red and the sample locations as green dots within the study area.	23
Figure 9: Open pit bench configurations and typical backfill sequence at LCM (SPI, 2014). ..	26
Figure 10: Map indicating the sample locations and position of the test-pit on a historically backfilled area (outlined in yellow). Image courtesy of Google Earth.	28
Figure 11: The Perspex tube seated in the auger hole as it was used for the percolation tests.	29
Figure 12: The Perspex cylinder model set-up.	33
Figure 13: Cross-sectional view of the centrifuge model assembly.	34
Figure 14: The Perspex cylinder that was used in the centrifuge model assembly with the Festo valves fitted and the positions of the filter, supports, sample top and gradations marked off.	35
Figure 15: (a) The foam lined ring clamp that was used to fix the support bars to the cylinder. (b) The support bar connected to the ring clamp and the 90° bracket. (c) The support system fixed to the strong box collar and attached to the cylinder, with the support bars at 90° from each other.	36
Figure 16: The 6 mm BB bullets enclosed in the A4 Bidim to form the filter.	37
Figure 17: The overflow system and its components. (a) Solenoid valves connected to the outlet valves and placed on concrete blocks in the annular space. (b) The flow configuration of the solenoid valves. (c) Elevation of external drainage pipe to 100 mm above the steel platform to maintain the water level in the annular space at the filter height. (d) The overflow collection tray being slotted into place underneath the model assembly on the centrifuge platform.	38
Figure 18: The University of Pretoria's geotechnical centrifuge in the enclosure at the Department of Civil Engineering (Jones, 2014).....	39
Figure 19: Components and construction process of the PPTs. (a) The HAE ceramic disc and pressure sensor. (b) HAE ceramic disc glued to the pressure sensor. (c) Electrical wires	

soldered to the back of the pressure sensor. (d) Complete PPT after curing of Loctite Hysol 94466 structural adhesive. The 10c coin used for scale has a diameter of 16 mm.40

Figure 20: The pore pressure transducer design. Figure extracted from Le Roux (2013).40

Figure 21: Pore pressure transducers being saturated and calibrated in the modified triaxial cell mentioned in Le Roux (2013).41

Figure 22: Control test configuration, with the PPT positions indicated by the respective numbers in the column.43

Figure 23: Correlation test configuration, with the PPT positions indicated by the respective numbers in the column.44

Figure 24: Full-scale test configuration, with the PPT positions indicated by the respective numbers in the column.44

Figure 25: Theoretical model configuration used to demonstrate the estimation of K from pore pressure data.48

Figure 26: Calculated pore pressures throughout the model for a constant acceleration (N_r) of 56G and a varying centrifuge acceleration (N_a) of 56G.51

Figure 27: The pore pressures of the varying centrifuge acceleration are adjusted to fit the plot for a constant acceleration (N_r) of 56 G by increasing N_a to 70G.51

Figure 28: Grading curve for the sand used in the control test (Jacobsz, 2013).52

Figure 29: Grading curve comparison between the site material and test material for the correlation test.53

Figure 30: Grading curve comparison between the site material and test material for the top soil.54

Figure 31: Grading curve comparison between the site material and test material for the "softs" material.55

Figure 32: Grading curve comparison between the site and test slurry material.56

Figure 33: Grading curve comparison between the site and test discard material.57

Figure 34: Recorded pore pressure data for the control test at a centrifuge acceleration of 23g, with the PPT positions illustrated by the diagram in the top right corner.59

Figure 35: Recorded pore pressure data for the control test at 1g, with the PPT positions illustrated by the diagram in the top right corner.61

Figure 36: Recorded pore pressure data for the correlation test at $N_r = 23g$, with the PPT positions illustrated by the diagram in the top right corner.64

Figure 37: Configuration of the correlation test after centrifugation.66

Figure 38: Recorded pore pressure data for the full scale test at 35g, with the PPT positions illustrated by the diagram in the top right corner.69

Figure 39: Recorded pore pressure data for the full scale test at 70g, with the PPT positions illustrated by the diagram in the top right corner.71

Figure 40: Configuration of the full scale test after the completion of both the 35g and 70g tests.73

Figure 41: Stratification of fine and coarse grained material observed in the top soil horizon.74

Figure 42: Particles observed on the bottom of the strongbox after completion of the full scale test.74

Figure 43: a) Fine grained layer of dark grey material covering the top of the sample, b) cross-section view of the mound that formed against the side of the cylinder, with grain sizes coarsening from the top down and laterally towards the centre of the mound, c) top view

demonstrating the crater-like appearance of the mound, d) the "feeder pipe" of the mound extending into the top soil horizon.75

Figure 44: Plume of carbonaceous material that had been forced up into the "softs" horizon.76

Figure 45: Cracks observed along the interface between the "softs" and top soil horizons. ...76

Figure 46: Plot of calculated h_{pz} and PPT elevation used to determine the h_{pz} of PPT 3.....77

Figure 47: Theoretical pore pressure distribution under hydrostatic conditions, illustrating both the hydrostatic pressure (h_{ps}) and total head (potential) (H_s) distributions.87

Figure 48: Theoretical pore pressure behaviour under steady state flow conditions, illustrating both the pressure (h_{pf}) and total heads (H_f) once steady state has been achieved after opening the outlet valves.87

Figure 49: a) Distribution of the calculated theoretical h_{ps} , measured h_{ps} and h_{pf} and b) distribution of H_s and H_f at 23g.89

Figure 50: a) Distribution of the calculated theoretical h_{ps} , measured h_{ps} and h_{pf} and b) distribution of H_s and H_f at 1g.89

Figure 51: a) Distribution of the calculated theoretical h_{ps} , measured h_{ps} and h_{pf} and b) distribution of H_s and H_f at 29g.93

Figure 52: a) Distribution of the calculated theoretical h_{ps} , measured h_{ps} and h_{pf} and b) distribution of H_s and H_f at 35g.95

Figure 53: a) Distribution of the calculated theoretical h_{ps} , measured h_{ps} and h_{pf} and b) distribution of H_s and H_f at 70g.96

LIST OF TABLES

Table 1: Scaling laws for various physical properties (Jacobsz, 2013).....	12
Table 2: Prototype horizon thicknesses and their scaled model thickness based on a centrifugal acceleration of 56.67G and a modelling height of 600mm	32
Table 3: Centrifuge input parameters.	45
Table 4: The respective centrifuge accelerations (N_a), average acceleration throughout the model (N_r) and simulated prototype height (h_p) for each test configuration.	46
Table 5: Calculation procedure used to determine the difference in total head between two PPTs in the sample, based on the configuration of Figure 25.	49
Table 6: Relative particle size fractions for the site and model material of the correlation test	53
Table 7: Relative particle size fractions for the site and model top soil materials	54
Table 8: Relative particle size fractions for the site and model "softs" materials	55
Table 9: Relative particle size fractions for the site and model slurry material	56
Table 10: Relative particle size fractions for the site and model discard material.....	57
Table 11: Calculated K values for the field percolation tests	58
Table 12: Pore pressures recorded for the control test at 23g.	60
Table 13: Pore pressures recorded for the control test at 1g.	61
Table 14: The recorded physical observations for the control tests at 23g and 1g.	62
Table 15: The calculated change in total head between each PPT for the control test at 23g	62
Table 16: The calculated change in total head between each PPT for the control tests at 1g	63
Table 17: Calculated permeability between each PPT for the 23g and 1g tests using the pore pressure data from the PPTs.....	63
Table 18: Calculated difference in K values between the 1g and 23g tests.....	64
Table 19: Pore pressures measured for the correlation tests.....	65
Table 20: The recorded physical observations for the correlation test	67
Table 21: The calculated change in total head between each PPT for the correlation test....	67
Table 22: Calculated permeability between each PPT for the correlation test using the pore pressure data from the PPTs.....	68
Table 23: Comparison of the calculated average for the field percolation tests and the permeability calculated for the model using the PPTs.....	68
Table 24: Measured pore pressures for the full scale test at 35g	70
Table 25: Measured pore pressures for the full scale test at 70g.	72
Table 26: The recorded physical observations for the full scale test at 35g and 70g.....	72
Table 27: The calculated change in total head between each PPT for the full scale test at 35g	77
Table 28: The calculated change in total head between each PPT for the full scale test at 70g	78
Table 29: Calculated permeability between each PPT for the 35g and 70g tests using the pore pressure data from the PPTs.....	79
Table 30: Comparison of the permeabilities calculated for the 35g and 70g test	79
Table 31: Calculated Reynolds numbers for each centrifuge test configuration.	80
Table 32: Comparison of the measured hydrostatic pore pressures at 1g and 23g.....	91



1. Introduction

1.1. Background

Opencast mining has been and continues to be a favoured method for the extraction of the vast coal reserves in the Highveld of South Africa. A consequence of opencast mining is the production of large mining voids which are subsequently backfilled with waste material and rehabilitated. Previously backfilled and restored open cast areas are generally zoned for agricultural uses, but with growing pressures on land use, such areas are increasingly being considered for the expansion of infrastructure and regional development. However, environmental and engineering concerns often place restrictions on the use of backfilled areas. In order for backfilled areas to be successfully developed, an intricate understanding of these restrictions is needed.

Of particular concern with previously backfilled opencast coal mines is the migration of contaminants from the backfill and the stability of the fill material. Both of these concerns are intricately linked to the permeability and hydraulic behaviour of the backfill material. The rate at which contaminants are transported from the backfill and the subsequent prediction of contaminant loads is critically influenced by the permeability and hydraulic behaviour of the backfill. The long term stability of backfill material is influenced by the collapse settlement. As mentioned by Day and Wardle (1996), rapid and unexpected collapse settlement is often the result of backfill saturation due to the recovery of groundwater. The permeability and hydraulic behaviour of the backfill will influence the rate at which the backfill is saturated and is critical to predict collapse settlement associated with groundwater recovery. Furthermore, backfill settlement will alter the permeability of the material, which once again has further implications for contaminant transport.

Understanding the backfill permeability and hydraulic behaviour is therefore an important component in defining the land use restrictions placed on a previously backfilled area. Due to the complexity and limited data associated with backfilled areas, research on their physical hydrology is rather limited (Younger *et al.*, 2002). To adequately understand the hydraulic behaviour and quantify the permeability of backfill, through site investigation techniques, would require significant financial and technical resources. Physical modelling of the backfill at a reduced scale, may provide an alternative means of replicating the backfill hydraulic behaviour and measuring the permeability of the fill material. To replicate the backfill as accurately as possible, a physical model would need to simulate the geometry, material properties and in-situ stresses present in a defined backfill prototype. To do so, one either needs to use a large physical model (prototype scale) or subject a smaller model to the same stress conditions experienced at a prototype scale. Although the latter approach often involves complex testing equipment and intricate testing procedures, it is the most commonly used approach. Small scale physical models offer the user maximum control of the boundary conditions and the tests are more repeatable and less costly than large scale tests (Culligan-Hensely and Savvidou, 1995). The geotechnical centrifuge has become a powerful tool in simulating self-weight (in-situ) stresses (Taylor, 1995). This allows for the in-situ stresses experienced in the real system to be reproduced in a comprehensive small scale model. Provided the model is proportionately scaled and one is aware of the assumptions made and

1. Introduction

their implications on the modelling results, then the model may ultimately be regarded as a representative simplification of the real system (prototype).

A representative centrifuge model may provide a means of better understanding the hydraulic behaviour and measuring the permeability of opencast backfill under controlled laboratory conditions. Although a centrifuge model could not completely replace a site investigation, it would provide valuable insight into the behaviour of opencast backfill. With a better understanding of the backfill behaviour, site investigations can focus on the key aspects identified by the centrifuge model and the use of financial and technical resources can be reduced.

In the context of this dissertation it should be noted that the term permeability has been used instead of hydraulic conductivity to describe the ease at which the medium can transmit a fluid (in this case water). These two terms are often used interchangeably across the various disciplines in earth sciences and engineering. Therefore, as the emphasis of the dissertation is on the properties of the medium, the term permeability has been used throughout the dissertation to ensure a universal understanding is maintained across multiple disciplines.

1.2. Aim

The aim of this investigation is to model the permeability and investigate the hydraulic behaviour of a vertically layered coal mine backfill sequence with a geotechnical centrifuge.

1.3. Objectives

The aim is addressed through:

- I. Developing a representative geotechnical centrifuge model of the backfill sequence to measure the permeability between discrete points in the backfill sequence.
- II. Validating the centrifuge test methodology and scaling laws associated with the modelling of permeability in a centrifuge.
- III. Assessing the reliability of the centrifuge methodology in simulating specific prototype conditions.
- IV. Investigating the hydraulic behaviour of the backfill through the interpretation of the modelling results.
- V. Establishing if and how the results of the centrifuge tests can be related to an actual coal mine backfill sequence.



2. Literature Review

2.1. Seepage flow

As the research is concerned with modelling the permeability of porous backfill material, the basic concepts of fluid mechanics for porous media need to be understood. These concepts are referred to throughout the research and the following section aims to provide a brief overview of these concepts. The principle of seepage flow is discussed and the governing laws and associated formulae have been highlighted.

2.1.1. The basic concepts of seepage flow

Seepage is the term used to describe the movement of pore water through a porous material. This movement or flow is driven by a difference in mechanical energy and flow is initiated from an area of high mechanical energy towards an area of low mechanical energy. As stated by Fetter (2001), the total mechanical energy at a point is known as the hydraulic head (H), herein referred to as the total head and can be described by the Bernoulli equation. The total mechanical energy per unit weight of water is therefore the sum of the pressure head (h_p), elevation head (h_z) and velocity head (h_v). However, natural seepage velocities are small enough to be omitted so that the total head is given by Equation 1:

$$H = h_p + h_z \quad (1)$$

Expanding Equation 1:

$$H = \frac{u}{\gamma_w} + z \quad (2)$$

where, u is the pore water pressure, γ_w the unit weight of water and z (m) the elevation of the water above a chosen datum (Knappett and Craig, 2012 and Fetter, 2001)). The units of Equation 2 are length (L) units and the total head is thus conventionally given in meters (m) above a chosen datum. For a saturated porous medium, Bear (1972) states that, when a fluid is at rest, hydrostatic conditions prevail and the total head will be constant at each point within the medium. In the case of seepage flow, the elevation of the water table (phreatic surface) is taken as the total head under hydrostatic conditions. However, for a moving fluid the total head varies as a function of space and time (Bear, 1972). Differences in the hydraulic head from one point to another, results in a hydraulic gradient (i) and seepage will take place from areas of higher total head towards areas of lower total head (down gradient).

Seepage flow through a fully saturated porous medium is described by Darcy's law (Equation 3). According to the sand column experiments of Darcy, the volumetric discharge (Q) is a function of the permeability (K), i and the cross-sectional throughflow area (A).

$$Q = K \cdot i \cdot A = -K \frac{\Delta h}{\Delta l} A \quad (3)$$

The negative symbol denotes a decrease in head along the flow path. The permeability (or coefficient of permeability) is given in units of velocity (L/T) and is a measure of the resistance of a porous medium to the flow of water. As highlighted by Knappett and Craig (2012), K is

2. Literature Review

largely dependent on the size of the pore spaces within the porous medium. Hence, K is directly related to the particle size distribution, the shape of the particles and the manner in which these particles are arranged in the porous medium (structure). Fine grained porous media have small pore spaces which results in greater adhesive forces between solid particles and pore water. This increases the frictional resistance to seepage flow and results in a lower permeability. Conversely, coarse grained porous media have larger pore spaces that minimise the surface area in contact with pore water. Therefore, cohesive forces between water molecules dominate whereby pore water can easily be mobilised and which results in a higher permeability (Knappett and Craig, 2012 and Fetter, 2001).

However, the permeability is as much dependant on the properties of the permeant as it is the properties of the porous medium. Temperature will have a direct effect on K as it alters the viscosity of water. As demonstrated by Equation 4, K is inversely proportional to the fluid dynamic viscosity (μ) and directly proportional to the intrinsic permeability (k) and unit weight of water:

$$K = \frac{kg\rho}{\mu} \quad (4)$$

Where, k (L^2) is an absolute coefficient depending on the characteristics of the porous medium only, ρ is the density of water and g is gravitational acceleration. Hence, K will decrease with an increase in dynamic viscosity at lower temperatures.

Darcy's law assumes that all flow is laminar where resistive viscous forces dominate at slow fluid velocities. When flow velocities increase, the inertial forces are great enough to overcome the resistive viscous forces and the flow is said to be turbulent. Hence at high fluid velocities turbulent flow dominates and Darcy's law is invalid. To determine whether flow is laminar or turbulent four factors are related in the calculation of the Reynolds number (Equation 5). For Darcy's law to be valid, Fetter (2001) states that the Reynolds number (Re) should be less than 1 to 10. In most cases seepage flow in porous media is slow enough for Darcy's law to be valid, except where there are large cavities/fractures or steep hydraulic gradients (Fetter, 2001).

$$Re = \frac{\rho vd}{\mu} \quad (5)$$

Where ρ is fluid density, v is the specific discharge, and d is the characteristic microscopic length of the medium (effective particle size).

2.2. Hydraulic Behaviour and Settlement of Opencast Backfill

2.2.1. Introduction

It is of primary importance when reclaiming backfilled areas of opencast mines to understand the relationship between the hydraulic behaviour of the backfill and the prediction of backfill settlement. After the completion of backfilling procedures, groundwater recovery and infiltration of surface water is likely to influence the settlement characteristics of the backfill. The extent of this influence is said to depend on the post-mining hydraulic environment and the permeability of the backfill (Hills, 1994). On the other hand, the densification of the backfill due to settlement results in a consequent reduction of the backfill permeability at the same time (Younger *et al.*, 2002). Hence, the hydraulic behaviour and settlement characteristics of a backfill are interlinked and their influence on the reclamation of backfilled areas cannot be separated. Based on the reviewed literature, the following section will investigate this relationship through a discussion of backfill settlement mechanisms and backfill hydraulic behaviour.

2.2.2. Backfill settlement

After placement into the mining void, backfill will settle over time. As described by Hills (1994) and Day and Wardle (1996) the total settlement of backfill can be sub-divided into three components. These three components, as depicted by Figure 1, are known as consolidation, collapse and creep settlements respectively.

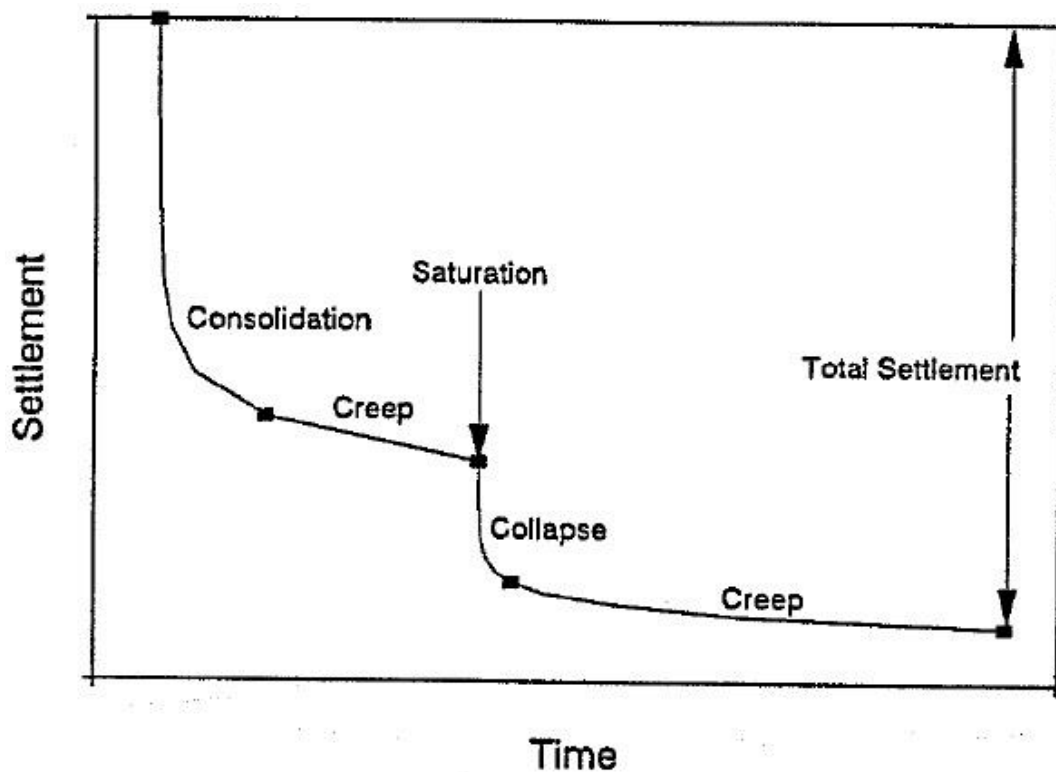


Figure 1: The components of total settlement (Day and Wardle, 1996).

2. Literature Review

As illustrated by Figure 1, the fill is initially expected to undergo time dependant consolidation settlement. According to Day and Wardle (1996) and Knappett and Craig (2012) consolidation settlement occurs in response to a change of the effective stress within the fill material due to the dissipation of excess pore pressures under an applied load. In simple terms, the application of a load (external or self-weight) to saturated materials is initially carried by the pore water and results in an excess pore water pressure within the material. In order to dissipate the excess pore water pressures some pore water must drain from the pores. Upon the drainage of some pore water, the load is transferred from the pore water to the intact material (soil skeleton), which results in an increase in the effective vertical stress and a subsequent reduction in volume (settlement). The rate of consolidation depends on the rate at which the excess pore pressures can be dissipated through drainage. As highlighted by Knappett and Craig (2012), the rate of consolidation is a function of the material permeability. Therefore, as a material with a greater permeability will drain rapidly, such materials will consolidate rapidly under an applied load. Conversely, pore water will drain slowly from a material of lower permeability and consolidation will occur over a longer period of time (Knappett and Craig, 2012)

With respect to opencast backfill, Day and Wardle (1996) state that "the bulk of the consolidation settlement occurs shortly after placement or after any change in applied load". This is demonstrated by Figure 1 where consolidation only occurs in the initial stages of settlement. Hence, for backfilled material that has been in place for many years, consolidation under self-weight would already have occurred and any further consolidation will be the direct result of changes in the applied load (construction on the backfill) (Day and Wardle, 1996).

The second component of total settlement that occurs under constant moisture content and stress conditions is known as creep settlement (Hills, 1994; Day and Wardle, 1996). Creep settlement is a slow process that according to Day and Wardle (1996) generally decreases logarithmically over time. Through compressive forces crushing the contacts between solid particles in the backfill, Hills (1994) describes creep as a "gradual rearrangement" of the fill material. The crushing of intact material results in the displacement of fine fragments and consequently causes a reduction in voids (volume). Although creep is a very slow process the production of fine fragments that may reduce the overall permeability of the backfill should not be overlooked.

The third component of total settlement is known as collapse settlement and is associated with a change in moisture content under constant stress conditions (Hills, 1994; Day and Wardle, 1996). As described by Day and Wardle (1996), collapse settlement is a result of an increased moisture content softening the inter-particle contacts. Consequently, backfill particles are rapidly rearranged into a denser packing, thus reducing the amount of voids within the fill. In comparison to consolidation and creep settlement, collapse settlement occurs rapidly and accounts for a large portion of the total backfill settlement. Thus, the prediction of increased moisture contents is critical to the prediction of backfill settlement due to collapse.

Increased moisture content in opencast backfill is associated with groundwater recovery after cessation of dewatering exercises and the infiltration of surface water into the backfill. As mentioned by Ferguson (1984) the panning and soils handling processes tend to

render backfill "impenetrable" to surface water. Hence, groundwater recovery is in most cases the main source of increased moisture contents in opencast backfill. As stated by Charles *et al.* (1984) and demonstrated in Figure 1, backfill settlement decreases rapidly with time to reach a fairly constant rate. However, upon saturation due to the recovery of groundwater, a sudden increase in the rate of settlement is observed. Consequently, backfill that may have been placed many years ago will suddenly experience large amounts of collapse settlement due to rising groundwater. An understanding of backfill hydraulic behaviour is therefore critical for the prediction of collapse settlement associated with groundwater recovery.

2.2.3. Backfill hydraulic behaviour

As highlighted by Younger *et al.* (2002), studies have generally focused on the geochemistry of backfill and research on the physical hydrology of backfill is rather limited. However, it is clear that the hydraulic behaviour of backfill materials differs greatly from that of the parent material. This is ultimately a consequence of the intrinsic physical and sometimes chemical changes of the material that occur during backfilling procedures and after fill placement. To understand the nature of flow through backfill, the influence of the material properties, backfilling method and the instability of the backfill after placement need to be examined (Hills, 1994; Younger *et al.*, 2002).

The material properties depend on the source rock and will vary accordingly. However, backfilling procedures involve the break-up of intact rock which produces a large amount of fine material. This increase in fine material may potentially control the overall permeability of the backfill material. Kenny *et al.* (1984) demonstrated that the permeability of granular materials was primarily dependant on the sizes of the particles in the fine fraction of the particle size distribution. Therefore, the increased percentage of fines in backfill may clog the pore space between larger particles and result in a reduced permeability. This is particularly evident in coal mine backfills with large quantities of shale clasts. Younger *et al.* (2002) highlight that shale clasts are likely to rapidly weather through slaking and abrasion when handled during backfilling procedures. This disintegration of the shale clasts results in a significant amount of fines being released into the backfill that may form mud and reduce the overall permeability.

The backfilling methods used to rehabilitate an opencast mine have been demonstrated to have a significant impact on the flow behaviour of the backfill. Younger *et al.* (2002) attribute the wide range of backfill permeabilities to the heterogeneity of the sediment fabric caused by end tipping backfilling methods. As illustrated by Figure 2a the backfill is gravity sorted as it rolls down a heap after being end-tipped. Large boulders and cobbles roll down the heap and accumulate at the foot of the heap, whereas the finer sediment is accumulated at the top of the slope. Through repeated end tipping an inclined accumulation of systematically graded layers as illustrated by Figure 2b may form (Younger *et al.*, 2002).

This artificial layering results in a type of structured heterogeneity in permeability throughout the backfill. As explained by Ferguson (1984) and Younger *et al.* (2002) the lower portions of the backfill generally have higher permeabilities due to the greater proportion of coarse material in this zone. Conversely, the upper portions of backfill are likely to have lower permeabilities due to a greater proportion of fine material and compaction from surface machinery. As a result of this layering in permeabilities, the vertical permeability (K_{vert}) between

2. Literature Review

individual layers in the backfill is generally poor. Hence, lateral flow dominates and preferential flowpaths develop along zones of higher permeability. Provided the backfill is saturated, these preferential flowpaths are generally associated with the more permeable coarse layers in the backfill. However, the entire backfill mass is unlikely to be completely saturated. In parts where the backfill is unsaturated/above the water table, Younger *et al.* (2002) suggest that the fine-grained layers will act as the preferential flow paths. As the fine-grained layers are capable of retaining more moisture than the coarser layers when unsaturated, they intrinsically have a higher unsaturated permeability (K_{unsat}). To put it in simple terms Younger *et al.* (2002) states that: "fine-grained spoil layers are preferential flowpaths in the unsaturated zones of spoil heaps" and "the coarse layers are the preferential flowpaths in the saturated zones of the spoil heaps".

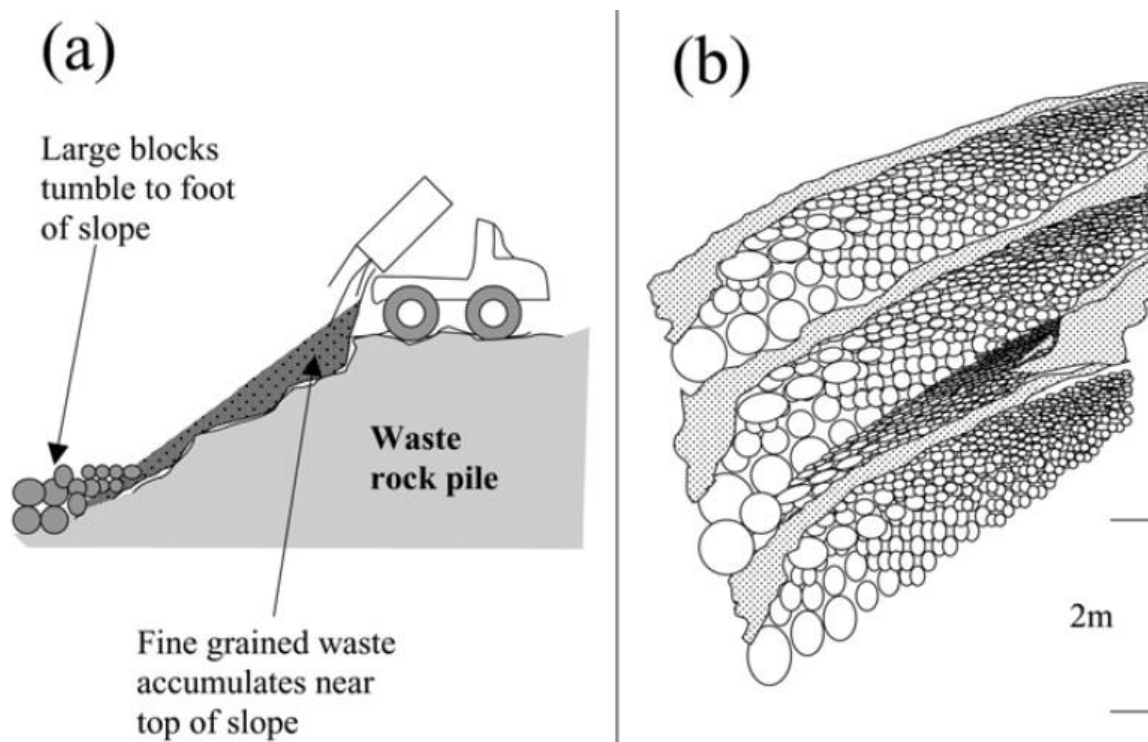


Figure 2: The resulting heterogeneity of backfill as a result of end-tipping backfilling procedures. (a) Gravity sorting of end tipped backfill material, with coarse material at the base and fine material at the top of the slope. (b) The typical systematic layering of an end-tipped backfill (Younger *et al.*, 2002).

Instabilities can influence the hydraulic behaviour of backfill through either physical (structural) or chemical changes to the backfill mass. As discussed in Section 1.2.2 backfill will undergo settlement after infilling into the mine void. Settlement results in a denser grain packing and subsequently reduces the void ratio of the fill mass. Additionally, the crushing and disintegration of weaker clasts produces fine-grained sediments that may block pores and therefore further reduce the void ratio. Ultimately, a reduction in the void ratio causes an overall decrease in the permeability of the backfill mass. The decrease in permeability as a result of settlement can be quite significant. Younger *et al.* (2002) report a decrease of up to two orders of magnitude for coal mine backfills after only a year of settlement. Similar values are reported



2. Literature Review

by Hills (1994), where the permeability of and uncompacted backfill was found to decrease by an order of magnitude within seventeen months of infilling.

Contrary to the decrease in permeability caused by backfill settlement, piping of the fill mass results in exceptionally high permeabilities (Younger *et al.*, 2002). Faster flows in the coarser grained layers may result in the entrainment of silt and sand particles. Through gradual abrasion by these entrained particles, erosional pipes may develop within the backfill mass. These pipes are equated to the dissolution cavities of a karst aquifer and are said to impart "pseudokarstic" hydraulic character to the backfill (Younger *et al.*, 2002). The presence of these sub-surface features may not be evident on the surface of a fill and often results in higher than expected permeabilities. Hence, for a fill where the discharge rate is expected to decrease over time, the opposite may be true due to the development of backfill pipes. As with dissolution cavities, backfill pipes are also susceptible to collapsing, especially when moisture contents suddenly decrease or additional surface loads are applied. A collapsed pipe may form a depression on the surface of the backfill and diverts additional water that would have formed part of the surface runoff into the backfill. As discussed in Section 2.2.2 this addition of water may result in unexpected and unpredictable collapse settlement long after the completion of backfilling.

Another significant control on the hydraulic behaviour of backfill can be attributed to chemical instabilities. This is particularly evident in the backfills of opencast coal mines where there are high concentrations of pyrite. As the pyrite weathers, large amounts of iron are dissolved into the infiltrating water. As the water percolates through the backfill the dissolved iron is precipitated as ferric hydroxide at the interface between saturated and aerated fill material. Over time layers of ferric hydroxide start to build up and clog the pores of the fill, thereby reducing the overall backfill permeability. Eventually, the precipitation of ferric hydroxides may produce an impermeable layer of pedogenic material (known as a hard pan ferricrete) within the backfill. These hard pans prevent the downward percolation of water and result in the localised saturation of the backfill mass immediately above them. Prevented from seeping vertically through the hard pans, this perched water is forced to flow laterally towards the edges of the backfill where it can exit as a spring or seepage face. As a consequence of this increase in localised lateral flow, piping of the backfill above hard pans may occur. Should the hard pan be situated close to the surface of the backfill, the resulting lack of infiltration may result in the erosion of the backfill surface due to increased surface runoff. This results in the development of gullies which may expose the interior of the backfill to changes in moisture contents through the diversion of surface runoff. Again this has the potential to cause unpredictable backfill settlements (Younger *et al.*, 2002).



2.3. Centrifuge Modelling

In order to better understand natural phenomena, physical modelling is often considered to be a reliable approach for exposing the mechanisms of these phenomena. The aim of physical modelling is to predict and observe the behaviour of natural phenomena by replicating the phenomena as accurately as possible at a reduced scale. The geotechnical centrifuge has been widely used in the physical modelling of geo-phenomena and has become an important tool to understanding the intricacies of ground behaviour, contaminant transport and earthquakes to name but a few (e.g. Taylor, 1995; Madabhushi, 2015). The following section will investigate: the basic concepts of centrifuge modelling; the fundamental scaling laws; water flow in a centrifugal field; and the measurement of permeability in centrifuge models.

2.3.1. Concept of centrifuge modelling

In order to make meaningful extrapolations from small-scale physical models to full scale phenomena (prototype), a large degree of similarity should be shared between the two events (Taylor, 1995). The fundamental problem with modelling geotechnical phenomena is the simulation of the stress level and stress history (in-situ stresses) experienced by geo-materials below the earth's surface (Jones, 2014). Due to the self-weight of geo-materials, in-situ stresses change with depth and result in a distribution of stress levels and histories at depth. Therefore, Taylor (1995) states that it is critical to simulate the effect of self-weight stresses to achieve similarity between the model and prototype.

This is where geotechnical centrifuge models have come to the fore in simulating prototype conditions. When a model is rotated in a geotechnical centrifuge, it experiences a radial acceleration field many times greater than earth's gravity. Thus, the unit weight of the model is increased so that the prototype stress level and history is replicated in the model (Taylor, 1995; Chikatamarla *et al.* 2006). Hence, if the centrifuge model accurately represents the material properties and geometry of the prototype (Joseph and Einstein, 1988), the observed model behaviour can be successfully extrapolated to the full scale prototype event.

2.3.2. Fundamental scaling laws

In order to relate the observed model behaviour to the prototype phenomena, appropriate scaling laws are needed (Chikatamarla *et al.* 2006). The basic scaling law, as described by Taylor (1995), is based on achieving the same stress conditions in the model as would exist at a homologous point in the prototype. This is achieved by subjecting a model N times smaller than the prototype to an inertial acceleration field N times greater than earth's gravity (Figure 3). Provided that the prototype material is used in the model and the model is subjected to the same stress history as the prototype, then the vertical stress at depth h_m in the model will be identical to that in the corresponding prototype at depth h_{pr} (Taylor, 1995).

2. Literature Review

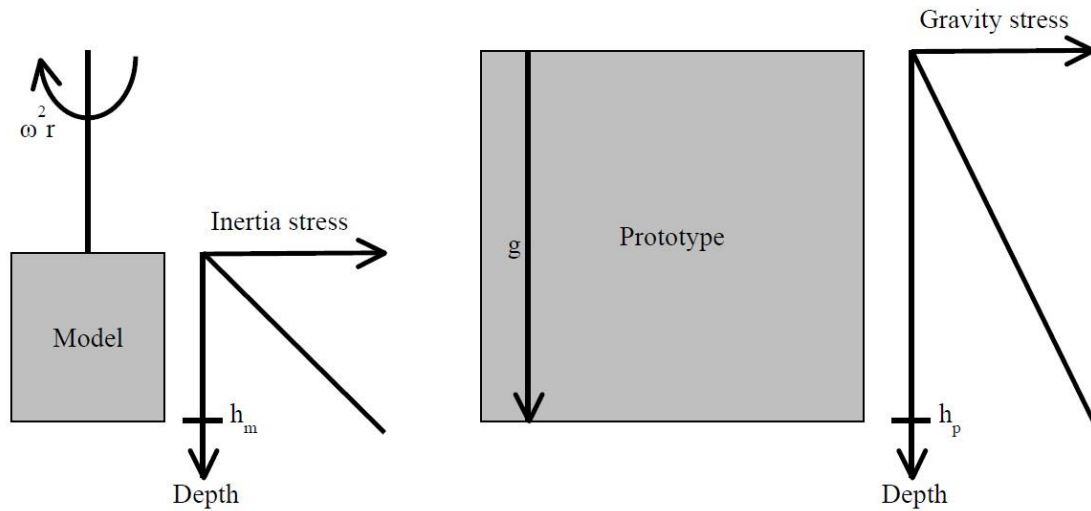


Figure 3: Inertial stresses in a centrifuge model are induced by rotation about a fixed axis correspond to gravitational stresses in the corresponding prototype (Taylor, 1995).

To illustrate this, Taylor (1995) demonstrates that if an acceleration of N times earth's gravity (g) was applied to a material with density ρ , then the vertical stress (σ_v) at depth h_m in the model can be determined by Equation 6.

$$\sigma_{vm} = \rho N g h_m \quad (6)$$

And at depth h_{pr} in the prototype:

$$\sigma_{vp} = \rho g h_{pr} \quad (7)$$

Subsequently if:

$$\sigma_{vm} = \sigma_{vp} \quad (8)$$

Then:

$$h_m = h_p N^{-1} \quad (9)$$

This is the basic scaling law of centrifuge modelling for linear dimensions. Thus, under ideal modelling conditions all linear dimensions will have a scaling factor of $1:N$ (model:prototype). As an example, to create the correct stress distribution in a model 100 times smaller than the prototype, the model will need to be accelerated to 100 times earth's gravity (Jacobsz, 2013).

Thus, by accelerating the model to a greater speed (increasing N), the modelling height needed to simulate the prototype can then be minimised. This would allow for a smaller model to be used in replicating the prototype. However, the behaviour of the model becomes difficult to measure and observe at smaller modelling heights. For this reason, Taylor (1995) suggests that most geotechnical centrifuge models adopt a larger modelling height and lower rotation speed.

Based on the scaling law for linear dimensions, scaling laws for other physical properties can be derived. Consolidation time, for example has a scaling factor of $1:N^2$

2. Literature Review

(Taylor, 1995). This means that the consolidation of a soil is accelerated by the elevated g field of the centrifuge, resulting in only a fraction of the prototype (actual) time needed to consolidate the model in the centrifuge. Hence, Taylor (1995) states that the rate at which time associated processes occur, appears to be accelerated in the centrifuge. This suggests that phenomena that take place over very long time periods can be simulated in a short modelling period when exposed to the elevated g field of the centrifuge.

Table 1 provides a summary of the scaling laws for some physical quantities (Jacobsz, 2013). Garnier *et al.* (2007) provides a complete catalogue of scaling laws for geotechnical centrifuge modelling and the reader is directed to this catalogue should they require more detail on scaling laws.

Table 1: Scaling laws for various physical properties (Jacobsz, 2013).

Property	Scale factor
Model scale	N
Acceleration (G)	N
Linear dimensions	$1/N$
Stress	1
Strain	1
Density	1
Mass	$1/N^3$
Force	$1/N^2$
Time (consolidation)	$1/N^2$
Time (dynamic)	$1/N$
Pore fluid velocity	N

2.3.3. Water flow in a centrifugal field and associated scaling laws

As with geometry and material properties of the model, the flow in a centrifuge model needs to be representative to that in the prototype. To achieve the required similitude between the model and prototype, the flow of water needs to be properly scaled (Nakajima and Stadler, 2006). As mentioned by numerous authors (Taylor, 1995; Dell'Avanzi and Zornberg, 2002; Thusyanthan and Madabhushi, 2003; Nakajima and Stadler, 2006) the primary scaling law for flow in a centrifuge is that of seepage velocity (v):

$$v_m = Nv_p \quad (10)$$

Therefore, the seepage velocity in the centrifuge model will be N times greater than in the prototype it represents (Taylor, 1995). As stated by Thusyanthan and Madabhushi (2003), this scaling law has been proven experimentally, assuming that the prototype soil has been used in the model and the soil is fully saturated (Taylor, 1995). As indicated by Table 1, the scaling factor for seepage velocity is 1: N (prototype: model).

However, when one considers the equation governing seepage flow (Darcy's law) two opposing issues arise. The debate deliberates whether the permeability (K) or the hydraulic gradient (i) is the fundamental parameter affected by gravity (Taylor, 1995; Thusyanthan and Madabhushi, 2003). Some consider K to be directly proportional to gravity and suggest that i is independent of gravity as it is dimensionless. According to Dell'Avanzi and Zornberg (2002), volumetric changes induced by the elevated stresses in a centrifuge alter the distribution (packing) of soil grains, which will intrinsically change the permeability (K) of the sample. Thus, if i is independent of gravity then $i_m = i_p$ and K is a function of the gravitational acceleration in the centrifuge. Based on this argument:

$$v_m = i_p N K_p = N v_p \quad (11)$$

which results in the scaling law for seepage velocity being satisfied. As outlined by Taylor (1995) and Thusyanthan and Madabhushi (2003) the problem with this argument is that soils would appear to be impermeable under zero gravity. This is due to the assumption of all seepage flow being gravity driven and at zero gravity there would not be any pressure gradient to induce seepage flow through the soil (Taylor, 1995).

However, based on the definition of hydraulic gradient (Equation 3) and considering that stresses are equal to the prototype but the lengths are condensed N times in the centrifuge, Taylor (1995) and Thusyanthan and Madabhushi (2003) propose that the hydraulic gradient is N times larger than in the prototype. This is a result of the change in head (Δh) having to occur over a length N times smaller than in the prototype. Therefore, i will be directly proportional to gravity with a scaling factor of N and K can be seen as a material constant ($K_m = K_p$) as displayed by Equation 12.

$$v_m = N i_p K_p = N v_p \quad (12)$$

From the above discussion it may seem irrelevant whether i or K is the fundamental parameter affected by the elevated acceleration field generated in a centrifuge, as both arguments still satisfy the scaling law for seepage velocity. However, when using centrifuge models to determine the permeability of soil material, it becomes important to understand the effect of centrifugation on both i and K in order to relate the modelling results to the prototype with the appropriate scaling laws.

A solution to the scaling of fluid flow in a centrifuge has been provided by Singh and Gupta (2002). The authors postulate that, "the centrifugation does not increase hydraulic gradient, it creates vertical and corresponding horizontal effective stresses by acceleration on the soil particles" (Singh and Gupta, 2002). Therefore, an effective stress regime equivalent to the prototype is generated in the model. This results in the lengths of both the water and soil columns in the model scaling uniformly, as the entire soil-water system experiences the same centrifugal acceleration (Singh and Gupta, 2002). Consequently, the change in water column length (Δl) over which the change in head (Δh) occurs in the model is equal to that of the prototype and results in a scaling factor of 1:1 ($i_m = i_p$) for the hydraulic gradient in the centrifuge (Singh and Gupta, 2002; Garnier *et al.*, 2007).

Based on the relationship between K and g , (Equation 4) Singh and Gupta (2002) demonstrate that K will be increased N times in the centrifuge if the same pore fluid and material is used:

$$\frac{K_m}{K_p} = \frac{\frac{k\rho g_m}{\mu}}{\frac{k\rho g_p}{\mu}} = \frac{g_m}{g_p} = N \quad (13)$$

Where K_p is the permeability at $1g$, g_p is gravitational acceleration and g_m is the centrifugal acceleration (Ng_p).

Hence, Equation 13 can be rewritten as:

$$K_m = NK_p \quad (14)$$

Equations 13 and 14 suggest that the self-weight of a fluid is increased N times in the centrifuge and as outlined by Singh and Gupta (2002), K is directly proportional to the unit weight of the permeating fluid (Equation 4). This results in a scaling factor of $1:N$ for K in the centrifuge (Singh and Gupta, 2002; Garnier *et al.*, 2007). Since $i_m = i_p$, Equation 11 is applicable and the scaling law for seepage velocity is satisfied.

In order for the scaling law of permeability to be applicable, Darcy's law needs to be valid for fluid flow in the centrifuge model. According to Culligan-Hensely and Savidou (1995) and Singh and Gupta (2002), laminar fluid flow needs to prevail in the model to ensure validity of Darcy's law. As demonstrated by Equation 5, the Reynolds number can be used to check the validity of Darcy's law. Provided that $R_e < 1$ fluid flow will be laminar and Darcy's law will be valid (Singh and Gupta, 2000). Hence, flow similarity between the model and prototype can be achieved by ensuring the Reynolds number does not exceed 1.

2.3.4. Modelling permeability in a centrifuge

2.3.4.1 Background

Conventional methods used to measure the hydraulic properties of soils rely on gravitational acceleration or an applied pressure gradient to drive flow through a sample. Such methods are often time consuming, tedious and limited to a small range of measurable K values (Simunek and Nimmo, 2005). By using a centrifuge to drive flow through a sample at N times gravitational acceleration, the measurement time is significantly reduced. Hence, as outlined by Nimmo *et al.* (1987), the range of measurable K values is increased considerably. Nimmo and Mello (1991) mention several advantages when using a centrifuge. Amongst these advantages are: the relatively simple flow apparatus used in experiments; the ability to simulate overburden pressures and the large measurement range for material with low K values.

Consequently, the centrifuge has been used in numerous research applications where conventional test methods have fallen short. The centrifuge has been particularly effective in the hydraulic characterisation of unsaturated soils. In particular unsaturated flow and the unsaturated permeability (K_{unsat}) of soils at low moisture contents have been extensively investigated by numerous researches (Nimmo *et al.*, 1987; Nimmo, 1990; Nimmo *et al.*, 1992;

2. Literature Review

Basha and Mina, 1999; Barry *et al.*, 2001; Simunek and Nimmo, 2005). Zornberg and McCartney (2010) have even gone so far as to develop a specialised centrifuge permeameter for the determination of soil water retention curves and K values for unsaturated soils. Other prominent research applications include the study of solute transport (Gamerding and Kaplan, 2000; Culligan-Hensley and Savvidou, 1995 to mention a few) and the estimation of recharge rates (Nimmo *et al.*, 1994).

As demonstrated, the centrifuge has proved to be an invaluable tool in understanding and measuring the hydraulic properties of geological mediums. The successes of centrifuge methods can be accredited to the development of the steady state centrifuge method (SSCM) of Nimmo *et al.* (1987). In their study, Nimmo *et al.* (1987) developed a centrifuge permeameter and test method that was used to measure K_{unsat} and validate Darcy's law for unsaturated flow in a centrifugal field. The permeameter and test methods have been subsequently refined (Nimmo *et al.*, 1992) and the SSCM method has been adopted as an American standard test method (ASTM DD6527) for unsaturated flow in a centrifuge. As demonstrated by Figure 4, the permeameter consists of a small (50 mm) soil sample space with ceramic discs at both ends. The sample is fitted into an assembly with a supply reservoir used to maintain a constant head as well as overflow and outflow reservoirs. The assembly is fitted into a 1 litre centrifuge bucket and accelerated up to 2000g in a small centrifuge (212mm arm radius). By measuring the change in weights of the various reservoirs Q can be determined and subsequently divided by the cross-sectional area of the sample to give the specific discharge (q). According to Nimmo *et al.* (1992) Darcy's law applies when q becomes constant and K can be calculated by dividing q by the driving centrifuge force. To determine when q becomes constant (steady state flow) the reservoirs were weighed after successive centrifuge runs until the measured weight for two successive runs were equal. (Nimmo *et al.*, 1987; Nimmo *et al.*, 1992).

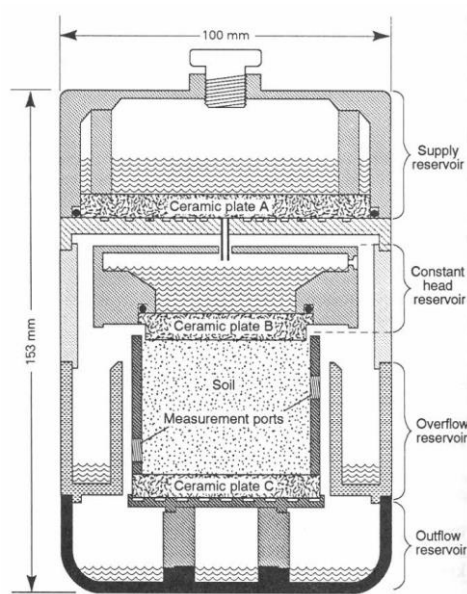


Figure 4: The SSCM apparatus used by Nimmo *et al.* (1992) to measure unsaturated permeability in a small centrifuge which has subsequently been implemented as ASTM DD6527 (Nimmo *et al.*, 1992).

2.3.4.2 Measuring permeability (K) in a centrifuge

2. Literature Review

As the aim of the present study is to measure K of a sample in a geotechnical centrifuge, two separate studies have been reviewed to gain a better understanding of the subject. Both studies provided valuable insight to the subject matter (measurement of K) and aided in the approach to the current investigation.

Using an adapted version of the SSCM apparatus (Figure 4) and similar methodology, Nimmo and Mello (1991) performed both falling and constant head tests on several fine textured samples in a centrifuge. Based on the simplified test configuration illustrated by Figure 5 the authors were able to calculate K for a constant head test as follows:

$$K = \frac{2qL}{\rho\omega^2(r_o^2 - r_{wa}^2)} \quad (15)$$

where: q is the specific discharge (as calculated by Nimmo *et al.*, 1992), L is the sample height ($r_b - r_t$), ρ is the density of water and ω the angular velocity of the centrifuge (Nimmo and Mello, 1991).

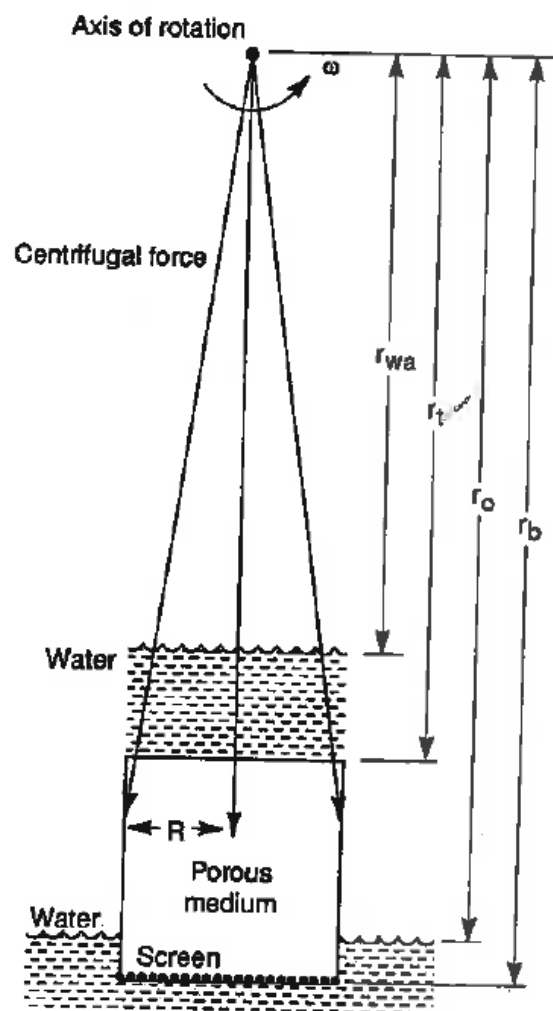


Figure 5: Simplified cross-sectional view of the test configuration used by Nimmo and Mello (1991) to measure the permeability in a centrifuge through falling and constant head tests. r_x denotes the radius from the axis of rotation to a specific point in the assembly (Nimmo and Mello, 1991).

2. Literature Review

For the falling head experiments the change in water level (r_{wa}) is monitored from a set datum (r_0) for successive centrifuge runs. By measuring the time of centrifugation for the total decrease in water level, the authors were able to calculate K_f as follows:

$$K = \frac{aL}{Ar_0\rho\omega^2(t-t_i)} \log \left[\frac{(r_0+r_{wa})(r_0-r_i)}{(r_0-r_{wa})(r_0+r_i)} \right] \quad (16)$$

where: A and a are the cross-sectional areas of the sample and falling head reservoir respectively, t and r_{wa} are the final times, t_i is the initial time measurement and r_i is the corresponding water level at t_i (Nimmo and Mello 1991).

By comparing the results of the centrifuge falling and constant head tests to conventional gravity driven falling head tests on the same material, Nimmo and Mello (1991) were able to determine the reliability of the centrifuge method. Upon comparison the authors found the measurements to agree within 20% for a given sample, with centrifuge methods measuring slightly higher than expected K values. The authors also state that due to better accuracy, reduced test time and uncomplicated experimental procedures, the falling head test was superior to the constant head test in the centrifuge. However, the authors caution that the resultant compaction due to the applied centrifugal force may alter the sample structure and influence K . For unconsolidated or highly structured material this becomes problematic and Nimmo and Mello (1991) suggest that the centrifuge methods are unsuitable for such materials. Nimmo and Mellow (1991) also suggest that this phenomenon could be used to reproduce overburden pressures (in-situ stresses) experienced at a specific sample location. This could possibly allow the estimation of K under simulated field conditions and provide insight to the effects of in-situ stresses on the K of a material.

A more recent attempt at measuring K in a centrifuge is presented by Singh and Gupta (2000). In their paper the authors present a falling head centrifuge model (Figure 6) and describe the test procedures used to measure the K of a silty sand at various void ratios in a small centrifuge (200 mm arm radius). Additionally, the results of the centrifuge tests have been compared to conventional 1g methods, allowing Singh and Gupta (2000) to define a centrifuge scaling law (Eq. 9) for K .

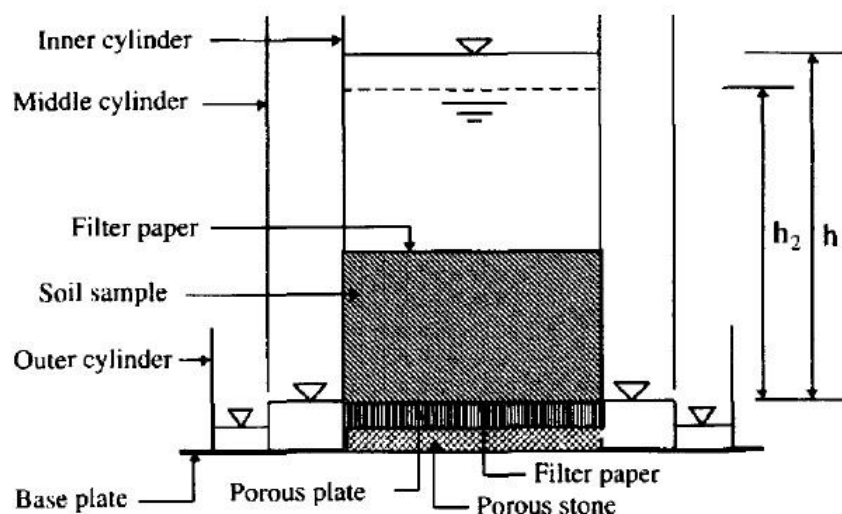


Figure 6: The centrifuge model assembly used by Singh and Gupta (2000).

2. Literature Review

As illustrated by Figure 6, the model consists of three concentric Perspex cylinders with the graduated inner cylinder containing a 30mm thick soil sample. The assembly was placed into the centrifuge and tests at accelerations of 50, 100, 150 and 200g were conducted on samples that were pre-compacted to different densities. Using this assembly Singh and Gupta (2000) were able to perform a falling head test during centrifugation. The fall in head ($h_1 - h_2$) is monitored on the graduated inner cylinder for the total time of centrifugation (t). These values are recorded and then substituted into Equation 17 to estimate K for the sample.

$$K_{cen} = \frac{L}{t} \ln \left(\frac{h_1}{h_2} \right) \quad (17)$$

Where L is the sample height and h_1 and h_2 are the initial and final heads respectively.

Singh and Gupta (2000) also conducted several 1g permeability tests on analogous samples with the same densities. The K values obtained from the centrifuge tests were compared to the values obtained from the conventional 1g tests to determine a scaling factor for K :

$$x = \frac{\ln \left(\frac{K_{cen}}{K_p} \right)}{\ln(N)} \quad (18)$$

where x is the scaling factor for K and K_{cen} and K_p are the permeabilities from the centrifuge and 1g test respectively (Singh and Gupta, 2000).

Applying Equation 18 to their experimental data, Singh and Gupta (2000) demonstrated that for all tests conducted, x tended towards unity. Hence, K has a scaling factor of 1: N (prototype to model) and the authors conclude that K is modelled N times in the centrifuge when compared to conventional 1g tests.



3. Study Area

To investigate the permeability of a heterogeneous coal mine backfill sequence, a small scale physical model of a backfill sequence was considered to be the best approach. By using the geotechnical centrifuge, the distribution of in-situ stresses present in a back fill sequence could be simulated. Provided the actual backfill material was used in the model, a large degree of similitude would be shared between the centrifuge model and backfill sequence being modelled. This would allow for the permeability of the model to be related to the actual backfill sequence, provided the associated scaling laws are well understood. To develop a geotechnical centrifuge model, a prototype is needed from which to develop the downscaled centrifuge model. For the purpose of this study the site needed to fulfil the following criteria in order to be suitable for the study:

- The study site needs to be a backfilled area located on an open cast coal mine owned by Exxaro Resources (Pty) Ltd.
- The backfilling sequence and procedures need to be clearly defined, in order to set the parameters for the model prototype.
- Backfilled areas need to be safe and easily accessible for field testing and sample collection.
- Sampling and field testing of the backfilled areas should be conducted without interfering with mining operations.
- Backfilling of the area where field testing is to be conducted should have been completed several years ago and should preferably be the oldest backfilled region on the mine to ensure the backfill is in an advanced state of settlement.

Using the above criteria, Leeuwpan Coal Mine (LCM) was selected as the site most suitable for the study. LCM is located roughly 8km to the East of the town Delmas in the Mpumalanga Province of South Africa (for locality plan refer to Figure 7). The mine is a conventional opencast coal mine employing modified terrace configurations and conventional truck and shovel operations. Annually LCM produces 3Mt of coal that is mostly consumed by the power generating and metal industries.

3.1. Climate and Surface Water Drainage

Based on the subdivision of South Africa into 24 climatic regions by Kruger (2004), Delmas is located within the Moist Highveld Grassland region. According to Kruger (2004) the climate of this region is typically temperate to moderate with a mean annual precipitation (MAP) of 600 - 800mm (1961-1990) and the maximum precipitation arriving in the summer (December and January). The winters are usually dry and harsh with approximately 30 frost days per annum (Kruger, 2004).

The study area is located within the B20A quaternary catchment of the Olifants Water Management Area (WMA). Locally, the major drainage feature is the Bronkhorstspruit River which is situated to the North-east of the study area (Figure 7). Drainage occurs towards this river in the region and both surface runoff and groundwater draining from the mine are likely to intersect the river. Two smaller, unnamed perennial streams intersect the study area in the

3. Study Area

far Western and central portions respectively. As such, the water quality and quantity of these streams is likely to be influenced by drainage and runoff from the mine. These perennial streams are possibly tributaries of the Bronkhorstspruit River and may contribute significantly to the water quality of the Bronkhorstspruit River.

Other notable surface water features include artificial irrigation dams, old open pit areas, pollution control dams and natural pans and wetlands.

3.2. Regional Geology

The regional geology, as illustrated by Figure 8, includes geological formations from the Witwatersrand, Transvaal and Karoo Supergroups respectively. Of these formations, the Vryheid Formation is the most notable with respect to the current investigation. The Vryheid Formation is currently being exploited by LCM for its abundant coal seams and will therefore constitute the bulk of the backfill material. As part of the Ecca Group within the Main Basin of the Karoo Supergroup, the Vryheid Formation typically consists of upward coarsening cycles of coal, shale/mudstone and sandstone (Johnson *et al.*, 2006). Thinning out towards the West of the basin, Johnson *et al.* (2006) state that the Vryheid Formation directly overlies pre-Karoo rocks or the Dwyka Group in this section of the Main Karoo Basin.

The Dwyka Group forms the lowest stratigraphic unit of the Karoo Supergroup and is characterised by glacial and marine basin deposits such as diamictite, conglomerate and mudrocks (Johnson, *et al.*, 2006). At LCM, the Diamictites of the Dwyka Group directly underlie the Vryheid Formation and forms the floor of the mining sequence.

Another notable formation in the vicinity of LCM is the Malmani Subgroup of the Chuniespoort Group (Transvaal Supergroup). As described by Eriksson *et al.* (2006), the Malmani Subgroup consist of up to 2000m of dolomitic and chert rich formations. At LCM the Malmani Subgroup typically underlies the Dwyka Group. The paleo-karst landscape created by the dolomite of the Malmani Subgroup, have according to van Rooyen (2014), resulted in an abnormal thickening of the coal seams in the area of Leeuwpan Mine.

As part of the Karoo Igneous Province, the Karoo Dolerite Suite is particularly well developed in the Main Karoo Basin (Duncan and Marsh, 2006). This intrusive igneous suite consists of an extensive network of dolerite dykes and sills and is thought to be part of the Karoo flood basalt feeder system (Duncan and Marsh, 2006). A large dolerite sill is present in the Western portion of the study area (Figure 8). According to van Rooyen (2014) this dolerite sill is approximately 15 m thick and has resulted in devolatilisation of the coal seams in close proximity to the sill.

Along the South-western boundary of the study area, an isolated outcrop of the Hospital Hill Subgroup is intersected. As part of the West Rand Group within the Witwatersrand Supergroup, the Hospital Hill Subgroup is typically composed of orthoquartzites interbedded with shale and ferruginous shale units (McCarthy, 2006). As Illustrated by Figure 8, the Hospital Hill Subgroup is not abundant in the region and only occurs as isolated outcrops.

In terms of geological structures, no major faults or lineations have been identified in close proximity to the study area. The dolerite dykes and sills as well as paleo karst



3. Study Area

environment of the dolomite formations are thought to have the most significant influence on the structural geology of the area. The intrusion of the dolerite dykes and sills has resulted in significant fracturing and thermal metamorphism of nearby rock formations (Grobbelaar *et al.*, 2004). The paleo-karst environment and dissolution of the underlying dolomite formations may result in the development of sinkholes and/or dolines, which could potentially increase the vulnerability of groundwater resources to surface contaminants.

3. Study Area

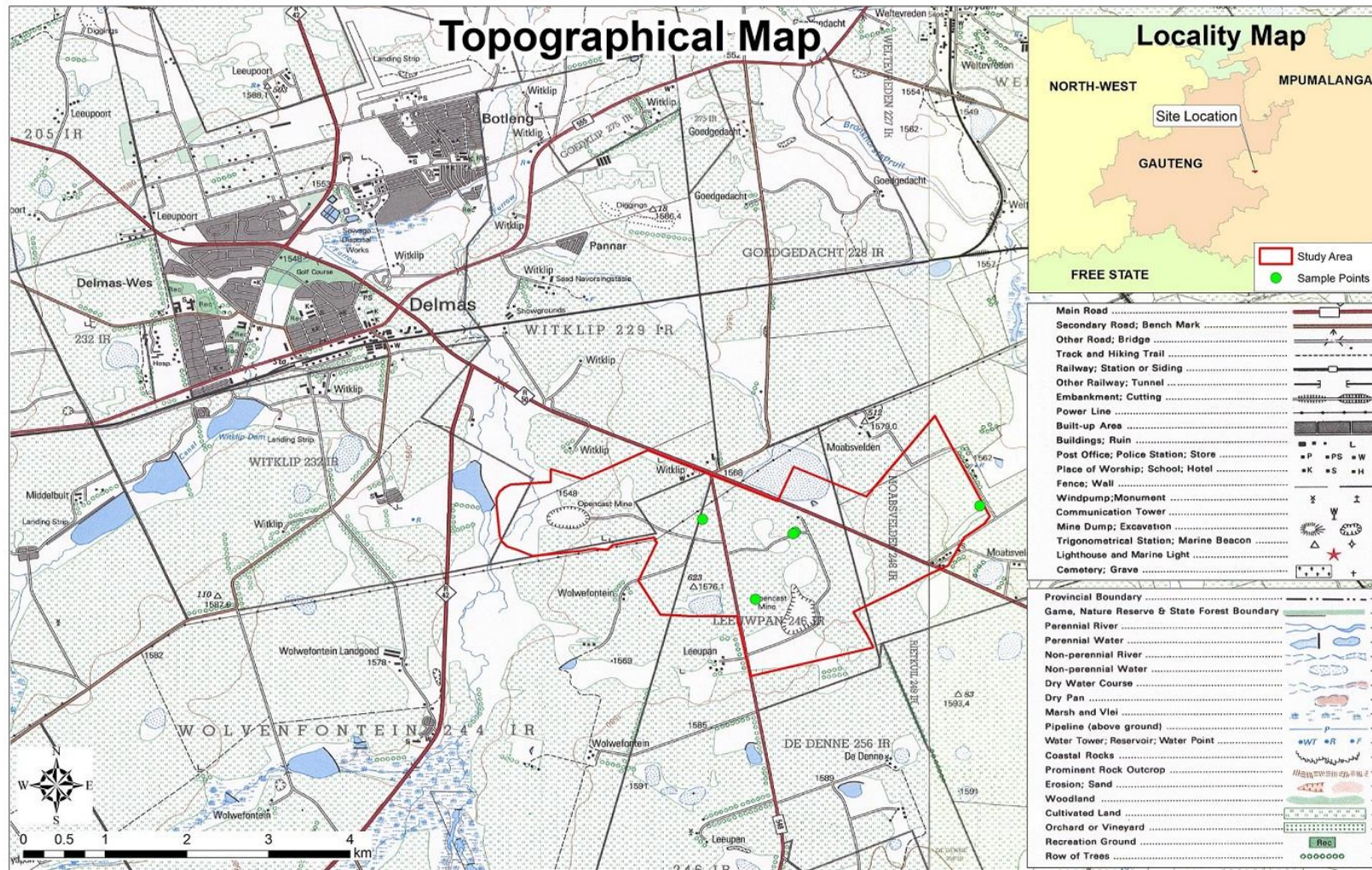


Figure 7: Site locality and topographical map outlining the study area and illustrating local surface water features.

3. Study Area

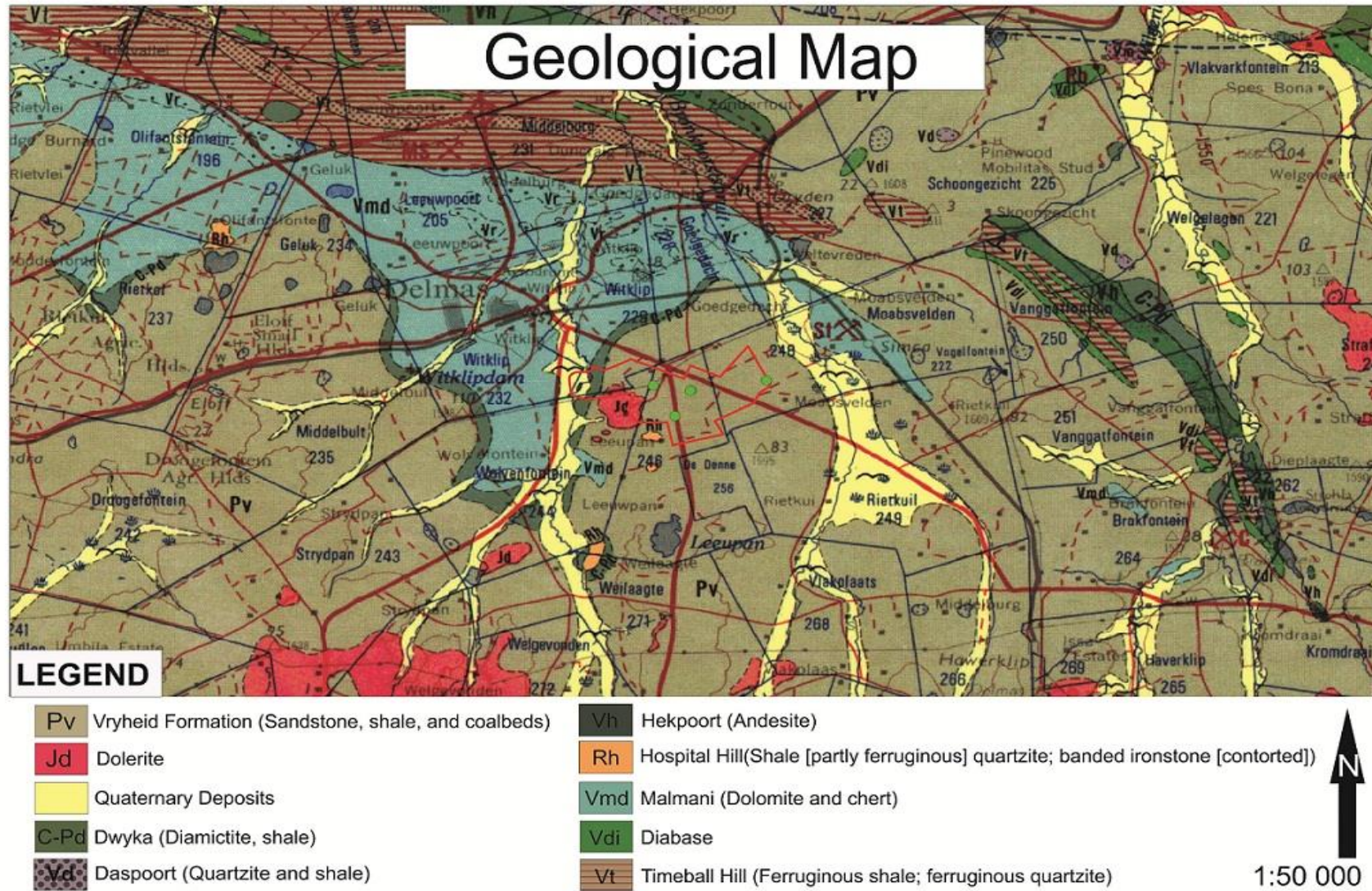


Figure 8: Regional geology map indicating the outline of the study area in red and the sample locations as green dots within the study area.

3.3. Hydrogeology

Based on the geological formations present in the region (Figure 8), there are likely to be three distinctive aquifer systems superimposed over each other (Grobbelaar *et al.*, 2004). These aquifer systems, as outlined by Grobbelaar *et al.* (2004) and van Rooyen (2014), can be classified as follows:

- Shallow, primary porosity aquifer composed of unconsolidated alluvial or colluvial deposits and weathered Eccca Group sediments;
- Intermediate, secondary porosity aquifer formed by the fracturing of the Eccca sediments by dolerite intrusions; and
- Deep, tertiary porosity (karst) aquifer formed by the dissolution of the Malmani Subgroup dolomites.

The upper weathered aquifer typically extends to weathering depths of between 5 – 12m and water is usually encountered close to the surface (Grobbelaar *et al.*, 2004). The water table in this aquifer may become perched due to underlying shale and mudstone aquicludes. As noted by Grobbelaar *et al.* (2004) and van Rooyen (2014), the perched water table is likely to intersect the surface at topographic lows and flow barriers such as dolerite dykes. As a result the groundwater may reappear on surface and is manifested as springs, seeps and temporary or permanent wetlands. According to Grobbelaar *et al.* (2004) the recharge value of this aquifer is in the order of 3% of the MAP and is considered to be a low yielding aquifer with typical yields of 100 - 200 L/h. Although this aquifer is rarely used for water supply purposes, its importance in the attenuation and transport of surface contaminants, especially in close proximity to the mine, should not be underestimated (van Rooyen, 2014).

The intermediate, fractured hard rock aquifer underlies the shallow weathered aquifer and is typically 40m thick in the region of LCM (van Rooyen, 2014). Due to the well cemented nature of the unweathered Eccca rocks, Grobbelaar *et al.* (2004) notes that secondary structures will control the movement of groundwater through this aquifer. Fracture networks, formed due to the intrusion of dolerite dykes and sills and the bedded nature of the more competent Eccca rocks have resulted in vertical and horizontal interconnectivity of the unweathered Eccca rocks. Flow paths may be both laterally and/or vertically constrained by dolerite dykes and sills (aquitards), which results in groundwater compartmentalization (van Rooyen, 2014). Yields of this aquifer are highly variable and are typically between 360 - 18000L/h according to van Rooyen (2014). Although high yielding boreholes may be encountered in highly fractured zones surrounding dolerite intrusions, the unweathered rocks of the Eccca are not considered to be a major aquifer.

The Malmani Subgroup is a well distinguished aquifer in the Delmas region and is locally used to supply potable water to the community of Delmas and water for large scale irrigation (Pietersen *et al.* 2011). Regionally known as the Botleng Aquifer, Pietersen *et al.* (2011) have described it as high yielding “with more than half of boreholes exceeding 5L/s” and transmissivities of several hundred m²/day. These properties are a result of dolomite dissolution along structural and lithological discontinuities such as grikes, fractures and joints (Pietersen *et al.*, 2011). These dissolution features result in underground cavities with a large storage potential. It is not uncommon for the aquifer to be directly connected to the surface

3. Study Area

through depressions, sinkholes and river beds. As such, water levels respond immediately to rainfall events and Pietersen *et al.* (2011) have described the aquifer as highly vulnerable to contamination.

In the study area, the Botleng Aquifer is overlain by the Dwyka Group tillites. These tillites are relatively impermeable and are regarded as an aquiclude by van Rooyen (2014). This aquiclude should provide some degree of protection to the underlying Botleng aquifer in the mining area and surrounds. However, fracturing of the Dwyka due to dolerite intrusions and blasting activities may result in mine effluents discharging into the Botleng aquifer over time. Also, a thin covering of the Dwyka aquiclude in the vicinity of paleo-karst topographical highs (dolomite pinnacles), may result in some interconnectivity between the Botleng aquifer and surface contaminants.

3.4. Backfilling Material and Typical Backfill Sequence

The Standard Practice Instruction (SPI) for procedures to maintain slope stability at LCM provides an outline of the backfilling procedures and sequence of backfilling. Figure 9 below illustrates the typical lithology's and bench configurations (dimensions) of the open pits as well as the typical backfill sequence to be expected at LCM. The lithologies are typically sub-divided into four distinct classes based on the ease of extraction (mining), stratigraphic position and the rock composition. The four classes and their typical properties are discussed below.

The upper-most portion of the mining profile is known as the soil horizon. The soil horizon, according to SPI (2014), consists of a selection of transported soils (colluvium and alluvium), residual soils weathered from sedimentary rocks and pedogenic ferricrete in some places. These soil horizons are generally between 3 m to 5 m thick and an average thickness of 4 m is illustrated in Figure 9. As stated in SPI (2014), the soil is generally classified as sandy clays to clayey sands with the expansiveness of the clays varying from medium to highly expansive.

The weathered overburden material found directly below the upper soil horizon is known as the "softs" horizon and consists of highly weathered, weak sandstone. This soft rock material is usually between 10 m and 20 m thick with an average thickness of 14 m being illustrated in Figure 9. At LCM the term overburden is used to collectively describe material overlying the coal seams that does not require blasting and can be removed with an excavator (SPI, 2014). Based on this classification, both the upper soil and "softs" horizons are classified as overburden material.

Directly underlying the weathered overburden materials is the less weathered interburden material referred to as the "hards" horizon in SPI (2014). The interburden consists of hard, fair quality sandstone, siltstone and shale which required blasting in order to be excavated. The average thickness of the interburden, as illustrated by Figure 9, is 12 m but this thickness may vary between 0 m and 15 m at LCM.

3. Study Area

The coal horizon, also known as the mining horizon, consists of interbedded coal seams and carbonaceous shale beds with an average thickness of 16 m, as illustrated by Figure 9. The mining horizon is blasted and then hauled to the plant for beneficiation, after which the discarded carbonaceous material is used in the backfilling process.

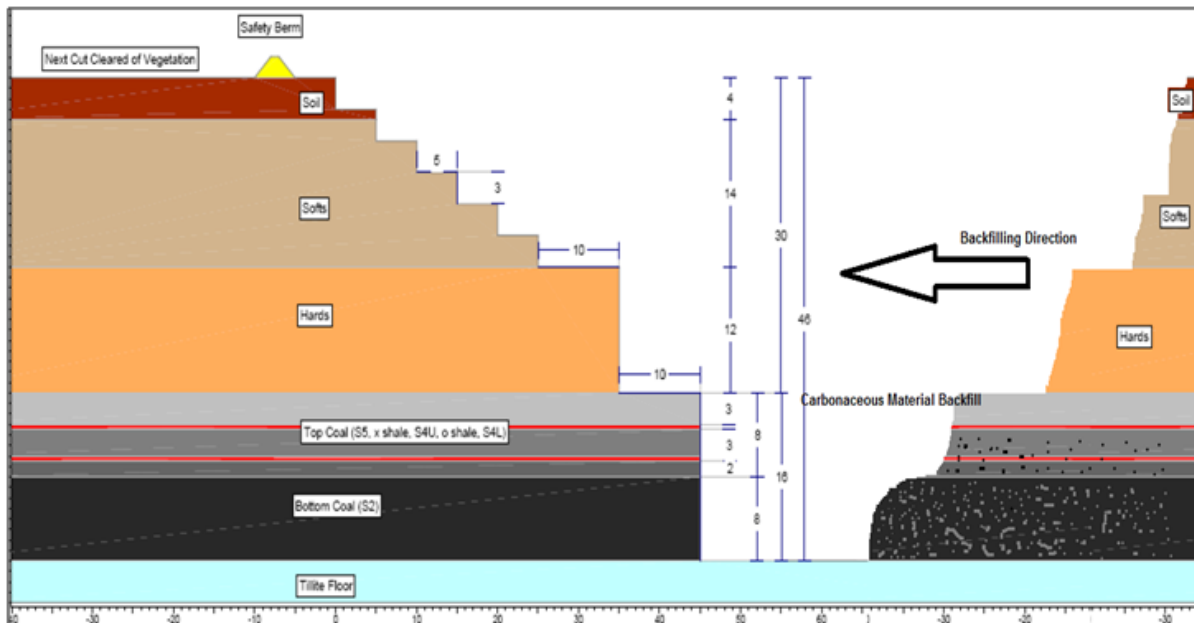


Figure 9: Open pit bench configurations and typical backfill sequence at LCM (SPI, 2014).

As illustrated by Figure 9 the typical mining sequence at LCM (from surface to tillite floor) is on average a total of 46 m thick with an average of 18 m of overburden, 12 m of interburden (labelled as “hards” in Figure 9) and a 16m thick mining horizon. When backfilling the mined-out areas, the objective is to fill the pit up to the original ground surface level. At LCM the backfilling process follows the guidelines outline in SPI (2014), so that the mined-out land is restored (as close as possible) to its pre-mining state/condition. This involves replacing the removed material back into the pit in the same sequence as it was found before being mined out (Figure 9).

The backfilling process is carried out by constructing benches from the mined out material. This is achieved through the process of end tipping and dozing where successive ramps are created at different elevations as the open pit is filled up. Each backfill horizon is hauled to a backfilling area and successively dumped into the mined out pit. When a backfill horizon reaches its designated elevation, the surface is levelled off with a bulldozer before the dumping of the next horizon in the backfill sequence can commence. No material, other than the fertile topsoil is stockpiled and the overburden and interburden are removed, hauled and then dumped into a backfilling sequence. To minimize contamination, dumping and bulldozing of the backfill takes place at least 45 m from the mining face and a fixed backfilling sequence is followed from the tillite floor to the top soil at the surface.

The first backfill horizon is placed directly onto the tillite floor and is known as the carbonaceous backfill material. This horizon consists of carbonaceous material and includes plant discard, filter cake, slurry and any other carbonaceous material that was mined out.



3. Study Area

From the tillite floor, this horizon is typically only built up to the top of the mining horizon (± 16 m) before being levelled off with a bulldozer.

After the carbonaceous material horizon has been levelled off, successive ramps are constructed and the hard rock sandstone, siltstone and shale interburden material is dumped onto the underlying carbonaceous bench. Ideally, the interburden should be backfilled up to the top of the interburden level in the mining sequence (± 12 m above the carbonaceous horizon) before it is bulldozed flat. The same procedure is followed for the weathered material of the "softs" horizon, which is backfilled up to the original ground level.

After the "softs" backfill horizon has been bulldozed, approximately 2 m of sub-soil is placed on top of the "softs" and compacted to minimize infiltration of surface runoff into the backfilled regions. Finally, the stockpiled topsoil is placed at the top of the backfill sequence, thus completing the backfilling process. After completion of the backfilling process the surface should be somewhat above the original ground surface level. This is done to account for the consolidation/settlement of the loose backfill material. Ideally, the backfill should return to the original ground surface level as it consolidates/settles over time.

4. Materials and Methods

Due to the nature of the research, the methodology has been sub-divided into the following categories: Field methodology, laboratory methodology, the centrifuge model and data analysis and processing methods. For each category the relevant methodologies and approaches to problem solving have been discussed in detail.

4.1. Field Methodology

4.1.1. Field permeability testing

In order to determine the reliability of the values obtained from the centrifuge permeability tests, in-situ permeability values are needed for comparison. This required the selection of an appropriate field site that could be adequately simulated with the centrifuge model. Thus, by simulating the in-situ conditions in the centrifuge model one could better understand the reliability and limitations of the centrifuge model.

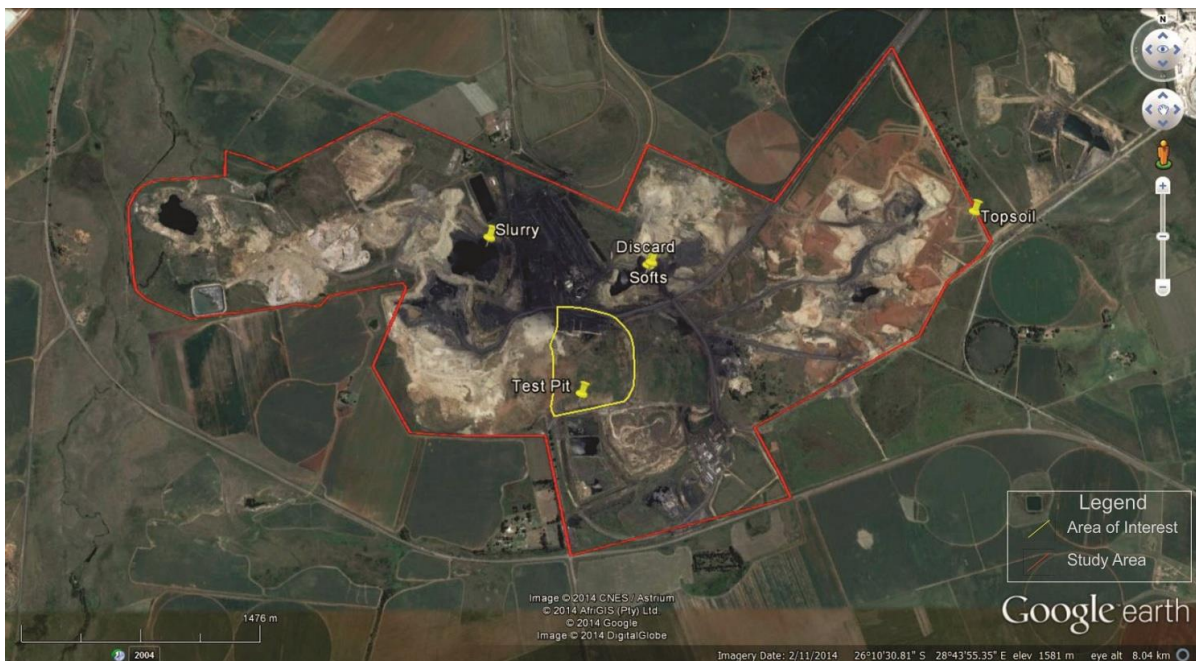


Figure 10: Map indicating the sample locations and position of the test-pit on a historically backfilled area (outlined in yellow). Image courtesy of Google Earth.

The area selected for the field permeability tests was a historically backfilled and rehabilitated area, as highlighted in yellow on Figure 10. This is the oldest rehabilitated area at LCM where the backfilling was completed in the year 2000. To determine the in-situ permeability of the backfill, four percolation tests were conducted at the bottom of a single test-pit/trench that was dug into the backfill material. The standard methodology for percolation tests, as outlined in SANS 10252-2:1993 and Dippenaar *et al.* (2014), was adapted for the purpose of this investigation.

A test-pit was excavated to a depth of 1.5 m and the soil profile was logged accordingly. The soil profile description and accompanying image can be found in the Appendix. To prepare the holes for the percolation tests, a 150 mm wide by 300 mm long soil auger was used to drill

4. Materials and Methods

a hole to a depth of 400 mm. The dimensions of the holes were in line with the dimensions suggested by SANS 10252-2:1993 (150 mm diameter by 400 mm deep) and were spaced approximately 1m apart on the floor of the test-pit. Once a hole was prepared, a 150 mm by 500 mm Perspex tube was inserted into the hole and seated tightly against the bottom of the hole. At the top of the Perspex tube a 50 mm section was marked with 10 mm intervals as illustrated by Figure 11. Before starting the percolation tests, the tube was filled with water up to the top marker (t_0) and allowed to drain to the bottom marker (t_5) twice. This would pre-soak the soil directly below the bottom of the hole and ensure adequate saturation for the test.

After pre-soaking, the tube was again filled to the top marker and a stopwatch was started. The time taken for the water level to drop between two markers (10 mm) was recorded until the water level reached the bottom marker. At this point, the stopwatch was stopped and the time for the final 10 mm drop was recorded. The stopwatch was then reset and the tube again filled to t_0 for the start of the second run. This process was successively repeated for at least 3 runs or until the difference in time taken for the full 50 mm drop ($t_0 - t_5$) between successive runs was less than 10%. After the completion of a test, the next auger hole was prepared and tested as outlined above.

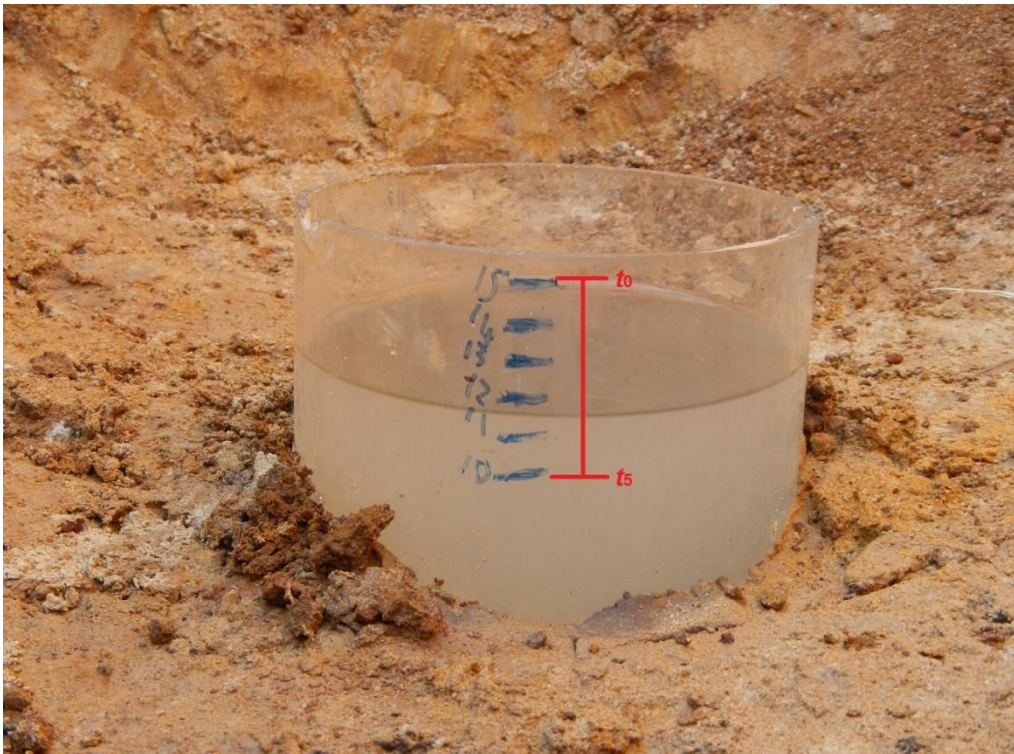


Figure 11: The Perspex tube seated in the auger hole as it was used for the percolation tests.

The use of the Perspex tube was found to have the following advantages over the standard method outlined in SANS 10252-2:1993:

- The tube prevented water from seeping through the side walls of the hole and ensured that only the vertical permeability is measured.
- As the Perspex tube is 500 mm long, it protrudes 100 mm beyond the top of the hole. This significantly increased the accuracy of water level measurements, as one could view the change in head directly from the side with minimal parallax inaccuracies.



4. Materials and Methods

- Additionally, the extension of the tube also increases in head above the bottom of the auger hole. Thus, greater water pressures are induced on the base of the hole which promoted quicker saturation of the underlying soil and steady state being reached in less time.

Due to mine health and safety regulations, the test-pit could only be excavated to a maximum depth of 1.5m below surface. This was deemed adequate as it would allow the percolation testing to be conducted below the traffic compacted zone (approximately upper 500 mm). At this depth the test-pit intersected the top of the "softs" horizon and all percolation tests were conducted in this material. After completion of the percolation tests, the test-pit was extended by 0.5 m to confirm continuity of the "softs" material below the test positions.

4.1.2. Backfill material sampling

In order to construct the centrifuge models, samples of each backfill horizon were needed. These samples were collected using two different methods. Firstly, to correlate the centrifuge model results to the field permeability values, the "softs" material extracted with the soil auger (when drilling holes for the percolation tests) was placed into a single sample bag for each auger hole. This material was used to construct the centrifuge model for the correlation test that would test the reliability of the centrifuge model. This was done by simulating the in-situ conditions of the percolation test site.

The second method of sampling involved collecting bulk (30 kg bags) samples of each backfill horizon. As it was not possible to dig open or drill through the backfill (due to risk of spontaneous combustion of carbonaceous material), samples were taken from areas that were in the process of being backfilled or other storage locations. This allowed access to each horizon of the backfill sequence and samples were taken using a shovel and large heavy duty plastic bags. The sample positions for each of the respective backfill horizons can be seen on Figure 10. The slurry was sampled separately from a slimes dam, as it is only added to the backfill if additional bulk is needed to reach the required carbonaceous elevation in the backfill sequence (Figure 9) or if the slurry dam is full. The top soil was sampled from a stockpile area where the top soil had been placed after removal.

Due to the competent rock formations of the interburden horizon, the blasting results in fragmentation of the rock into large (up to room size) boulders. These boulders were too large to be used in the centrifuge model and were consequently not sampled. This resulted in the exclusion of the interburden horizon from the centrifuge model which is explained in Section 4.3.1.

4.2. Laboratory Methodology

4.2.1. Grain size analysis

All samples collected from the field as well as the prepared material used for the centrifuge models were sent to Soil Lab (Pty) Ltd in Pretoria for grain size analysis. To obtain the particle size distributions (PSD) of the samples the material was first sieved through a standard series of mesh sieves with diameters ranging from 63.00 mm to 0.075 mm. The distribution of any material passing the 0.075 sieve is then further classified through a

4. Materials and Methods

hydrometer analysis. The hydrometer analysis then reports the relative proportions of material between 0.04 mm and 0.002 mm. Using these measured values the PSD for each sample was plotted and the relative proportions of clay, silt, sand and gravel were determined. Soil Lab (Pty) Ltd is a SANAS accredited laboratory and all analysis were conducted according to the standard operating procedures prescribed by SANAS.

4.3. Centrifuge Model

4.3.1. *Developing the centrifuge model*

Based on the reviewed literature, most centrifuge models used for measuring permeability are complex in their design with many specialised components and generally only used to test small samples. Also, considering that these studies are not aimed at replicating dimensions and properties of a specific prototype, these types of models are not very adaptable and are aimed at investigating specific processes rather than modelling a prototype scenario. As outlined in Section 2.2, when modelling a specific event or prototype the centrifuge model should replicate both the geometry and physical properties of the prototype as accurately as possible. Hence, most of the available permeability centrifuge models were inadequate for the objectives of the research. However, Singh and Gupta (2000) provide a model that may be more adaptable to a specific prototype scenario and give valuable insight into model design, test methods and scaling laws for permeability tests in the centrifuge. As illustrated by Figure 6, their model consisted of three concentric Perspex cylinders with the graduated inner cylinder containing a 30mm thick soil sample. Using this set-up Singh and Gupta (2000) were able to perform a falling head test during centrifugation by monitoring the fall in head on the graduated inner cylinder. They were then able to calculate the permeability of the soil sample and define scaling laws for modelling permeability in the centrifuge (as discussed in Section 2.3.5). Although the model presented by Singh and Gupta (2000) was designed for small samples at high accelerations in small centrifuges, the use of Perspex cylinders makes the model adaptable to a wide range of modelling scenarios. When using a large geotechnical centrifuge, the dimensions of the Perspex cylinders can be increased to accommodate much larger samples. Thus, the model setup could be suitably adapted to model the prototype backfill sequence at LCM.

Based on the backfill sequence for LCM (Figure 9) a prototype can be visualised using the average thickness of each horizon and their positions in the backfill sequence. As such, the prototype can be perceived as a 46m thick sequence consisting of four successive layers, each with unique physical properties and different thicknesses. As mentioned in Section 4.1.2 the large boulders of the interburden horizon were not sampled. These boulders are not crushed (unless they are too large to be loaded onto a haul truck) and are dumped as is into the backfill sequence. To model these boulders would require a significant effort in acquiring average dimensions for the boulders as well as a substitute material with similar physical properties to use in the model. The inclusion of the interburden horizon would also create complex scale effects due to the need to downscale the boulders in the model, while using a different scale factor for the other three horizons. However, it was believed that due to the large size of the boulders, this horizon would not control the overall permeability of the backfill. As demonstrated by Kenny *et al.* (1984), the size of the fine fraction was found to control the overall permeability of granular materials. It was therefore reasoned that the fine material

4. Materials and Methods

originating from the underlying carbonaceous or overlying overburden layers may fill the spaces between the larger boulders and would regulate the permeability in the interburden horizon. Based on the above reasoning, it was considered reasonable to omit the interburden horizon from the prototype. This resulted in a three layer prototype with an overall thickness of 34 m composed of 16 m of carbonaceous material at the base, 14 m of overburden material in the middle and 4 m of top soil at the top of the sequence.

With the dimensions of the prototype well defined, the scaling of the prototype becomes a function of the modelling height and the centrifugal acceleration, as demonstrated by Equation 9. Based on the Perspex model of Singh and Gupta (2000) and the available space on the centrifuge platform, it was determined that a Perspex cylinder of 1000 mm in height would fit into the available space. A Perspex cylinder of this size also accommodated a sample large enough to simulate the prototype thickness at manageable acceleration levels. Using a total sample height (h_m) of 600 mm, an acceleration (N) of 56.67G would be needed to simulate a prototype height (h_{pr}) of 34 m (Equation 9). Applying this level of acceleration, the thickness of each layer in the model was calculated using Equation 9 and is presented in Table 2 below.

Table 2: Prototype horizon thicknesses and their scaled model thickness based on a centrifugal acceleration of 56.67G and a modelling height of 600mm

Horizon	Thickness in prototype (m)	Thickness in model (m)
Top soil	4	0.07
Soft overburden	14	0.25
Carbonaceous material	16	0.28
Total thickness	34	0.6

This allowed for 400 mm space to accommodate a filter below the sample as well as a water head and overflow space above the sample. The model set-up, as illustrated by Figure 12, included a 50 mm filter at the base, the 600 mm sample on top of the filter and a 300 mm water head above the sample. A space of 50 mm was left above the water head to prevent the water from spilling when transferring the model onto the centrifuge platform. To allow flow out of the cylinder, two holes were drilled in the bottom of the cylinder to accommodate the outlet valves. Finally, an 8 mm thick Perspex sheet was fixed to the bottom of the cylinder to provide a watertight seal and foundation for the bottom of the cylinder.

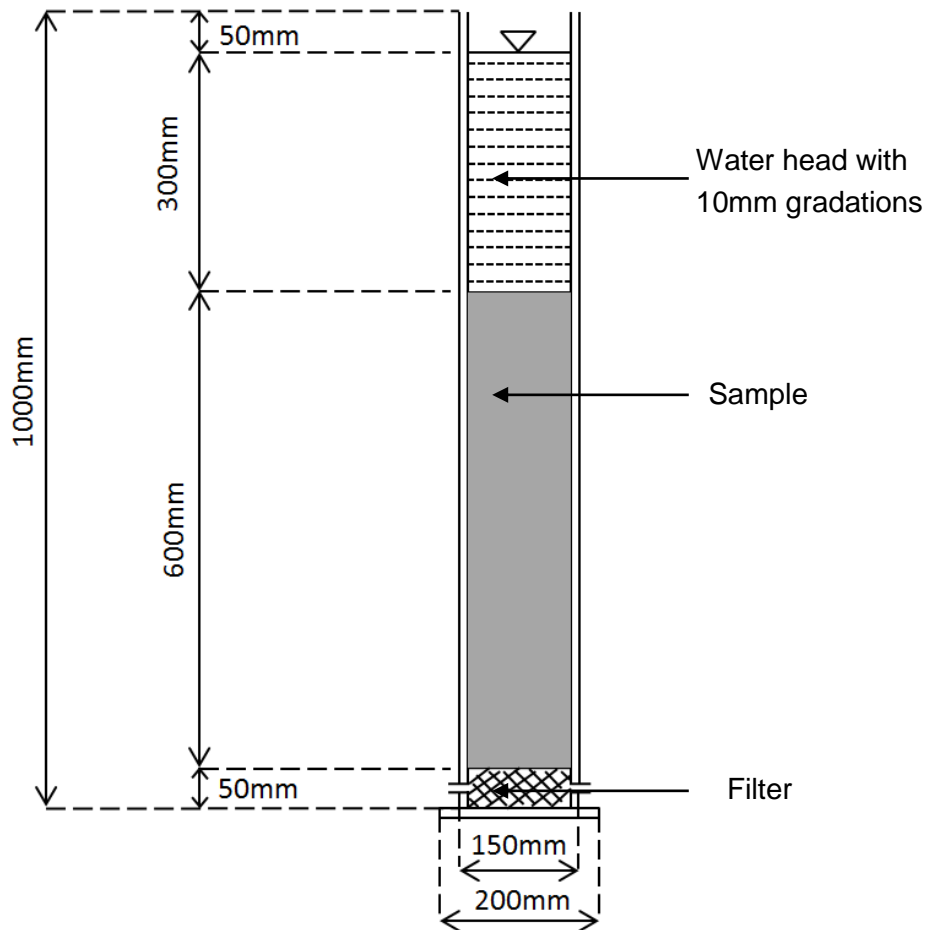


Figure 12: The Perspex cylinder model set-up.

To determine the permeability of the sample, the fall in head can be measured from a defined datum by using the gradations on the cylinder during centrifugation. Then, using the falling head formula of Singh and Gupta (2000) (Equation 17) the permeability of the sample can be calculated. Although useful, this falling head formula only provides a single K value for the entire sample thickness and it is not possible to determine the K values of each individual layer in the sample. To achieve this, small pore pressure transducers (PPTs) were placed at predetermined distances from each other in the backfill sample (see Figure 25 below). The methods used to estimate the permeability using the PPTs is presented in Section 4.4.2 below.

4. Materials and Methods

4.3.2. Model setup and construction

Based on the Perspex cylinder model discussed in Section 4.3.1 above, an assembly was designed using a strong box to support the model and all its components in the centrifuge. The model assembly as used for the centrifuge tests is illustrated by Figure 13 and the specifications of the components are discussed below.

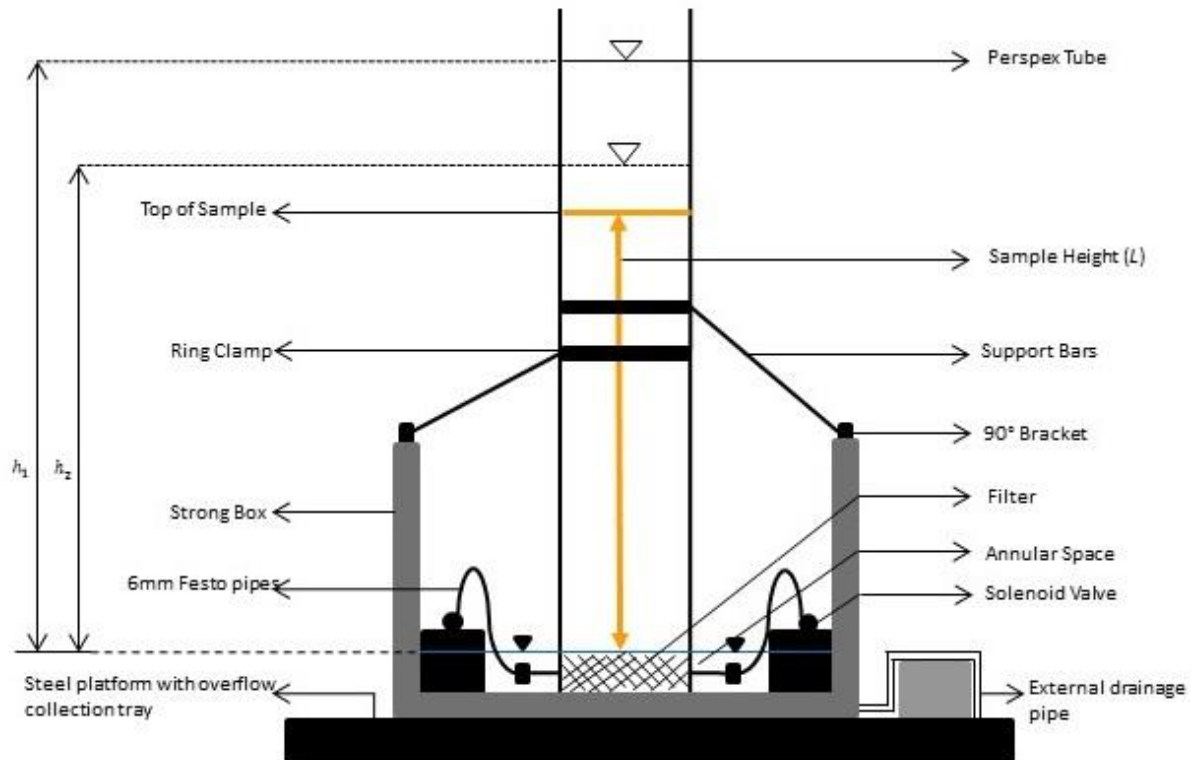


Figure 13: Cross-sectional view of the centrifuge model assembly.

4.3.2.1 Perspex cylinder

To monitor the fall in head during centrifugation and control the thickness of each layer when packing the model, a clear cylinder was needed. Due to the fact that the Perspex is clear, lightweight and strong enough to withstand the elevated accelerations in the centrifuge, a Perspex cylinder was used in the construction of the model. The two 1000 mm long cylinders used each had an outside diameter of 150 mm and wall thicknesses of 3 mm and 5 mm respectively (resulting in inside diameters of 144 mm and 140 mm respectively). These inside diameters would contain a sample large enough to minimise the skin effect caused by water moving down between the sample and the inside of the cylinder.

To seal off the bottom and provide a base to support the cylinder, a 200 mm x 200 mm piece of 8 mm thick Perspex sheeting was fixed to the bottom of the cylinder. To ensure that the base was firmly fixed to the cylinder, a 4mm deep circular groove was routed into the Perspex sheeting. The groove was then lined with Perspex adhesive before the cylinder was slotted into the groove and fixed to the base. The outside contact between the tube and the base was then sealed off with Soudal Fix All® Crystal adhesive and sealant to provide a sturdy and water tight connection between the base and the cylinder.

4. Materials and Methods

To provide free drainage from the cylinder into the annular space, two holes were drilled at opposite ends of the cylinder. The centre of each hole was 20 mm from the base of the cylinder and threaded to fit a 13mm Festo outlet valve. After the valves were screwed into position, the joint was waterproofed and reinforced with Soudal Fix All® Crystal adhesive/sealant. To complete the construction of the cylinder, the positions of the filter, sample height, supports and overflow were marked off on the cylinder. A transparency graduated in 10 mm increments, was fixed into position to monitor the fall in water head above the sample. Figure 14 illustrates the Perspex cylinder as it was used in the model assembly.

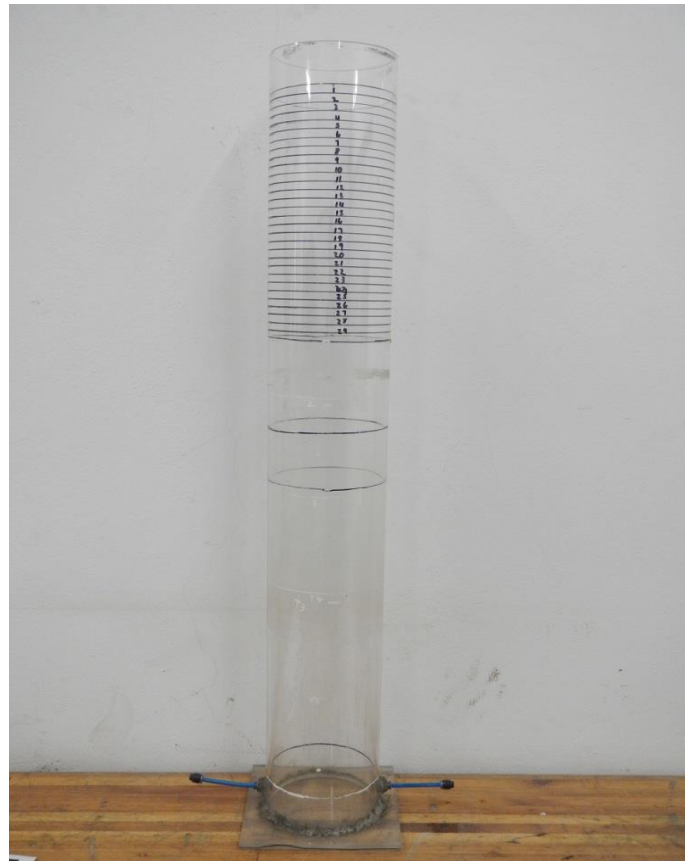


Figure 14: The Perspex cylinder that was used in the centrifuge model assembly with the Festo valves fitted and the positions of the filter, supports, sample top and gradations marked off.

4.3.2.2 Strong box and support system

The strong box provided by the Department of Civil Engineering provided a suitable platform to support the cylinder and supplied an ideal drainage mechanism to accommodate the overflow system of the model. The strong box is constructed of 50 mm thick solid aluminium walls with the front panel containing an 80 mm thick glass observation window. The inside of the box is 400 mm wide, 600 mm long and 400 mm high and provided ample space to accommodate the cylinder and overflow system. To aid in drainage or saturation of the strongbox, the base contains six drainage ports (three on each side). These ports are connected to an outflow pipe that formed part of the overflow system and ensured that the model could drain freely. The strong box was placed on 1000 mm long by 800 mm wide steel platform that contained the overflow collection tray and could be used to move the box with a fork lift.

4. Materials and Methods

A 25 mm thick by 50 mm wide attachment collar was added to the top of the strong box for the attachment of the support system. To stabilise the cylinder, 20 mm wide ring clamps were constructed from 490 mm lengths of galvanised steel sheeting. To ensure a tight fit and prevent the rings from slipping, the inside of the rings were covered with 3 mm thick foam strips (Figure 15a). These clamps were fitted around the cylinder and then connected to the support bars with an 8 mm bolt and nut. The support bars consisted of 3 mm thick by 25 mm wide sections of steel flat bar. Holes were drilled at the ends of the flat bar which connected the one end to the ring clamp and the other end to a 90° bracket that was bolted to the attachment collar (Figure 15b). To provide maximum stability, the brackets were bolted onto the attachment collar so that the support bars were 90° from each other (Figure 15c).



Figure 15: (a) The foam lined ring clamp that was used to fix the support bars to the cylinder. (b) The support bar connected to the ring clamp and the 90° bracket. (c) The support system fixed to the strong box collar and attached to the cylinder, with the support bars at 90° from each other.

4.3.2.3 Filter

To facilitate an even distribution of drainage through the base of the model a unique filter was designed. The filter needed to be incompressible (to support the weight of the overlying sample at elevated accelerations) and have a greater permeability than the sample to allow free drainage through the bottom of the model. After experimenting with numerous ideas, it was found that solid plastic bullets used in soft air guns had the properties that were needed for the filter. The plastic bullets are all perfectly spherical, the same size (6 mm diameter) and incompressible. The size and packing of the bullets ensured that the filter maintained a greater permeability than the overlying sample. To prevent the bullets from blocking the outlet valves and restricting the flow, they were encased with a single layer of A4

4. Materials and Methods

Bidim (a needle punched geotextile) (Figure 16). The geotextile held the filter together and also prevented the bullets from mixing with the sample. The geotextile is highly permeable and was not thought to influence the permeability of the sample at all.



Figure 16: The 6 mm BB bullets enclosed in the A4 Bidim to form the filter.

4.3.2.3 Flow system

To allow flow from the model, 6 mm ten bar pneumatic Festo tubes were connected to the valves at the bottom of the model. These pipes were connected to solenoid valves placed on concrete blocks inside the strong box (Figure 17a and b). The solenoid valves were remotely controlled from the centrifuge control room and could be opened or closed at any stage during the test. To initiate flow, both solenoid valves are opened and water is allowed to flow through the model and filter. The water then passes through the outlet pipes and solenoid valves and drains into the annular space. As with the falling head test of Singh and Gupta (2000) the water level in the annular space was maintained at the height of the filter (Figure 13). To maintain the water in the annular space at 50 mm above the base of the cylinder, the external drainage pipe connected to the drainage holes of strongbox was elevated to 100 mm above the steel platform with a concrete block (Figure 17c). This ensured that any excess water in the annular space (water flowing out of the model) drained away immediately. The external drainage pipe then drained the water into the overflow collection tray in the steel platform below the strong box (Figure 17d).

4. Materials and Methods

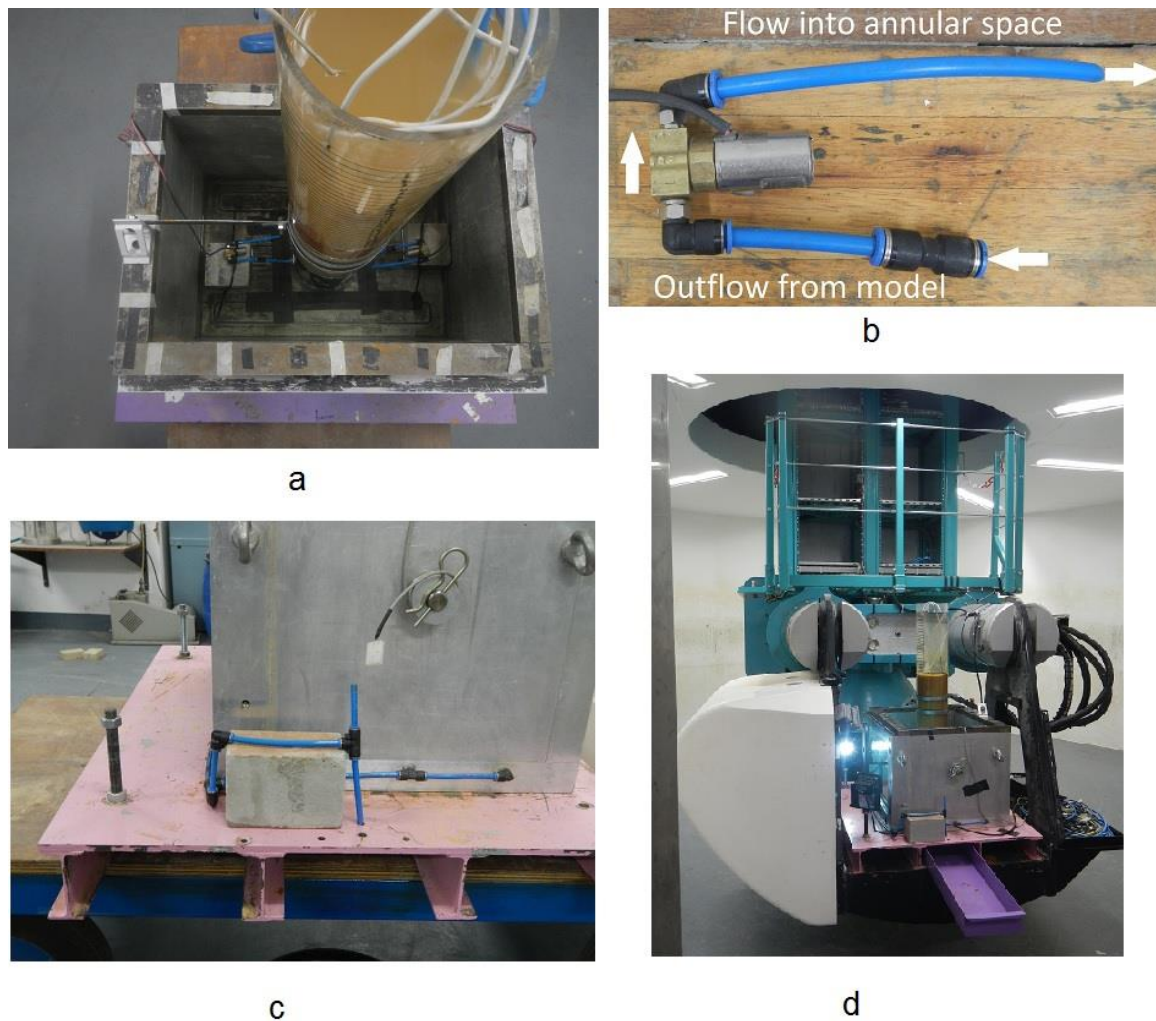


Figure 17: The overflow system and its components. (a) Solenoid valves connected to the outlet valves and placed on concrete blocks in the annular space. (b) The flow configuration of the solenoid valves. (c) Elevation of external drainage pipe to 100 mm above the steel platform to maintain the water level in the annular space at the filter height. (d) The overflow collection tray being slotted into place underneath the model assembly on the centrifuge platform.

4.3.3. Instrumentation

4.3.3.1 The University of Pretoria's geotechnical centrifuge:

The laboratories of the Department of Civil Engineering is equipped with a 150 g-ton Actidyn C67-4 beam centrifuge (Figure 18). The centrifuge has a 0.8 m x 1.0 m swinging platform attached to a 3 m long beam (measured from axis of rotation to platform). During testing, the platform is rotated so that it is always normal to the resultant acceleration (Jones, 2014). Capable of accelerating a payload of 1500kg to 100g or a smaller payload of 950kg to 130g, the centrifuge was more than capable of reaching the accelerations required for the study.



Figure 18: The University of Pretoria's geotechnical centrifuge in the enclosure at the Department of Civil Engineering (Jones, 2014).

The centrifuge is equipped with two cameras which monitor both the cross sectional profile and plan view of a model during testing (Jacobsz *et al.*, 2014). Additionally, a high definition (HD) web camera can be mounted anywhere on the platform or model to provide the required surveillance angle of the model. The cameras provide live feedback to the monitors in the centrifuge control room and the in-flight model behaviour can be directly observed. Water supply to the centrifuge platform is made possible with a fluid rotary joint. The flow rate is monitored and controlled by pressure regulators and flow meters from the hydraulic control panel in the control room (Jacobsz *et al.*, 2014). This allows water supply to models to be initiated and regulated at any stage of the test. Equipped with the Digidaq data acquisition system (developed at the University of Western Australia, see Gaudin *et al.*, 2010), a wide of range instrumentation can be logged and monitored from the control room. The Digidaq system was used to log the data received from the pore pressure transducers in the model. A live pore pressure data feed enabled precise control of the test initiation (as discussed in Section 4.3.6) and provided valuable insight to the performance of the transducers during the test.

Should a more detailed overview of the geotechnical centrifuge of the University of Pretoria be required, the reader is directed to Jacobsz *et al.* (2014). In their paper the authors cover the geotechnical centrifuge facility of the Department of Civil Engineering in detail.

4.3.3.2 Pore pressure transducers (PPTs):

The PPTs consisted of a small pressure sensor attached to a high-air-entry (HAE) ceramic disc (Figure 19a). The pressure sensor was a MS5407-AM high sensitivity Miniature SMD pressure sensor manufactured by Measurement Specialities. According to Le Roux (2013), the pressure sensor has an absolute pressure rating of seven bar and provides a high sensitivity output at high linearity. The HAE ceramic disc with an air entry value of (AEV) of three bar, was cut with a 7.26 mm coring drill bit and then filed down to a thickness of 4 mm.

4. Materials and Methods

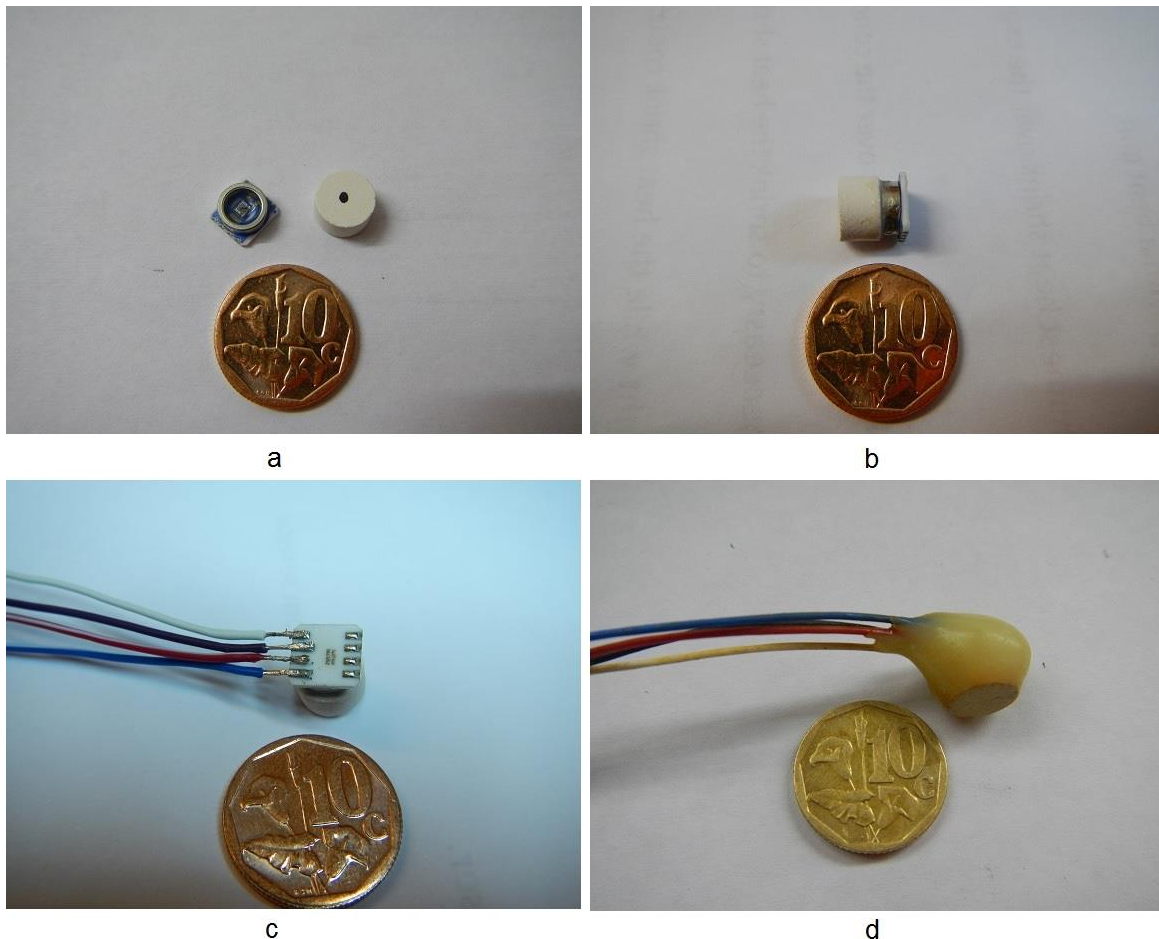


Figure 19: Components and construction process of the PPTs. (a) The HAE ceramic disc and pressure sensor. (b) HAE ceramic disc glued to the pressure sensor. (c) Electrical wires soldered to the back of the pressure sensor. (d) Complete PPT after curing of Loctite Hysol 94466 structural adhesive. The 10c coin used for scale has a diameter of 16 mm.

To construct the PPT, the HAE ceramic disc was secured to the pressure sensor with a quick set adhesive to create a small water reservoir between the sensor and the HAE ceramic (Figure 19b). After securing the ceramic disc, the electrical wires were connected (Figure 19c) and the entire assembly was insulated with Loctite Hysol 94466 A&B structural adhesive. The assembly was then allowed to cure until the adhesive hardened (Figure 19d). The design of the completed PPT is illustrated by Figure 20 below.

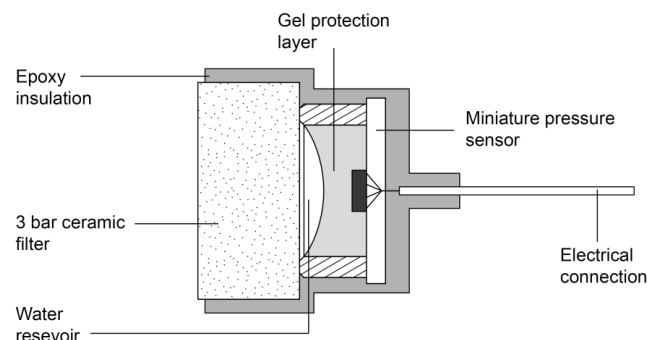


Figure 20: The pore pressure transducer design. Figure extracted from Le Roux (2013).

4. Materials and Methods

The saturation and calibration of the PPTs was carried out in a modified triaxial cell (Figure 21) as outlined by Le Roux (2013). The PPTs were stored in a sealed container filled with high quality deaired water after the saturation and calibration process and after each test. This ensured that the PPTs remained saturated before and after testing.



Figure 21: Pore pressure transducers being saturated and calibrated in the modified triaxial cell mentioned in Le Roux (2013).

As described in Section 4.3.1 the PPTs were spaced at known distances from each other within the backfill sample. This enabled the pore water pressures at discrete points within the model to be quantified and monitored throughout each test. Using the pore pressure values, the permeability of the material between the PPTs (i.e. each layer) could be calculated (Section 4.4.2). The PPTs were both small and highly sensitive and provided accurate pore pressure readings while causing minimum disturbance to the sample.

4.3.4. Material preparation

The backfill material sampled from LCM could not be used in its raw state in the model. As the model is a small scale representation of the prototype, any material that is large in comparison to the model dimensions, would need to be resized according to the scaling law for linear dimensions (Equation 9). Based on the particle size distributions (Section 5.1) a maximum particle size of 37.5 mm was recorded for the raw backfill samples. Modelling particles of this size in the centrifuge becomes impractical when addressing flow problems. As mentioned previously, the permeability will be controlled by the finer fraction of the material. Therefore, provided that the model and site material retained similar fractions of fine particles, the coarse particles could be removed from the model material without having a significant effect on the material permeability. By removing any coarse particles from the materials used



4. Materials and Methods

in the model, the materials could be viewed as a continuum where the permeability is a function of the fine fraction in the model material.

To ensure that model material retained an adequate degree of similarity (in terms of pore size and geometry) to the raw site material, only the coarsest particles were removed from the raw site material. This was achieved by only removing any particles larger than 4.5 mm from the site material during the preparation procedures. To prepare the model material, the procedures described below were followed for all of the site materials used, with the exception of the material used in the correlation. The site material for the correlation test was only oven dried and was not prepared in the same way as the other site materials.

To prepare the raw material for the model, the samples were removed from the bags and dried overnight in an oven set at 60°C. Once dried, the samples were passed through a sieve with a 4.75 mm mesh diameter. Any material retained in the sieve was lightly crushed with a 5lb hammer and then passed through the sieve again. This was repeated until the material retained in the sieve was too hard to be crushed. All material passing the sieve was placed in a sample bag for use in the model. In the prototype, the carbonaceous horizon is composed of a mixture between the slurry and discard. As the mixing ratio is not defined, the prepared discard and slurry material was combined at a 1:1 ratio to provide the material used for the carbonaceous horizon in the model.

4.3.5. Test configurations

Three different test configurations were carried out, each with different materials and different PPT placements. The purpose of each test as well as their configuration is discussed below.

4.3.5.1 Control test

As the name would suggest, the purpose of the control test was to validate the test methodology and verify the scaling laws applicable to the modelling of permeability in the centrifuge. To ensure that the number of variables in the test was limited, a uniform fine sand was used in this test. The grading curve of the sand is presented by Figure 28 in Section 5.1. As demonstrated by Figure 22, the model was packed with sand to 600 mm above the filter and three PPTs spaced at 200 mm intervals were placed into the sample. The bottom PPT was placed above the filter and the top PPT was placed 200 mm below the sample surface (Figure 22). The control test provided a valuable reference point for comparison with the other tests and assisted with the interpretation of the model behaviour (pore pressure data).

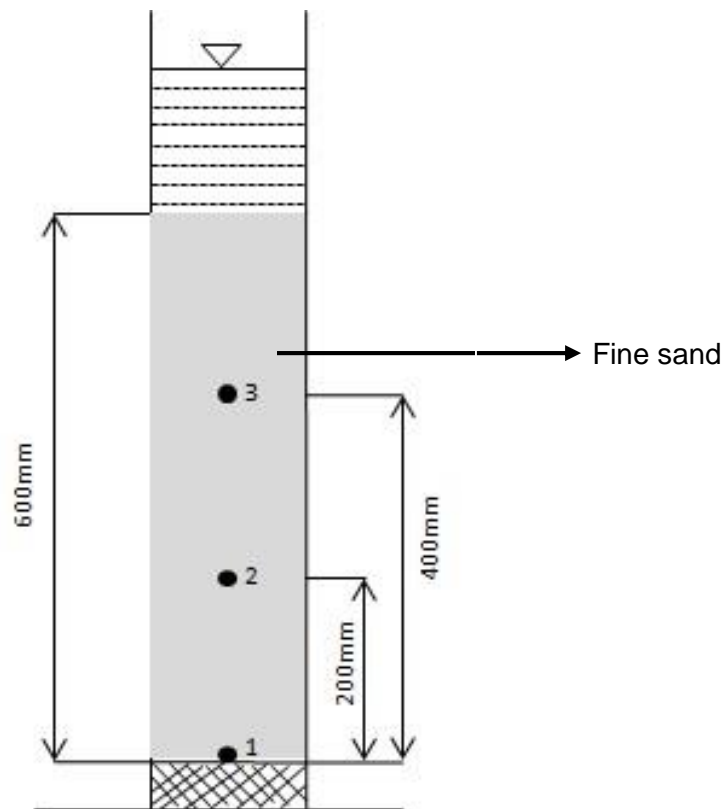


Figure 22: Control test configuration, with the PPT positions indicated by the respective numbers in the column.

4.3.5.2 Correlation test

The objective of the correlation test was to replicate the in-situ conditions of the site where the percolation tests were conducted. This allowed the K values obtained in the field to be correlated to the centrifuge K values. The reliability of the model for simulating seepage flow mechanisms could then be interpreted. This provided a rationale to appropriately relate the model results to the prototype. As mentioned in Section 4.1.2, the material sampled from the auger holes was used in the construction of the correlation test. Three PPTs were positioned in the sample with the same placement as the control test. Figure 23 illustrates the configuration of the correlation test.

4.3.5.3 Modelling full-scale profile

The full-scale test was constructed to simulate the geometry of the prototype. The prepared material sampled from each horizon was layered according to the model thicknesses presented in Table 2. The placement of the PPTs and the configuration of the full-scale model are illustrated by Figure 24. When conducting the first full-scale test, the cylinder with a 3mm wall thickness could not tolerate the high g levels and ruptured. Therefore, the cylinder with a 5mm wall thickness and inside diameter of 140mm was used for subsequent full scale tests.

4. Materials and Methods

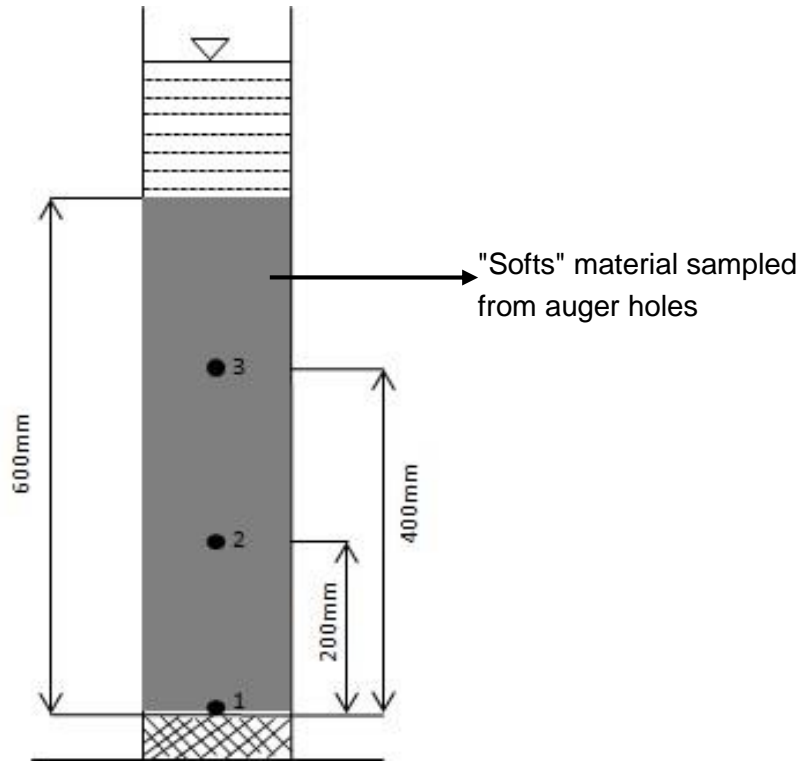


Figure 23: Correlation test configuration, with the PPT positions indicated by the respective numbers in the column.

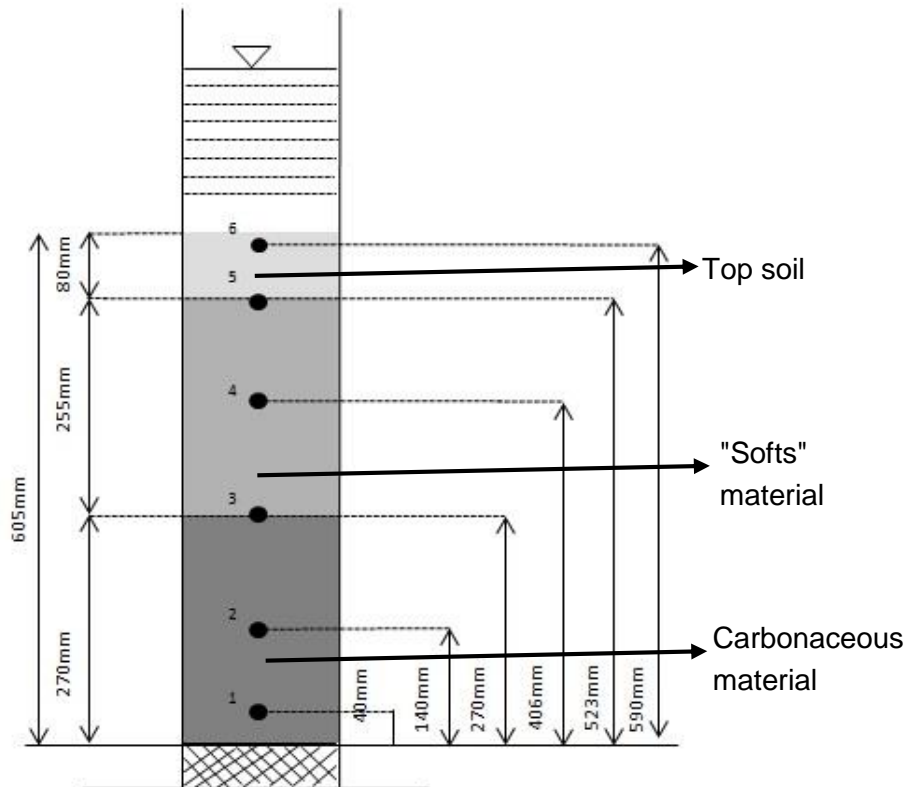


Figure 24: Full-scale test configuration, with the PPT positions indicated by the respective numbers in the column.

4.3.6. Test procedures

To construct each model the same process was followed. The filter was placed at the bottom of the cylinder and the cylinder was then secured in the strong box with the support system. To ensure that the PPTs did not de-saturate before the test commenced, they needed to be placed into a saturated sample. This was accomplished by filling the cylinder with deaired water up to the level where the PPT would be placed. The dry sample was then placed into the deaired water and allowed to settle around the PPT. This procedure was repeated until the sample/horizon reached the elevation designated by the configuration for each test. Before being placed into the sample, the sensitivity of the PPTs was tested. If a PPT was not adequately responsive then it was discarded.

When packing the full-scale model, each horizon was allowed to settle before the next layer was placed on top of it. This minimised contamination between the different layers and ensured that the thickness of each layer could be controlled. After the sample was packed, the cylinder was filled up to the top marker of the water head with deaired water. The annular space was filled with water and the solenoid valves were connected to the cylinder. At this point the assembly was weighed and placed onto the centrifuge platform, the solenoid valves were connected to the power supply and the PPTs were connected to the Digidaq interface. The small web camera was mounted to the frame of the centrifuge platform and positioned to monitor the fall in head above the sample. Finally, the centrifuge input parameters required for the setting of the counter weight position (Table 3) were set and the centrifuge was started.

Table 3: Centrifuge input parameters.

Acceleration	As per configuration
Payload	430kg
g height above platform	0.2m
Centre of mass height	0.25m

The test procedures for each configuration are described below. As explained in Section 4.4.3 the centrifuge acceleration needed to be adjusted to ensure that the required average acceleration was achieved throughout the model. Table 4 presents the set centrifuge and average accelerations for each test along with the simulated prototype height based on the average acceleration.



4. Materials and Methods

Table 4: The respective centrifuge accelerations (N_a), average acceleration throughout the model (N_r) and simulated prototype height (h_p) for each test configuration.

Test	Centrifuge acceleration (N_a)	Average acceleration (N_r)	Simulated h_p
Control	23g	19g	11.4m
Correlation	29g	23g	13.8m
Full-scale	35g & 70g	28g & 56g	16.8m & 33.6m

4.3.6.1 Control test

For the control test, the centrifuge was accelerated to 23g. Upon stabilising at 23g the pore pressures were monitored until they reached a stable/constant value. This indicated that all consolidation had taken place and that the falling head test could commence. The initial water level (h_1) was recorded and the solenoid valves were opened to initiate flow through the model. After opening the valves, the pressures rapidly dropped as flow commenced and then after some time reduced linearly, reflecting the falling water level in the cylinder. To determine if the flow through the model had reached a steady state, the pore pressures were monitored for a linear reading. After the water level had dropped sufficiently, the solenoid valves were closed and the final water level (h_2) was recorded. The pore pressures were again allowed to stabilise before the solenoid valves were opened for a second test run. After the second test run, the solenoid valves were closed and the pore pressures were allowed to stabilise before the centrifuge was stopped. Once the centrifuge had stopped, the sample thickness and final water level were recorded. The cylinder was again filled with deaired water and a falling head test was conducted under normal gravitational acceleration (1g). The initial water level was recorded and the solenoid valves were opened. The water level was allowed to fall to the same final level as the test at 23g before the solenoid valves were closed and the test completed.

4.3.6.2 Correlation test

As indicated by Table 4, the centrifuge was accelerated up to 29g for the correlation test. This ensured an average of 23g throughout the model and simulated the 14 m thickness of the "softs" horizon in the prototype. As with the control test, the pore pressures were allowed to stabilise before the falling head test was initiated. The correlation test followed the same procedures outlined in the control test above. However, due to the time taken for a single test run, only one falling head test was conducted. Also, due to the slow flow rate, no 1g test was conducted for the correlation test. After the centrifuge stopped, the sample thickness was recorded.

4.3.6.3 Modelling full-scale profile

For the full scale profile test, falling head tests were conducted at 35g (half scale) and 70g (full scale). The centrifuge was accelerated to 35g and the pore pressures were allowed to stabilise. The initial water level was noted and the solenoid valves were opened. After a

4. Materials and Methods

sufficient amount of steady state flow was allowed through the model, the solenoid valves were closed and the pore pressures allowed to stabilise again. The cylinder was topped up with water through the centrifuge water supply system and the pore pressures were again allowed to stabilise. The centrifuge was then accelerated to 70g. At this point the pore pressures were monitored and when they were stable, the solenoid valves were again opened. As in the previous tests, the water level was allowed to fall until a sufficient amount of steady state flow had passed through the model. The solenoid valves were closed and the pore pressures allowed to stabilise before the centrifuge was stopped.

4.4. Analysis Methods

The following section describes the analysis methods used throughout the investigation. The methods used to estimate the permeability of the model material and the processing of the pore pressure data are presented. Calculations used to assess the permeability of the field percolation tests are also considered. Furthermore, the calculation methods used to compute the required centrifugal accelerations are examined.

4.4.1. Calculating field permeability from percolation test data

During field percolation tests, the time taken for the hydraulic head in a cylinder placed on prepared ground to fall by 10 mm is recorded. The discharge for each 10 mm fall in head was calculated using the volume of the cylinder and the recorded time. Based on Darcy's law (Equation 3) and assuming a vertical hydraulic gradient of one, the discharge can be used to calculate the permeability (K) for each 10mm fall in head. This provided five K values for each run at a test position. The arithmetic mean of each run was calculated from these five K values. Since there were three runs conducted at each test site, this resulted in three averaged values for each of the test sites. To determine a single K value for each test site, the three run averages were again averaged to obtain the final K value for each of the four test locations.

4.4.2. Processing pore pressure data and calculating model permeability

To adequately explain the methods used to calculate the permeability from the pore pressure readings, Figure 25 has been used as a theoretical example. In the example, three PPTs have been evenly spaced in the sample, with one PPT at the bottom of the sample with a distance of l between the PPTs. The initial and final heads recorded before and after the tests are denoted by h_i and h_f respectively.

As described by Bernoulli's equation (Equation 1), the total head (H) at any point is the sum of the elevation head (h_z) and the pressure head (h_p) when flow velocity is disregarded. Under hydrostatic conditions before flow is initiated the total head (or hydrostatic potential) at any point in the cylinder will be equal to the total head at the bottom of the cylinder where the maximum pore pressure is measured.

Hence,

$$H = H_1 \quad (19)$$

And

$$H_1 = H_2 = H_3 \quad (20)$$

As the acceleration varies with radial distance from the centrifuge axis (as explained in Section 4.4.3 below), the elevation head cannot be simply measured as its elevation above the datum. By using the pore pressures, the elevation head for each PPT could be more accurately calculated. By rearranging Equation 1, the measured total head (H_i) can be used to calculate the elevation head at points 1 to 3 ($h_{z(1-3)}$) using the measured hydrostatic pore pressure ($h_{ps(1-3)}$) at each PPT.

$$h_{z(1-3)} = H_i - h_{ps(1-3)} \quad (21)$$

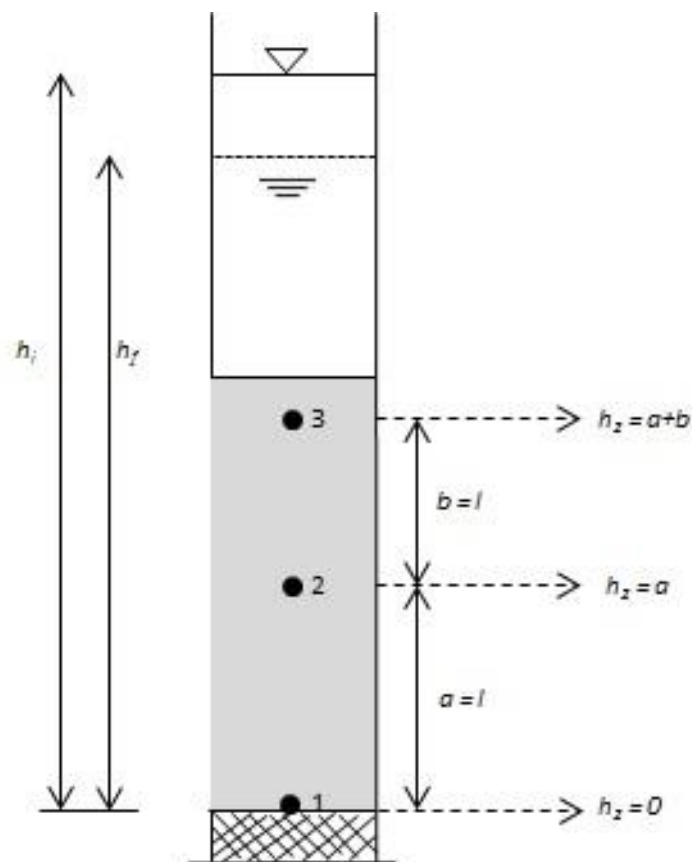


Figure 25: Theoretical model configuration used to demonstrate the estimation of K from pore pressure data.

After flow was initiated and steady state achieved, the measured pore pressure ($h_{pf(1-3)}$) from each PPT and their respective elevation heads ($h_{z(1-3)}$) as given by Equation 21, can be used to calculate the total head at each PPT during the falling head test ($H_{f(1-3)}$).

$$H_{f(1-3)} = h_{z(1-3)} + h_{pf(1-3)} \quad (22)$$

4. Materials and Methods

Therefore, the total head at each PPT during steady state flow was estimated and the difference in total head (ΔH) between two individual PPTs could be calculated. Based on the configuration of Figure 25, the calculation procedure described above is demonstrated in Table 5 below.

Table 5: Calculation procedure used to determine the difference in total head between two PPTs in the sample, based on the configuration of Figure 25.

PPT	Elevation (m)	Hydrostatic Conditions			Steady State Flow Established			ΔH (kPa)
		h_{ps} (kPa)	H (kPa)	h_z (kPa)	h_{pf} (kPa)	H_f (kPa)	h_z (kPa)	
3	a + b	h_{ps3}	$h_{ps1} = H_1$	$H_1 - h_{ps3} = x$	h_{pf3}	$h_{pf3} + x = H_{f1}$	x	N/A
2	a	h_{ps2}	$h_{ps1} = H_1$	$H_1 - h_{ps2} = y$	h_{pf2}	$h_{pf2} + y = H_{f2}$	y	$H_{f3} - H_{f2}$
1	0	h_{ps1}	$h_{ps1} = H_1$	$H_1 - h_{ps1} = 0$	h_{pf1}	$h_{pf1} + 0 = H_{f1}$	0	$H_{f2} - H_{f1}$

Using the measured ΔH to determine the permeability, Darcy's law can be rearranged to solve for K (Equation 23).

$$K = \frac{Q}{iA} \quad (23)$$

The discharge (Q) is determined using the internal area (A) of the cylinder and the fall in head recorded for the duration of the test ($h_i - h_f$). By using the measured difference in total head (ΔH) between two PPTs and the respective spacing (l) between these two PPTs, the hydraulic gradient (i) can be calculated (Equation 24).

$$i = \frac{\Delta H}{l} \quad (24)$$

However, the measurement units of the PPTs are expressed in kilo-Pascals (kPa), whereas, the formula units for Equation 24 is meters (m). Hence, the measured total head difference ($\Delta H = H_{f2} - H_{f1}$) is converted to meters by dividing the ΔH by the unit weight of water (γ_w) as demonstrated by Equation 25 below.

$$i = \frac{H_{f2} - H_{f1}}{\gamma_w l} \quad (25)$$

Combining Equations 23 and 25, the permeability of the sample can be calculated between any two given PPTs using Equation 26.

$$K = \frac{Q\gamma_w l}{A(H_{f2} - H_{f1})} \quad (26)$$

4.4.3. Calculation of centrifugal accelerations

As described by Taylor (1995), the inertial acceleration field (a) in the centrifuge is given by Equation 27. Hence, acceleration (a) is a function of the angular rotational velocity (ω) and the radius from the axis of rotation to any element in the model (r). Due to the height of the model above the platform, the inertial acceleration varies non-linearly along the height of the model. Thus, the set centrifugal acceleration (N_a) needs to be adjusted to achieve the desired

4. Materials and Methods

average acceleration (N_r) to simulate the prototype scenario. To determine the required centrifugal acceleration, the pore pressure distributions for a constant (N_r) and varying (N_a) inertial acceleration were compared.

$$a = \omega^2 r \quad (27)$$

For a constant inertial acceleration, the pore pressure will vary linearly with increasing depth in the model according to Equation 28. Hence, a straight line can be plotted for the variation of pore pressure with depth in the model (Figure 26).

$$P = \rho(9.81 \cdot N_r) \quad (28)$$

Where P is the pore pressure at a specific depth in the model, N_r is the required centrifugal acceleration which depends on the scale of the model, ρ is the density of water and h indicates the depth in the model.

However, as demonstrated by Equation 27, the inertial acceleration will vary according to the radius of a point measured from the axis of rotation. Hence, the pore pressure at any point within the model becomes a function of the inertial acceleration experienced at that point, due to its radius from the axis of rotation. Therefore, the pore pressure will vary non-linearly with depth throughout the model (See Figure 26). Accounting for the varying inertial acceleration with depth, Equation 29 can be derived from Equation 28.

$$dP = \rho \cdot \omega^2 r \cdot dr \quad (29)$$

Where dP indicates the pressure increase at a depth dr below the surface. Integrating Equation 29 from the water surface (r_0) to a distance r , both measured from the axis of rotation of the centrifuge:

$$P = \int_{r_0}^r \rho \omega^2 r \cdot dr \quad (30)$$

Hence:

$$P = \rho \omega^2 \frac{1}{2} r^2 \Big|_{r_0}^r \quad (31)$$

And the pore pressure at any given point in the model between r and r_0 can be calculated using Equation 32.

$$P = \frac{1}{2} \omega^2 \rho (r^2 - r_0^2) \quad (32)$$

Where: ω is calculated according to Equation 33 below and r_0 is the radial distance to the free water surface in the column measured from the axis of rotation.

$$\omega = \sqrt{\frac{N_a \cdot 9.81}{r}} \quad (33)$$

The question arises at which radial distance (measured from the axis of rotation of the centrifuge) the centrifuge rotation rate (N_a) should be calculated so that the non-linear water

4. Materials and Methods

pressure distribution would best match the desired linear pressure distribution. Figure 27 demonstrates a linear pore pressure distribution and varying pore pressure distribution obtained in the centrifuge resulting from the varying acceleration field. The set centrifugal acceleration (N_a) in Equation 33 was adjusted until the centrifugal pore pressure plot aligned sufficiently with the linear plot. Hence, by setting the centrifugal acceleration to the acceleration used in Equation 33, the desired average acceleration (N_r) needed to simulate the prototype will be distributed throughout the entire height of the model. As demonstrated by Figure 27, the plots do not match perfectly and there is both some over and under-stress. However, as Figure 27 illustrated these differences were small and were considered to be negligible.

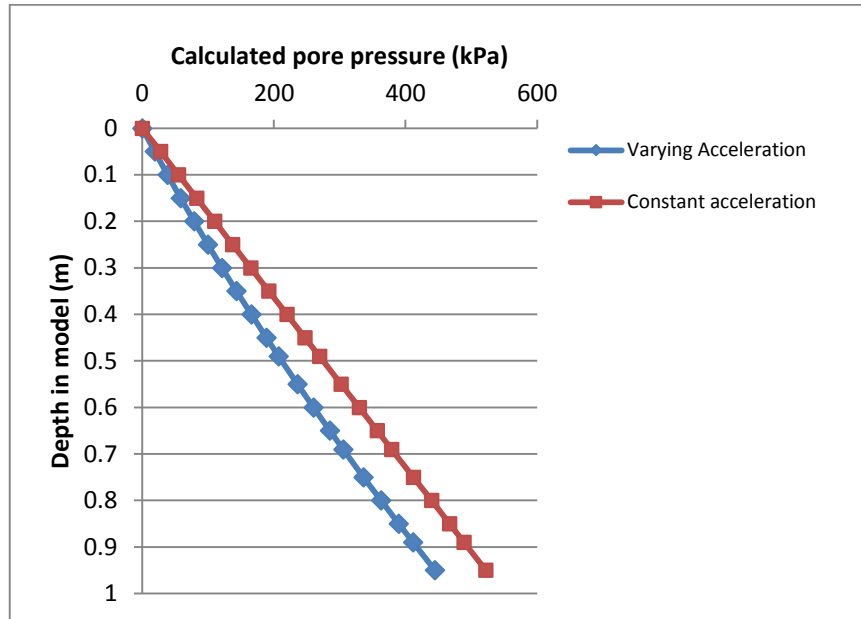


Figure 26: Calculated pore pressures throughout the model for a constant acceleration (N_r) of 56G and a varying centrifuge acceleration (N_a) of 56G.

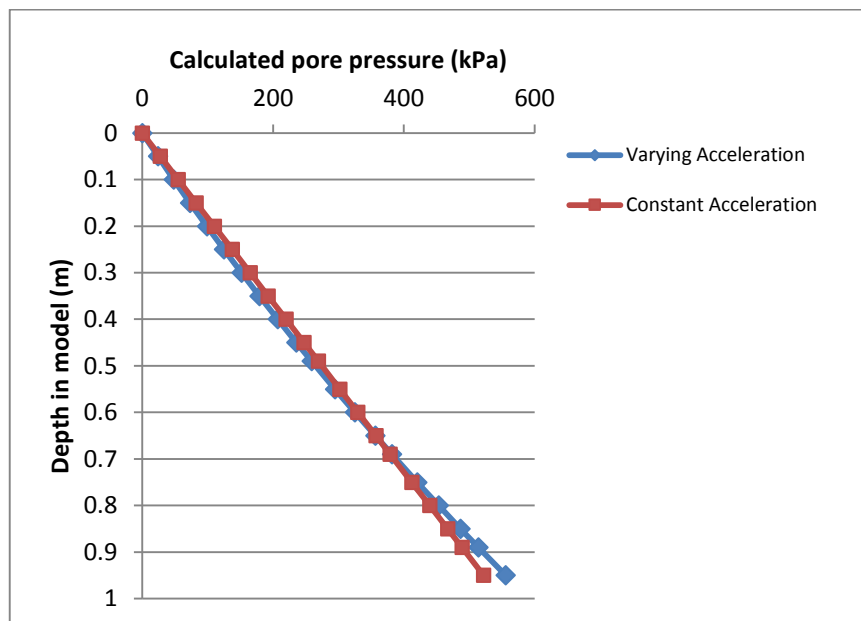


Figure 27: The pore pressures of the varying centrifuge acceleration are adjusted to fit the plot for a constant acceleration (N_r) of 56 G by increasing N_a to 70G.

5. Results

The data from the laboratory, field and centrifuge tests were compiled, processed and compared. The following section presents and discusses the respective test results in detail.

5.1. Particle Size Distributions

Particle size analyses were performed on all the site material sampled from LCM, the prepared material used in the model construction as well as the sand used in the control test. The following section presents the particle size distributions (PSD) for all the materials and a comparison between the PSD of the site material and prepared model material.

5.1.1. Control test material

The PSD for the control test material is presented in Figure 28 below. The material is well sorted and the particle sizes range from a coarse silt to a medium sand with a D50 size of 0.17 mm. The most abundant particle sizes are present in the fine sand range (0.06 mm - 0.2 mm), making up approximately 60% of sample. Furthermore, the sample has a smaller portion of particles in the medium sand fraction and a minor portion of particle in the coarse silt fraction. Hence, the control test material is well sorted but poorly graded and can be best described as a fine sand.

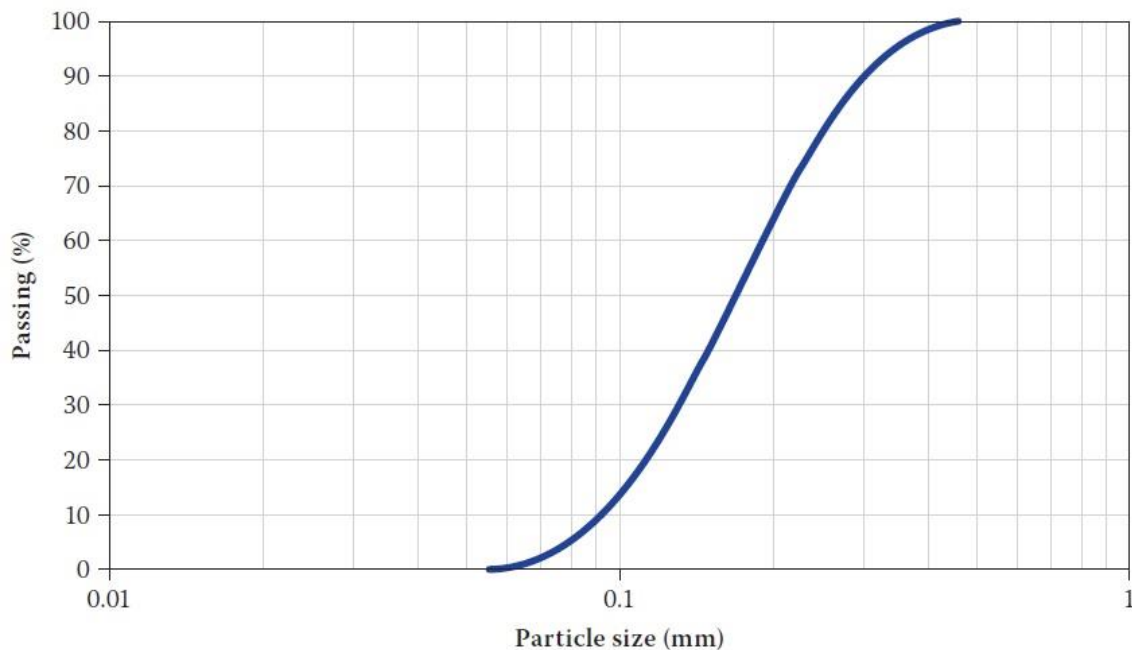


Figure 28: Grading curve for the sand used in the control test (Jacobsz, 2013).

5. Results

5.1.2. Correlation test material

As the model material for the correlation test was not prepared, the grading characteristics would be expected to be very similar to the site material. When analysing the PSD for the correlation test material (Figure 29) this is confirmed. The curves are almost identical and only differ slightly towards the lower portion (fine fraction) of the curves. The most abundant particle size appears to fall within the sand fraction (0.06mm - 2.0mm) for both curves, with a D50 size of 0.14 mm. This is confirmed when analysing the particle size fractions for each material (Table 6). Both materials have the largest percentage of their particles within the sand fraction. Additionally, both materials have almost equal amounts of silt and sand sized particles, with the model material only having 1% and 4% more particles in the silt and sand fractions respectively. However, the site material has 5% and 1% more particles than the model material in the clay and gravel fractions respectively.

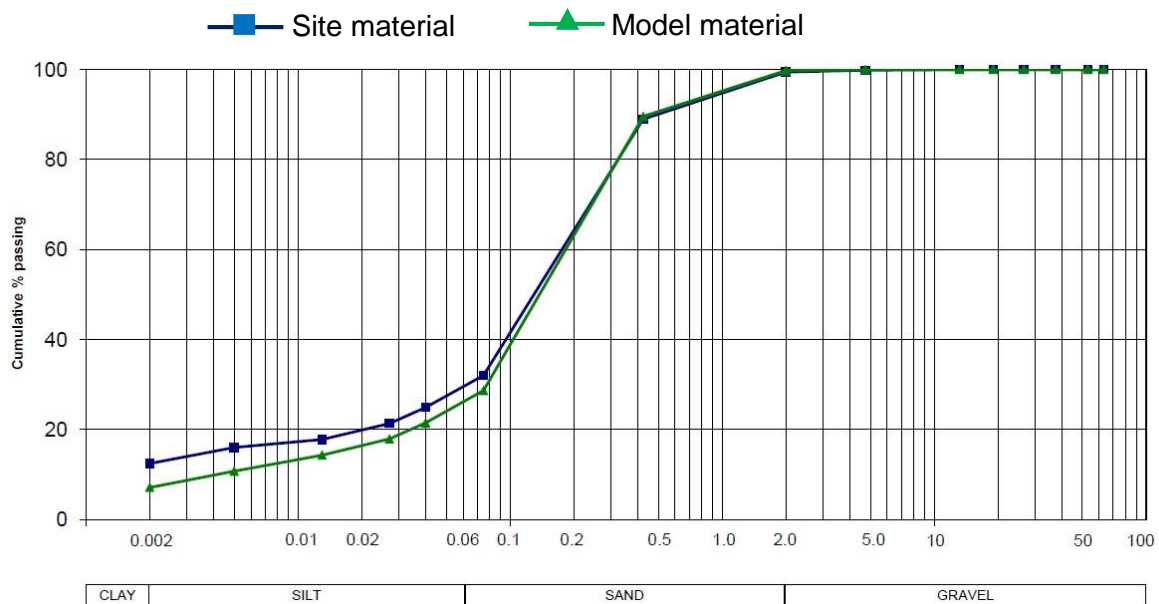


Figure 29: Grading curve comparison between the site material and test material for the correlation test.

Table 6: Relative particle size fractions for the site and model material of the correlation test

Correlation Test	Site Material	Model Material
% Clay	12	7
% Silt	17	18
% Sand	70	74
% Gravel	1	0
D50 (mm)	0.14	0.14

5. Results

5.1.3. Top soil material

Although the PSDs for the top soil (Figure 30) have a similar shape, they differ quite significantly in the upper section of the graph (gravel fraction). The grading curve of the model material displays no particles larger than 4.75 mm and only 2% of the total sample falling within the gravel fraction (Table 7). Additionally the model material has 10%, 7% and 3% more particles in the sand, silt and clay fractions respectively and a D50 size of 0.055 mm. Overall, the model material has the highest and second highest particle fractions in the sand, silt and clay fractions respectively. Conversely, the site material has its second highest particle abundance in the gravel fraction, has 21% more gravel sized particles than the model material and has a D50 size of 0.13 mm.

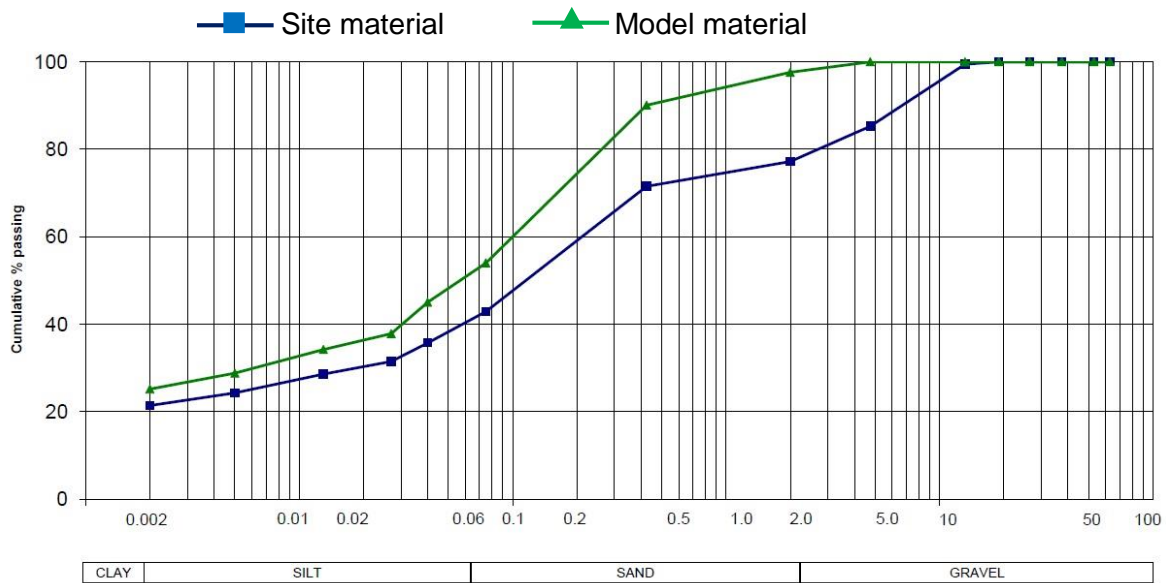


Figure 30: Grading curve comparison between the site material and test material for the top soil.

Table 7: Relative particle size fractions for the site and model top soil materials

Top Soil	Site Material	Model Material
% Clay	21	25
% Silt	18	25
% Sand	37	47
% Gravel	23	2
D50 (mm)	0.13	0.055

5. Results

5.1.4. "Softs" material

As with the top soil, the shape of the grading curves for the "softs" material are similar (Figure 31), but diverge significantly in the upper section of the graph. This is once again reflected in the 19% greater gravel content in the site material opposed to the 14% increase in sand content for the model material (Table 8). The clay content for both materials is in this case the same and the model material only has 5% more silt content than the site material. With a D 50 size of 0.17 mm the site material also has a slightly larger D50 size than the model material, which has a D50 size of 0.11 mm. However, both the site and model materials still retain the greatest portion of particles in the sand fraction and the grading curves have similar shapes.

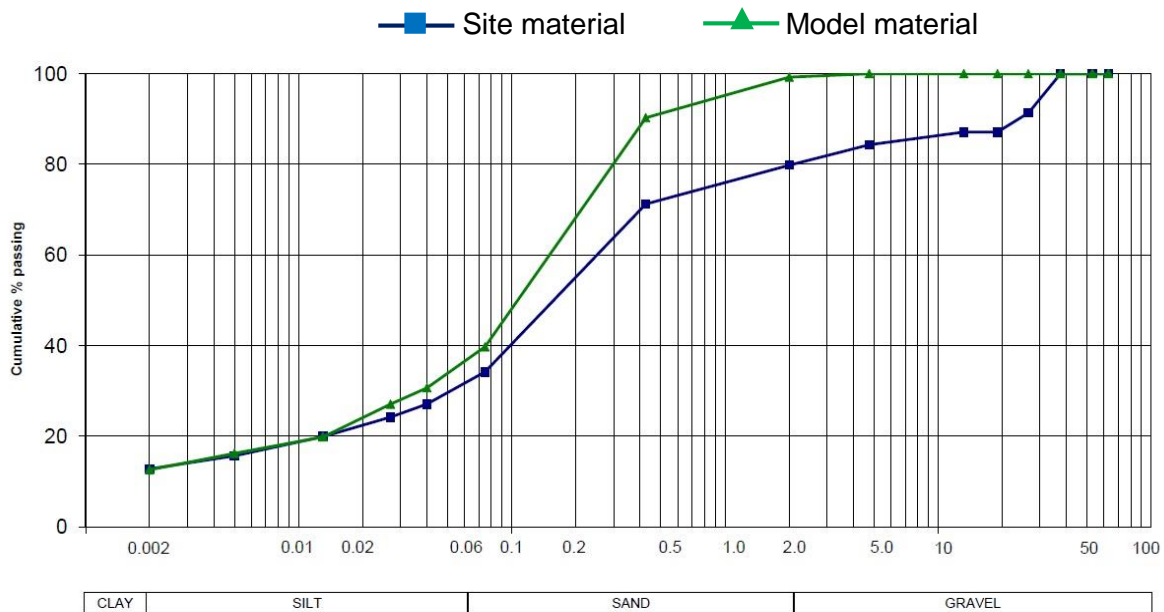


Figure 31: Grading curve comparison between the site material and test material for the "softs" material.

Table 8: Relative particle size fractions for the site and model "softs" materials

Softs	Site Material	Model Material
% Clay	13	13
% Silt	18	23
% Sand	49	63
% Gravel	20	1
D50 (mm)	0.17	0.11

5. Results

5.1.5. Slurry material

The grading curves of the slurry site and model materials differ significantly (Figure 32). The reason for this becomes apparent when comparing the relative particle size fractions and D50 size for the site and model materials in Table 9. The site material has the greatest abundance of particles (51%) in the gravel fraction. On the contrary, the model material only has a 1% gravel content and more than double the amount of particles in sand fraction (53%). Furthermore, the model material has 15% and 7% more silt and clay respectively than the site material. Hence, it is apparent that the preparation of the model material has significantly altered the grading characteristics of the slurry. The dramatic increase in sand, silt and clay and reduction of gravel has resulted in the overall classification of the slurry changing from a sandy gravel to a silty sand. Furthermore, with a D50 size of 0.08 mm for the model material, opposed to a D50 size of 2.0 mm for the site material, it is apparent that the mode material has a significantly larger fraction of fine material. It then follows that the hydraulic characteristics of the site and model materials are likely to differ significantly.

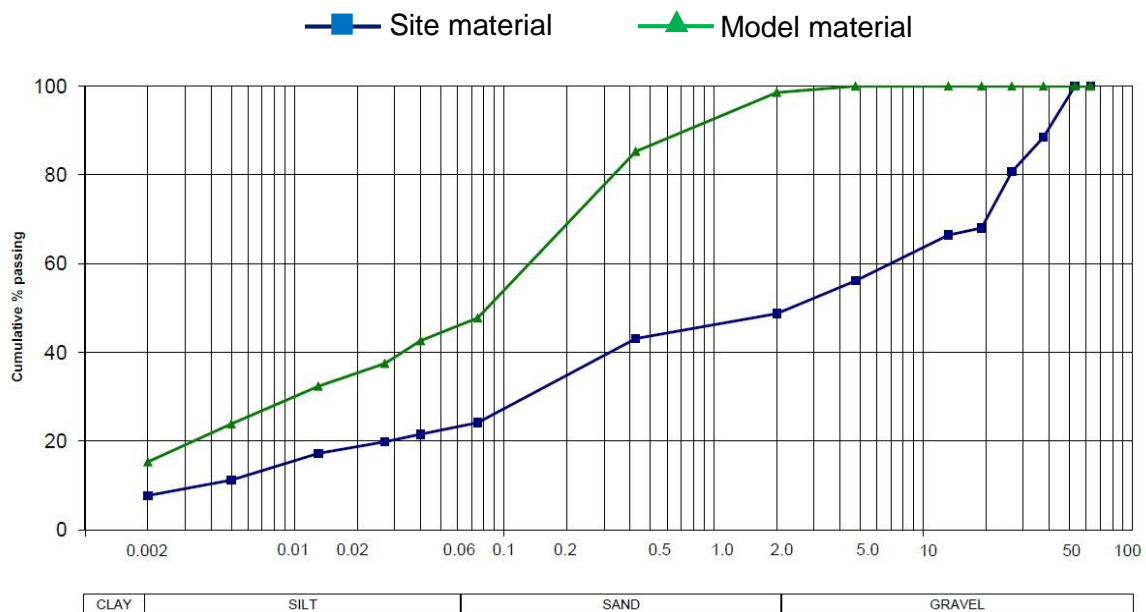


Figure 32: Grading curve comparison between the site and test slurry material.

Table 9: Relative particle size fractions for the site and model slurry material

Slurry	Site Material	Model Material
% Clay	8	15
% Silt	15	30
% Sand	26	53
% Gravel	51	1
D50 (mm)	2.0	0.08

5. Results

5.1.6. Discard material

As illustrated by Figure 33 the grading curves for the site and model discard material are similar in shape for the lower section but differ notably in the middle and upper sections of the graph. This is also reflected in the site material having a significantly higher D₅₀ size the model material (Table 10). The site material has 71% of its particles larger than 4.75mm and very few fine particles. Hence, the site material had a significant portion of large particles that needed to be crushed for the preparation of the model material. This again resulted in a reduction of the gravel content, but not to the same extent as with the slurry material.

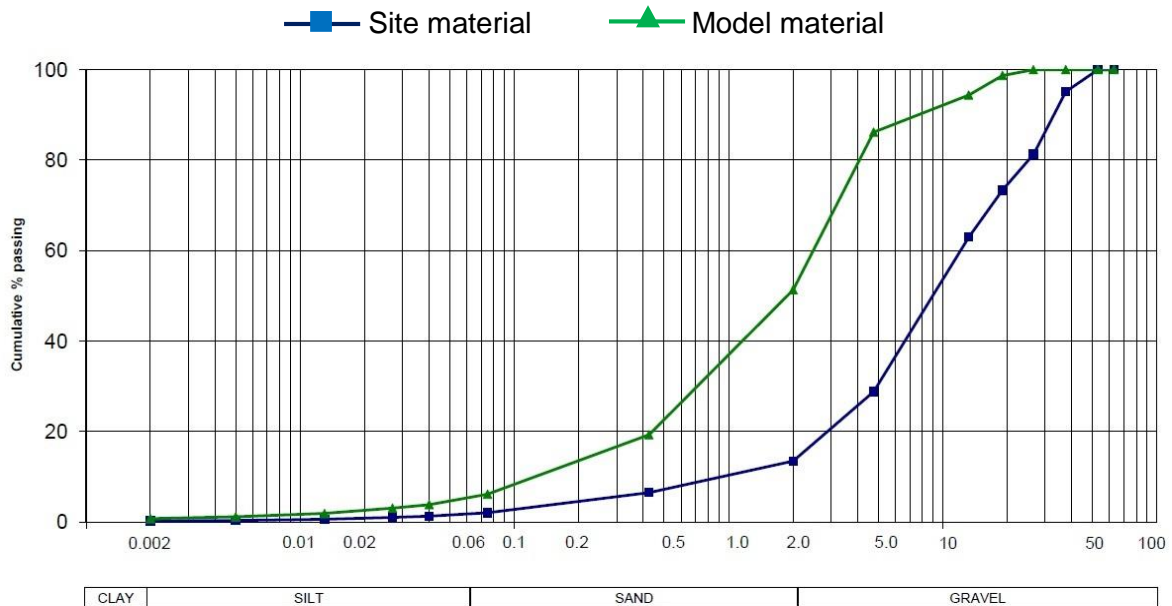


Figure 33: Grading curve comparison between the site and test discard material.

When comparing the particle size fractions in Table 10, it becomes apparent that there are significant differences between the sand and gravel fractions for each material. Compared to the 46% sand content of the model material, the site material only had 12% sand content. Similarly, the gravel content has been reduced from 86% in the site material to 49% in the model material. Therefore, as with the top soil, "softs" and slurry the sand content has been increased by reducing the gravel content when preparing the site material for the model.

Table 10: Relative particle size fractions for the site and model discard material

Discard	Site Material	Model Material
% Clay	0	1
% Silt	1	4
% Sand	12	46
% Gravel	86	49
D ₅₀ (mm)	9.0	1.8



5. Results

5.2. Field Percolation Tests

The calculated permeabilities from the field percolation tests are presented in Table 11 below. These values were used to obtain a baseline field value for comparison with an analogous centrifuge model (correlation test). As mentioned in Section 4.3.5.2 this comparison was used to assess the reliability of the centrifuge model in simulating the permeability of the backfill material. The data used to calculate the averages is presented in the Appendix. This includes the time-drawdown measurements, calculated discharges and permeabilities for each 10 mm drawdown of all the percolation tests.

Table 11: Calculated K values for the field percolation tests

Test Nr.	Average K (m/s)
1	1.793E-05
2	2.246E-05
3	1.208E-04
4	1.810E-05
Average	1.950E-05

As demonstrated by Table 11, with the exception of test number three, the calculated averages are very similar and fall within the same order of magnitude. The calculated permeability for test number three was considerably faster than the rest of the tests. Therefore, it is not considered to be a representative indication of the material permeability and is regarded as an anomaly/or outlier. The permeability of test number three was consequently excluded when calculating the average permeability of the percolation tests.

5.3. Centrifuge Tests

After the completion of the five centrifuge tests, the data collected from the instrumentation was organised and subsequently processed. Using the collected instrumentation data, pore pressure plots for each test were drawn and allowed for a visual assessment of the pore pressure behaviour during each centrifuge test. Following the methodology outlined in Section 4.4.2, the permeability between each PPT in all the models was calculated. The sample consolidation settlement and other notable characteristics were observed and recorded. The following section presents the data and results of the five centrifuge tests that were conducted.

5.3.1. Control test

As outlined in Section 4.3.6 the control test was carried out at both 23g and 1g. The instrumentation data, physical observations and calculation of ΔH and K for both the 1g and 23g tests are presented and described below.

5.3.1.1 Instrumentation data 23g test

The recorded pore pressure data for the control test at a centrifugal acceleration of 23g is presented in Figure 34 below. Once the centrifuge was started, the pore pressures immediately increased and stabilised rapidly when the centrifuge reached the required acceleration. Thereafter, the test was carried out in two separate runs and all the PPTs exhibited similar pore pressure responses as described below.

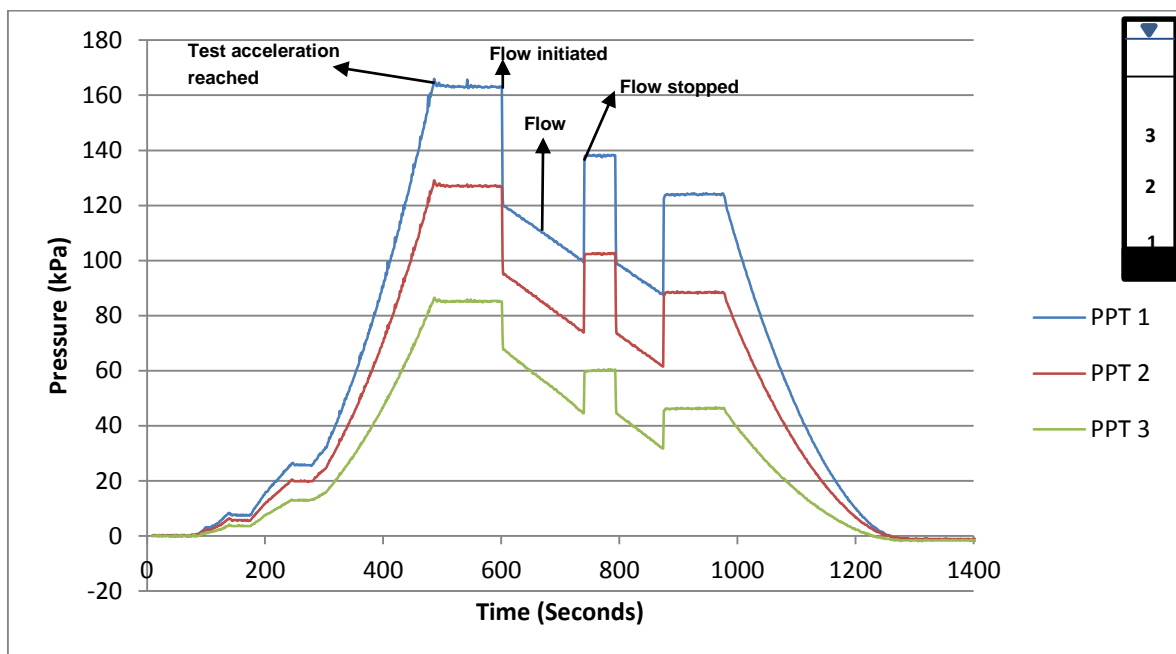


Figure 34: Recorded pore pressure data for the control test at a centrifugal acceleration of 23g, with the PPT positions illustrated by the diagram in the top right corner.

5. Results

As demonstrated by Figure 34, the initial pore pressures rapidly decreased after the solenoid valves were opened to initiate flow through the model. After the substantial initial pressure drop, the pore pressures decreased at a constant rate while steady state flow was maintained throughout the model. Once the solenoid valves were closed to stop flow through the model, the pore pressures rapidly restabilised at a pressure less than the pressure before the start of the test run due to the drop in water level during the flow period. Table 12 presents the pore pressure values of each PPT for the response described above.

Table 12 and Figure 34 reflects that the pore pressure readings are related to the elevation of the PPT in the model. At the bottom of the sample, PPT 1 experienced the maximum pore pressures when the solenoid valves were closed and the greatest drop in pressure when the valves were opened. For PPT 3 the opposite is true, as it experienced both the lowest pressures and smallest pressure drop at an elevation of 0.4 m above the filter. Placed at an elevation of 0.2 m between PPT 1 and 3, PPT 2 records intermediary pressures and pressure drops. During steady state flow, the highest and lowest pore pressures were still recorded by PPT 1 and 3 respectively.

Table 12: Pore pressures recorded for the control test at 23g.

PPT	Elevation (m)	Initial pressure before flow initiation 1 st Run (kPa)	Pressure Drop at flow initiation (kPa)	Restabilised Pressure after cessation of flow/ 2 nd Run Initial Pressure (kPa)	Pressure Drop at flow initiation (kPa)	Restabilised pressure after cessation of flow (kPa)
1	0	163.4	43.3	138	39	124
2	0.2	127.1	31.9	102.6	29	88.6
3	0.4	85	17.2	60.4	15.8	46.2

After the pore pressures restabilised at the end of the second run, the centrifuge was stopped and the pore pressures slowly decreased as the centrifuge decelerated. The fact that the pore pressures returned to their original value before the instrumentation panel was switched off confirms the validity of the readings during the test.

5.3.1.2 Instrumentation data 1g test

Pore pressure data recorded for the control test at 1g is illustrated in Figure 35 below. Due to the lack of a driving force due to the test being carried out at normal gravity, the pore pressures are significantly lower and the test took considerably more time than the 23g test. As a result of the lengthy duration taken for the test, only a single test run was completed. To maintain better resolution, only the portion of the graph illustrating the falling head test has been presented. The pore pressure behaviour was similar to that of the 23g test, where the highest and lowest initial and restabilised pore pressures were recorded by PPT 1 and 3 respectively. The pore pressure also dropped sharply when the valves were opened and then started to decrease at a constant rate during steady state flow reflecting the reducing water level. When closing the valves, PPT 2 and 3 restabilised in 3 seconds, whereas PPT 1 took 19 seconds to restabilise completely.

5. Results

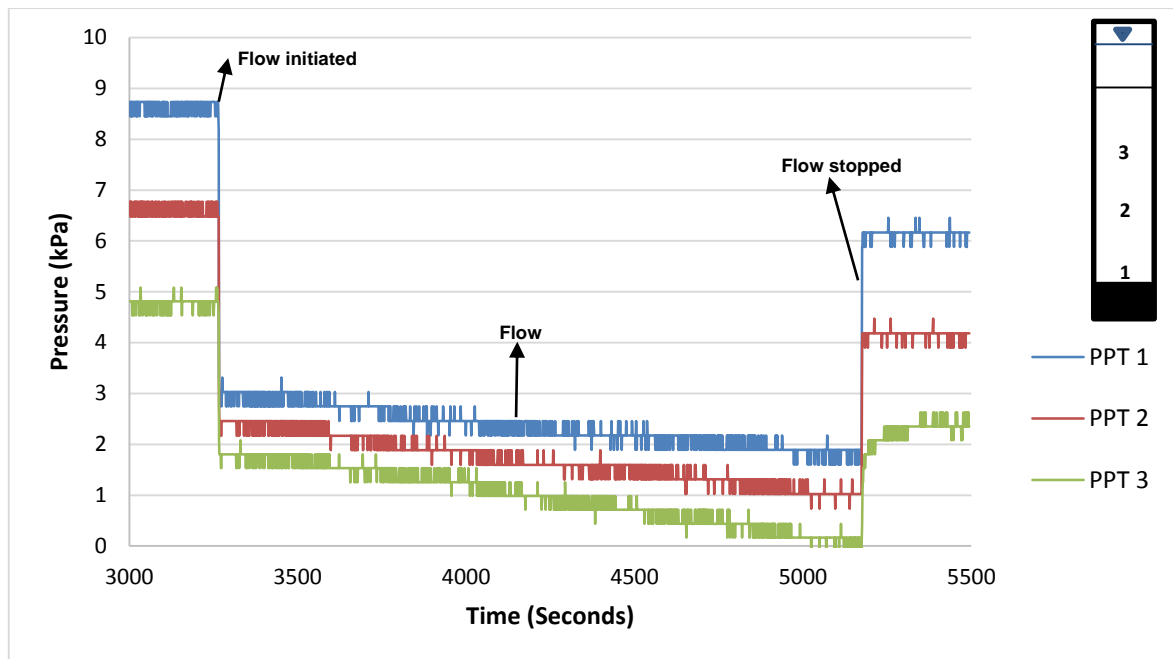


Figure 35: Recorded pore pressure data for the control test at 1g, with the PPT positions illustrated by the diagram in the top right corner.

Furthermore, as demonstrated by Table 13 the pressure drop follows the same trend as the 23g test. PPT 1 and PPT 3 again experience the greatest and smallest drop in pressure respectively. The graph also has a jagged appearance with many small spikes in pore pressure throughout the test due to the resolution of the PPTs.

Table 13: Pore pressures recorded for the control test at 1g.

PPT	Elevation (m)	Initial pressure before flow initiation (kPa)	Pressure Drop at flow initiation (kPa)	Restabilised pressure after cessation of flow (kPa)
1	0	8.731	5.7	6.167
2	0.2	6.769	4.309	4.184
3	0.4	4.807	3.002	2.351

5.3.1.3 Physical observations

Various physical observations were recorded before, during and after each test. These observations include the initial and final water levels, sample thickness before and after each test as well as the test time. The recorded observations for both the 23g and 1g test are presented in Table 14 below.

The initial and final sample thicknesses were taken before and after the test respectively. As the centrifuge was not stopped between runs, both the first and second run of the 23g test have the same initial and final sample thicknesses. The 1g test was conducted directly after the 23g test and the sample was unchanged. Hence, the initial and final sample

5. Results

heights correspond to the final sample height of the 23g test. A total settlement of only 4 mm was recorded for the control test.

For the 23g test a 0.14 m fall in head occurred during the 139 seconds of the first run and a 0.097 m fall in head occurred over the 82 seconds of the second run. Hence, the water head decreased by a total of 0.237 m in 222 seconds (3 min 42 sec) over the two separate runs. The 1g test was significantly slower and the water head fell by 0.24 m over 1911 seconds (31 min 51 sec).

Table 14: The recorded physical observations for the control tests at 23g and 1g.

Test	h_1 (m)	h_2 (m)	Test Time (sec)	Initial Sample Thickness (m)	Final Sample Thickness (m)
23g run1	0.89	0.75	139	0.594	0.59
23g run 2	0.75	0.653	82		
1g	0.9	0.66	1911	0.59	0.59

5.3.1.4 ΔH calculation: 23g test

Pore pressure values were extracted from the first run in Figure 34 and used to calculate ΔH between each PPT in the sample. The results are presented in Table 15 below. A maximum ΔH was calculated between PPT 3 and 1 which were 0.4 m apart. The second highest ΔH was calculated for the middle portion of the sample between PPT 2 and 3. The lowest ΔH was calculated between PPT 1 and 2 at the base of the sample. Therefore, the ΔH increases with the distance separating the PPTs and decreases slightly with depth from the top of the sample.

Table 15: The calculated change in total head between each PPT for the control test at 23g

PPT	Elevation (m)	Hydrostatic conditions			Steady state flow established			ΔH (kPa)
		h_{ps} (kPa)	H (kPa)	h_z (kPa)	h_{pf} (kPa)	H_f (kPa)	h_z (kPa)	
3	0.4	85	163.4	78.36	67.8	146.16	78.36	26.06
2	0.2	127.1	163.4	36.34	95.2	131.54	36.34	14.62
1	0	163.4	163.4	0	120.1	120.1	0	11.4

5.3.1.5 ΔH calculation: 1g test

As the model was not accelerated during the 1g test, pore pressure values were extracted from Figure 35 during steady state flow and converted to a pressure head in meters through division by the unit weight of water (9.81 kN/m³). Then by adding the respective elevation of each PPT, the total head was calculated for each PPT and then subsequently used to determine the change in total head (ΔH) between each PPT. The results are presented in Table 16 below. The calculated ΔH for both the lower and middle portions of the sample are very similar and only differ by 0.0082 m. Despite this minor difference, the lower portion of the sample had a slightly larger ΔH than the middle portion of the sample. Hence, the ΔH

5. Results

decreases slightly with elevation. The calculated ΔH for the 0.4 m separating PPT 1 and 3 was the greatest and as with the 23g test, ΔH increases with the distance separating the PPTs.

Table 16: The calculated change in total head between each PPT for the control tests at 1g

PPT	Elevation (m)	Steady State Flow Established				
		h_{pf} (kPa)	h_{pf} (m)	H_f (m)	h_{pz} (m)	ΔH (m)
3	0.4	1.81	0.1845	0.5845	0.4	0.2756
2	0.2	2.46	0.2508	0.4508	0.2	0.1337
1	0	3.03	0.3089	0.3089	0	0.1419

5.3.1.5 Model permeability

Using the data presented in Table 14 (drop in water level with the cross-sectional area of the cylinder), the volumetric discharge (Q) was calculated for each test. Together with the calculated ΔH from Tables 15 and 16, Q was used to calculate the K values between each PPT in the sample. The K values calculated between each PPT are presented in Table 17 below. Although the values do not vary significantly, there are some differences between the K values calculated for the two tests. For the 23g test the lowest K value was calculated between PPT 2 and 3 for the middle portion of the sample. The highest K value was calculated for the lower portion of the sample between PPT 1 and 2. Conversely, the 1g test showed an inversion of the calculated maximum and minimum K values. The lowest K value was calculated between PPT 1 and 2 and highest K value between PPT 2 and 3. Hence, it appears that the K value decreases with elevation for the 23g test and increases with elevation for the 1g test.

Table 17: Calculated permeability between each PPT for the 23g and 1g tests using the pore pressure data from the PPTs

Test	PPT	l (m)	Q (m ³ /s)	A (m ²)	γ_w (kN/m ³)	ΔH (kPa)	K_m (m/s)
23g Run 1	1 to 2	0.2	1.631E-05	0.0163	9.81	11.44	1.716E-04
	2 to 3	0.2				14.62	1.343E-04
	1 to 3	0.4				26.06	1.507E-04
	PPT	l (m)	Q (m ³ /s)	A (m ²)	i	ΔH (m)	K_m (m/s)
1g	1 to 2	0.2	2.017E-06	0.0163	0.7095	0.1419	1.822E-04
	2 to 3	0.2			0.6687	0.1337	1.933E-04
	1 to 3	0.4			0.6891	0.2756	1.876E-04

The calculated K values for both the 1g and 23g test are very similar and all fall within the same order of magnitude. Table 18 provides a comparison of the differences in the calculated K values for each test. Average K values of 1.522E-04 m/s and 1.877E-04 m/s are calculated for the 23g and 1g test respectively. These averages are very similar when seen in the context of permeability values, with the 1g test average being only 1.233 times greater than that of the 23g test. Hence, the applied inertial acceleration in the centrifuge appears to have

5. Results

had a minimal effect on the calculated K value of the sample due to compression of the material at high accelerations.

Table 18: Calculated difference in K values between the 1g and 23g tests.

PPT	K 23g	K 1g	K 1g/ K 23g
1 to 2	1.716E-04	1.822E-04	1.062
2 to 3	1.343E-04	1.933E-04	1.440
1 to 3	1.507E-04	1.876E-04	1.245
Average	1.522E-04	1.877E-04	1.233

5.3.2. Correlation test

To simulate the site conditions, the model for the correlation test was subjected to a centrifugal acceleration of 29g ($N_r = 23g$). The instrumentation data, physical observations and calculated permeability of the correlation test are presented below. To determine the validity of the model methodology, the calculated model permeability is compared to the field permeability from the percolation tests.

5.3.2.1 Instrumentation data

The pore pressure measurements for the correlation test are presented in Figure 36. To increase the resolution of the graph, the time scale has been reduced to only display the falling head part of the test. The graph presents noteworthy insight to the pore pressure and settlement behaviour of the "softs" material.

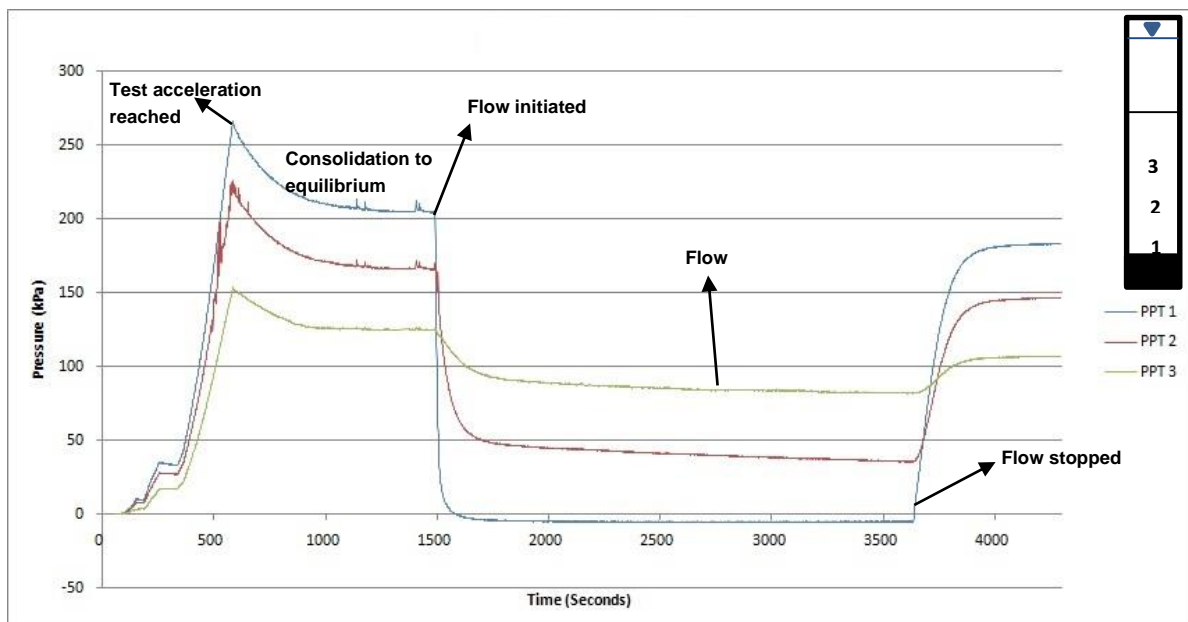


Figure 36: Recorded pore pressure data for the correlation test at $N_r = 23g$, with the PPT positions illustrated by the diagram in the top right corner.

5. Results

Initially the pore pressures increased at a constant rate while the centrifuge accelerated. PPT 2 displayed some interference during this period, but quickly readjusted to a constant rate. When the centrifuge reached the required acceleration (N_a) of 29g the pore pressures reached their maximum value. After the maximum values were attained, the pore pressures gradually started to decrease as the sample slowly consolidated. After the sample consolidated completely and the pore pressures dissipated, the curves flattened out and reached a stable pore pressure reading. As the curves of PPT 1 and 2 are stabilising, there are two distinct spikes in the pore pressures at the same time interval. A similar double spike is observed just before the valves are opened. These spikes may possibly be attributed to a sudden rearrangement of a large lump of particles as the sample settles.

The measured pore pressures for each PPT throughout the test (at specific time intervals) are presented in Table 19 below. PPT 1 measured the largest maximum pressure (266.4 kPa), followed successively by PPT 2 and PPT 3. After stabilising to a constant value, the maximum and minimum pore pressures were still measured by PPT 1 and 3 respectively. However, the time taken for pore pressure to dissipate while the sample was consolidating differs significantly for each PPT. At the bottom of the sample, it took PPT 1 618 seconds before a constant value was attained. The measured pore pressures closer to the top of the sample (PPT 3) stabilised after only 386 seconds. As with the pore pressure measurements, PPT 2 stabilised after an intermediate time of 488 seconds. Therefore, both the measured pore pressures and recorded consolidation times increase with depth in the model.

Table 19: Pore pressures measured for the correlation tests.

PPT	Elevation (m)	Max pressure (kPa)	Initial pressure before flow initiation (kPa)	Pressure drop after flow initiation (kPa)	Restabilised pressure after cessation of flow (kPa)
1	0	266.4	204.2	204.2	182.81
2	0.2	223.7	165.58	116.7	146.32
3	0.4	153.7	124.43	32	106.65

After consolidation settlement was completed and the pore pressures had dissipated and stabilised to their equilibrium (initial) pressures (Table 19), the valves were opened and each PPT exhibited slightly different pore pressure behaviours. As illustrated by Figure 36, PPT 1 had the quickest response and the greatest drop in pore pressure when the valves were opened. In 91 seconds the pore pressure dropped to zero. Thereafter, steady state flow was achieved and the pore pressure gradually decreased at a constant rate. Approximately 259 sec after the valves were opened, the pore pressure became constant and PPT 1 measured pore pressures between -4.56 kPa and -5.13 kPa for the remainder of the falling head test. Decreasing by 116.7 kPa in 229 sec., PPT 2 had the second fastest response and largest drop in pore pressure when the valves were opened. After the initial drop, the pore pressure slowly decreased at a constant rate for the rest of the falling head test. PPT 3 measured the smallest drop in pore pressure (32 kPa) and takes the longest (249 sec) to reach a new equilibrium when the valves were opened. As with PPT 2, the pore pressure also slowly decreased at a constant rate once steady state flow is achieved at PPT 3. During steady state flow conditions, the distribution of the hydrostatic pore pressures seems to have been inverted. PPT 3 now

5. Results

measured the highest pore pressure and PPT 1 now measured the lowest pore pressure. PPT 2 still measured an intermediate pore pressure but had also dropped below PPT 3. Based on the above observations, both the response time and pore pressure measurements appear to correlate to the elevation of the PPT in the sample. Although recording a greater decrease in pressure, PPTs situated closer to the bottom of the sample also responded faster and reached steady state flow quicker than PPTs positioned at higher elevations in the sample. Hence, the pore pressure increases, while the response time decreases with elevation when the valves are opened.

When the valves were closed, the pore pressures restabilised so that PPT 1 and 3 once again recorded the maximum and minimum pore pressure respectively (Table 19). PPT1 was again the fastest and PPT 3 the slowest to respond and stabilise after the valves were closed. Therefore, pore pressures and response time once more decreased with elevation when the valves were closed at the end of the test.

5.3.2.2 Physical observations

As with the control test numerous physical observations were made during the correlation test. The configuration of the correlation test after centrifugation is illustrated by Figure 37 and the recorded observations are presented in Table 20 below.

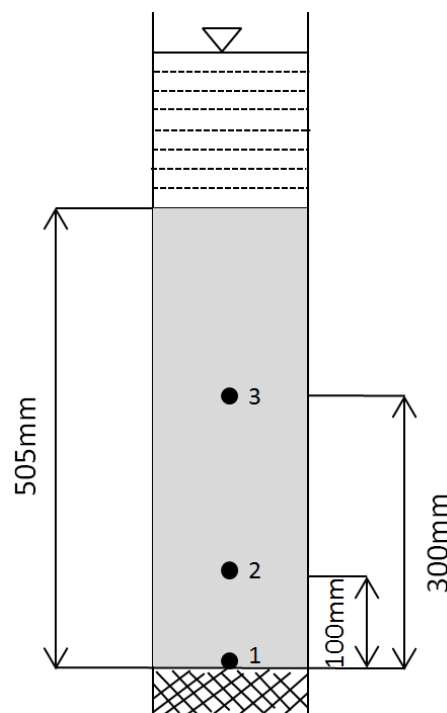


Figure 37: Configuration of the correlation test after centrifugation.

With only a 9.05 cm fall in head occurring over 2142 seconds (35 min 42 sec) the test took significantly longer than the 23g control test. During the test the sample had settled significantly and a total settlement of 8.5 cm was measured at the end of the test.

Table 20: The recorded physical observations for the correlation test

Test	h_1 (m)	h_2 (m)	Test time (Sec)	Initial sample thickness (m)	Final sample thickness (m)
Correlation	0.8895	0.799	2142	0.59	0.505

As a result of the amount of settlement that had occurred, the PPT cables exiting the model were pulled tight. Hence, the PPTs must have moved with the sample as it settled, resulting in the spacing between the PPTs being changed. To measure the spacing of the PPTs after the test, the cables were marked at the point where they were aligned with the top of the Perspex cylinder. The distance between the marker and the bottom of the PPT was then measured to determine by how much the PPT had moved and to confirm its position in the sample. As PPT 1 was placed above the filter, it could not move and stayed in its original position. However, PPT 2 and PPT 3 had each moved by 100mm and after the sample had settled, were positioned at 100mm and 300mm above the filter respectively.

5.3.2.3 ΔH calculation

Pore pressure values were extracted from Figure 36 and used to calculate ΔH between each PPT in the sample. The results are presented in Table 21 below. The ΔH calculated for the 0.3 m separating PPT 3 and 1 was the maximum for the sample and was significantly larger than the rest of the values. The second highest ΔH was calculated for the middle of the sample between PPT 2 and 3. Between PPT 1 and 2 at the base of the sample, the lowest ΔH was calculated. Hence, as with the control test ΔH increased with the distance separating the PPTs. As the bottom portion of the sample records a smaller ΔH than the middle portion, the ΔH decreased slightly with depth from the top of the sample.

Table 21: The calculated change in total head between each PPT for the correlation test

PPT	Elevation (m)	Hydrostatic Conditions			Steady State Flow Established			ΔH (kPa)
		h_{ps} (kPa)	H (kPa)	h_{pz} (kPa)	h_{pf} (kPa)	H_f (kPa)	h_{pz} (kPa)	
3	0.3	124.4	204.2	79.8	81.77	161.57	78.8	166.4
2	0.1	165.6	204.2	38.6	35.64	74.24	38.6	87.33
1	0	204.2	204.2	0	-4.845	-4.845	0	79.085

5.3.2.4 Model permeability and comparison to field K values

Using the data presented in Table 20, the volumetric discharge (Q) was calculated. Together with the calculated ΔH from Table 21, Q was used to calculate the K values between each PPT in the sample. The K values calculated between each PPT are presented in Table 22 below. The values calculated for the sample do not vary significantly and all fall within the same order of magnitude. However, the calculated K values do vary slightly throughout the sample height. The middle portion of the sample between PPT 2 and 3 had the highest calculated K value. The lowest K value was calculated for the bottom portion of the sample between PPT 1 and 2. The K value calculated between the bottom (PPT 1) and top PPT (PPT 3) represents an average K value for the sample separating the PPTs. Based on the above

5. Results

observations, the permeability of the sample increased slightly with elevation and distance separating the PPTs.

Table 22: Calculated permeability between each PPT for the correlation test using the pore pressure data from the PPTs.

Test	PPT	l (m)	Q (m ³ /s)	A (m ²)	γ_w (kN/m ³)	ΔH (kPa)	K_m (m/s)
Correlation	1 to 2	0.1	7.230E-07	0.0163	9.81	79.09	5.5E-07
	2 to 3	0.2				87.33	9.97E-07
	1 to 3	0.3				166.4	7.84E-07

To confirm the accuracy of the centrifuge modelling methodology, the centrifuge test results are compared to the field percolation test results in Table 23 below. The calculated field permeability is significantly larger than the calculated model permeability. As demonstrated in Table 23, the calculated field permeability is two orders of magnitude greater than the average calculated with the PPTs. Therefore, it appears that the centrifuge model underestimates the permeability of the material. However, the difference is not so great that it cannot be reasonably explained by the physical properties of the model, test observations and methodology. A full discussion of the model reliability in simulating the in-situ conditions and the interpretation of the results presented in Table 23 will follow in Section 6.3.2.2.

Table 23: Comparison of the calculated average for the field percolation tests and the permeability calculated for the model using the PPTs.

Field average(m/s)	PPT average(m/s)
1.950E-05	7.771E-07

5.3.3. Modelling full scale profile

As outlined in Section 4.3.6 the tests modelling the full scale profile were carried out at both 70g and 35g. The instrumentation data, physical observations and calculation of ΔH and K for both the 35g and 70g tests are presented and described below.

5.3.3.1 Instrumentation data: 35g test

The instrumentation data for the full scale test conducted at 35g is illustrated by Figure 38 and the measured pore pressures for specific time intervals are presented in Table 24 below. As with the previous tests, the pore pressures increased at a constant rate while the centrifuge was accelerating. When the centrifuge reached 35g all the PPTs, with the exception of PPT 6, recorded their maximum pore pressures before slowly decreasing as the sample consolidated. The measured pore pressures correlated with elevation, decreasing successively from the greatest pore pressure at PPT 1 to the lowest pore pressure at PPT 6. After all the pore pressures had almost stabilised, PPT 3 suddenly starts to decrease. The pore pressures continued to decrease and dropped to the lowest recorded pore pressure before the valves were opened. PPT 5 and 6, positioned in the topsoil, do not appear to have experienced much consolidation at all. PPT 5 only decreased slightly after reaching its maximum pore pressure and stabilised quickly thereafter. While recording the lowest pore pressure, PPT 6

5. Results

seems to not have been affected by consolidation settlement, as the pore pressures continued to increase slightly before stabilising. PPTs 1, 2 and 4 display the greatest amount of consolidation settlement, as the pore pressures decreased significantly before stabilising.

Once the pore pressure had dissipated, the valves were opened to initiate flow at about 3000 seconds and each PPT displayed slightly different pore pressure behaviours. In response to the valves being opened, the pore pressures at each PPT increased initially before decreasing. As demonstrated by Table 24, the decrease in pore pressure appears to be related to the elevation of the PPT. The smallest drop in pore pressure was experienced by PPT 6, increasing successively to the largest drop experienced by PPT 1. Again the sensor closest to the valve (PPT 1) responded the quickest and attained steady state flow before the other PPTs. After the initial steep drop in pore pressure, PPTs 1, 2 and 4 stabilised and started to decrease at a constant rate as the water level gradually decreased during steady state flow. Conversely, the pore pressures at PPT 5 and 6 did not decrease sharply when the valves were opened. Initially the pore pressures increased slightly and then started to slowly decrease at a constant rate as steady state flow was achieved. The behaviour of PPT 3 was completely different from the rest of the sensors in the sample. After initially increasing when the valves were opened, the pore pressure dropped sharply and then increased slowly before stabilising at a pore pressure between that measured by PPT 4 and 2. Thereafter, PPT 3 behaves in a similar manner to the rest of the PPTs as the pore pressure started to decrease at a constant rate during steady state flow.

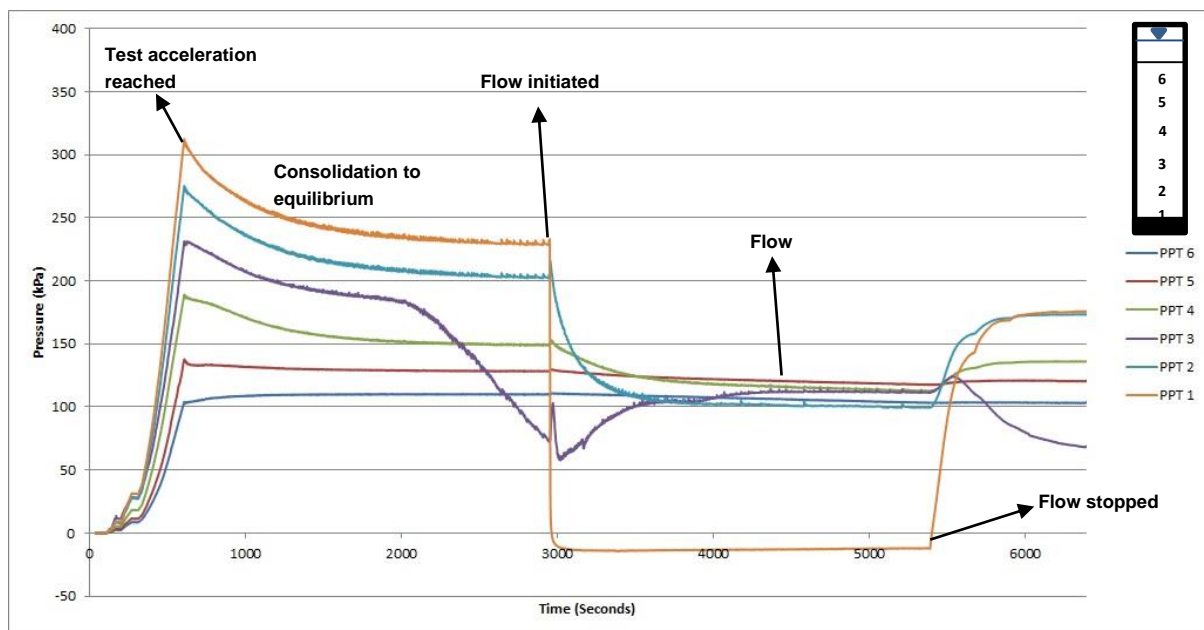


Figure 38: Recorded pore pressure data for the full scale test at 35g, with the PPT positions illustrated by the diagram in the top right corner.

As highlighted by Figure 38, the distribution of the hydrostatic pore pressures seems to have been inverted during steady state flow conditions. PPT 5 now measures the highest pore pressure and PPT 1 now measures the lowest pore pressure. With the exception of PPT 6, the pore pressures now increase successively with elevation from PPT 1 to 5. PPT 6 measured a lower pore pressure than PPT 5 and consequently the pore pressure decreased slightly with elevation between PPT 5 and 6. Another observation that can be made during

5. Results

steady state flow is the apparent convergence of the measured pore pressures. With the exception of PPT1, the measured pore pressures vary within a range of only 18.3 kPa during steady state flow. Conversely, there is a difference of 111.6 kPa between PPT 1 and PPT 2.

Table 24: Measured pore pressures for the full scale test at 35g.

PPT	Elevation (m)	Maximum pressure (kPa)	Initial pressure before flow initiation (kPa)	Pressure drop upon flow initiation (kPa)	Restabilised pressure after cessation of flow (kPa)
1	0.085	312.5	229.2	239.4	175.6
2	0.1775	275.4	202.6	82	173.5
3	0.29	231.6	73.28	n/a	68.8
4	0.3905	189.1	149.2	17.3	136
5	0.5065	137.9	128.5	0.8	120.9
6	0.573	110.4	110.2	0.6	103.8

At the end of the test the valves were closed and the pore pressures allowed to restabilise. With the exception of PPT 3 that once again exhibited anomalous behaviour, PPT 1 and 6 once more recorded the maximum and minimum pore pressures respectively (Table 24). Hence, the pore pressure once again decreased successively with elevation, except for PPT 3. After initially increasing when the valves were closed, the pore pressures measured by PPT 3 decrease to a minimum of 68.8 kPa before the start of the 70g test.

5.3.3.2 Instrumentation data: 70g test

Directly after the 35g test was completed, the water head was topped up and the centrifuge acceleration was set to 70g. The instrumentation data for the full scale test conducted at 70g is illustrated by Figure 39 and the measured pore pressures for specific time intervals are presented in Table 25 below. The single step increase in the pore pressures measured by all the PPTs, represents the addition of water to the top of the sample while the water head was being topped up. As demonstrated by Figure 39 and Table 25, the pore pressure behaviour of the 70g test shares some similarities to that of the 35g test. However, there are some distinct differences. Most notably, PPT 1 did not measure the highest maximum or initial pore pressures. The pore pressure reached a maximum of 250.4 kPa (Table 25) before decreasing to the lowest initial pressure as the sample consolidated. PPT 2 initially increased while the centrifuge was accelerating up to 70g and measured the largest maximum pore pressure (359 kPa). However, after reaching the maximum pore pressure, PPT 2 decreased dramatically as the sample consolidated and recorded the second lowest initial pore pressure. After reaching its maximum pore pressure, PPT 3 also started to dramatically decrease and appears to have behaved in a similar way as PPT 1 and 2. However, PPT 3 abruptly stopped decreasing and the pore pressures slowly increased and readjusted to an expected measurement. Thereafter, PPT 3 slowly decreased and stabilised as the pore pressures dissipated while the sample consolidated. PPTs 4, 5 and 6 all exhibited a similar behaviour to that of the 35g test. PPT4 increased to a maximum pore pressure of 328.3 kPa while the centrifuge was accelerating and then slowly decreased to an initial pore pressure of 260.4 kPa after the sample had consolidated. Similar behaviour is exhibited by PPT 5, which

5. Results

decreased from a maximum pore pressure of 289.2 kPa to an initial pressure of 266.4 kPa. PPT 6 increased to a maximum pore pressure of 250.4 kPa while the centrifuge was accelerating. The pore pressures then immediately started to decrease at a constant rate and PPT 6 appears to have been almost unaffected by the sample consolidating or the opening and closing of the valves.

As with the 35g test, the drop in pore pressure when the valves were opened appears to decrease with elevation. PPTs 1 and 6 again recorded the greatest and smallest decrease in pore pressures respectively. When steady state flow was achieved throughout the model, the pore pressure distribution was analogous to that of the 35g test. With the exception of PPT 6, the pore pressures increased successively with elevation. After the initial drop in pore pressures when the valves were opened, PPTs 5, 4 and 3 decreased at a constant rate during steady state flow. Conversely, PPTs 1 and PPT 2 initially decreased at a constant rate after flow was initiated, but then progressively increased as the test proceeded. At the end of the test, the pore pressure of both PPTs 1 and 2 had increased to a value greater than the pore pressures measured after the initial drop when the valves were opened. PPT 6 was seemingly unaffected by the opening of the valves and the pore pressure appears to have decreased at a constant rate after the centrifuge had accelerated to 70g. As demonstrated by Table 25, a decrease of only 0.6 kPa was measured for PPT 6 after flow was initiated. As with the 35g test, the pore pressures of PPT 3, 4, 5 and 6 seem to all fall within a range of 25.1 kPa during steady state flow. Also, in addition to PPT 1, PPT 2 now also falls further outside the range.

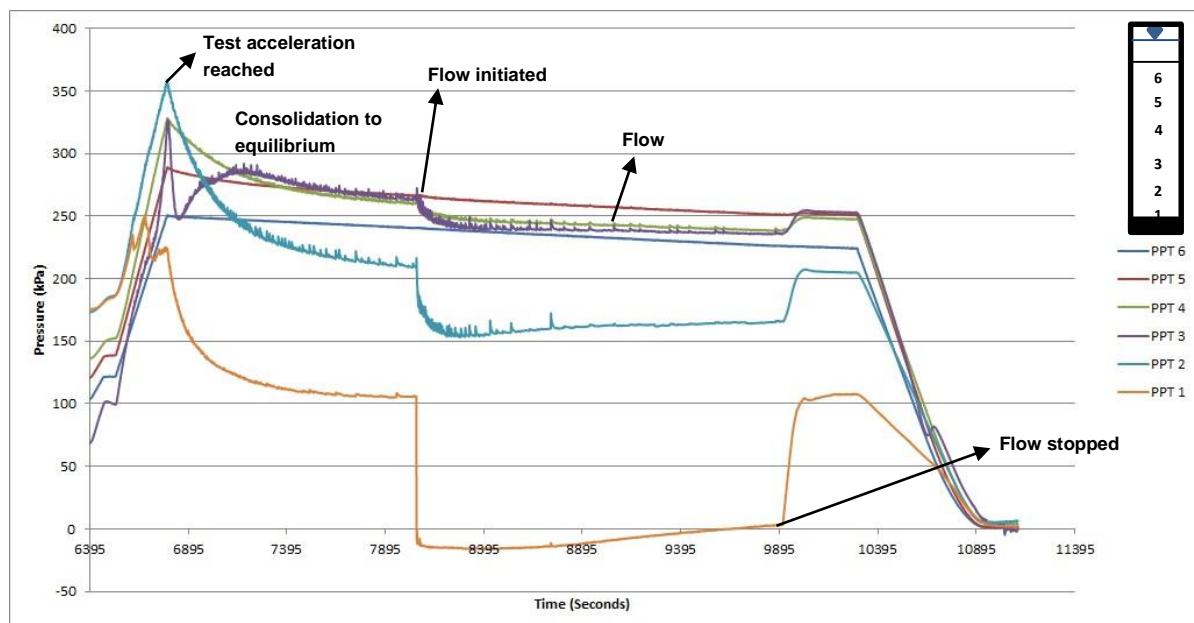


Figure 39: Recorded pore pressure data for the full scale test at 70g, with the PPT positions illustrated by the diagram in the top right corner.

5. Results

Table 25: Measured pore pressures for the full scale test at 70g.

PPT	Elevation (m)	Max pressure (kPa)	Initial pressure before flow initiation (kPa)	Pressure drop after flow initiation (kPa)	Restabilised pressure after cessation of flow (kPa)
1	0.08	250.4	105.9	120	107.3
2	0.165	359	209.3	55	204.5
3	0.26	326.8	263.6	21.5	252.7
4	0.325	328.3	260.4	10.1	247.7
5	0.44	289.22	266.4	0.8	251.3
6	0.506	250.4	240.4	0.6	224.3

Once the valves were closed at the end of the test, the pore pressures were allowed to restabilise again. After restabilising, the pore pressures returned to a distribution similar to the distribution before the valves were opened. As presented in Table 25, PPT 3 and 5 now recorded the greatest pore pressures and PPT 1 again measured the smallest pore pressure. PPT 1 restabilised to a pore pressure greater than the measured initial pressure before the permeability test. After the pore pressure had stabilised, the centrifuge was stopped and the pore pressures were allowed to equilibrate before the test was completed.

5.3.3.3 Physical observations

The physical observations recorded for the full scale test are presented in Table 26 below. As expected the flow rate in the 35g test was slower than the 70g test, taking 2440 seconds for the head to fall by 40 mm. The 70g test was slightly faster, taking 1861 seconds for the head to fall by 30 mm. After the 70g test was completed, the sample height and thickness of each horizon were measured and are presented in Figure 40 below. The sample height had decreased by 0.139 m due to consolidation settlement of the backfill material during the tests. The upper topsoil horizon was almost unaffected by consolidation and its thickness only decreased by a mere 4 mm. Conversely, the middle "softs" horizon experienced the greatest amount of consolidation with its thickness decreasing by 79 mm. The bottom carbonaceous horizon also consolidated significantly, with its thickness decreasing by 56 mm.

Table 26: The recorded physical observations for the full scale test at 35g and 70g.

Test	h_1 (m)	h_2 (m)	Test time (sec)	Initial sample thickness (m)	Final sample thickness (m)
Full scale 35g	0.87	0.83	2440	0.605	0.535
Full scale 70g	0.87	0.84	1861	0.535	0.466

As with the correlation test, the PPTs moved with the sample as it consolidated/settled. The final position of each PPT was determined in the same manner as the correlation test and their respective positions in the sample are illustrated in Figure 40 below. To calculate the permeability for the 35g test, the spacing (l) between each PPT is needed. As the model was not deconstructed or the test stopped, the final sample thickness and positions of the PPTs after the 35g test had to be estimated. In order to make this estimation, it was assumed that

5. Results

after the 35g test only half of the total PPT movement had taken place. Hence by subtracting half of the total measured movement from the final positions of each PPT at the end of the 70g test, the positions of each PPT after the 35g test were estimated. Based on these estimated positions, the final sample thickness after the 35g test could also be estimated.

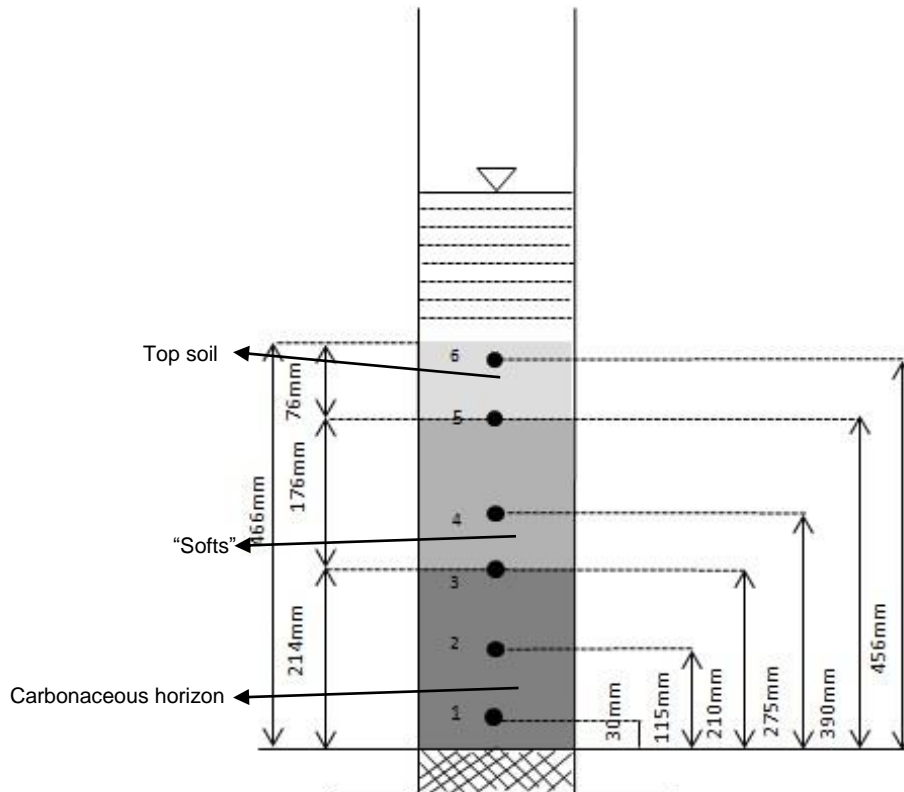


Figure 40: Configuration of the full scale test after the completion of both the 35g and 70g tests.

Along with the observations recorded in Table 26, other characteristics were also noted before, during and after the test. After the sample was packed and prepared for testing, it was noted that the sample material was finely stratified in layers of alternating coarse and fine grained material (Figure 41). The layering was most visible in the top soil horizon, due to the colouration of the material. However, both the "softs" and carbonaceous horizons also exhibited this alternating sequence of fine and coarse grained layers throughout their length.

During the 35g test, as the material started to consolidate, the water above the sample was suddenly clouded by dark fine grained particles. The cloud of particles seemed to have been forcefully ejected from the sample below the water head in a single burst and settled shortly after being ejected. Upon settling the water cleared and no further dust clouds were observed for the remainder of the tests. When observing the model for the first time after the tests, it was noted that the bottom of the strong box was covered with fine particles that had been ejected through the valves during the tests. As illustrated by Figure 42, most of the particles were dark grey and black in colour.

5. Results



Figure 41: Stratification of fine and coarse grained material observed in the top soil horizon.



Figure 42: Particles observed on the bottom of the strongbox after completion of the full scale test.

Other notable features are illustrated by Figure 43 a-d. In Figure 43a, a layer of dark grey very fine grained material can be seen covering the surface of the sample. The layer was approximately 2 mm thick and covered the entire surface of the sample. As illustrated in Figure 43 b-d, a mound of material with a crater-like appearance had formed against the cylinder at a single point above the sample. The top of the crater is also covered with approximately 1 mm of the very fine dark grey material. Thereafter, the material coarsens slightly and a

5. Results

yellowish colouration dominates. The mound has a similar appearance to a volcano, with a surface crater and a feeder pipe below the crater. The feeder pipe of the mound seems to be composed of material originating from the "softs" horizon, and may provide an explanation for the dust cloud observed at the start of the 35g test. This is confirmed by the plume of carbonaceous material that appears to have been forced up along the side of the cylinder, from the carbonaceous horizon and into the "softs" horizon (Figure 44).

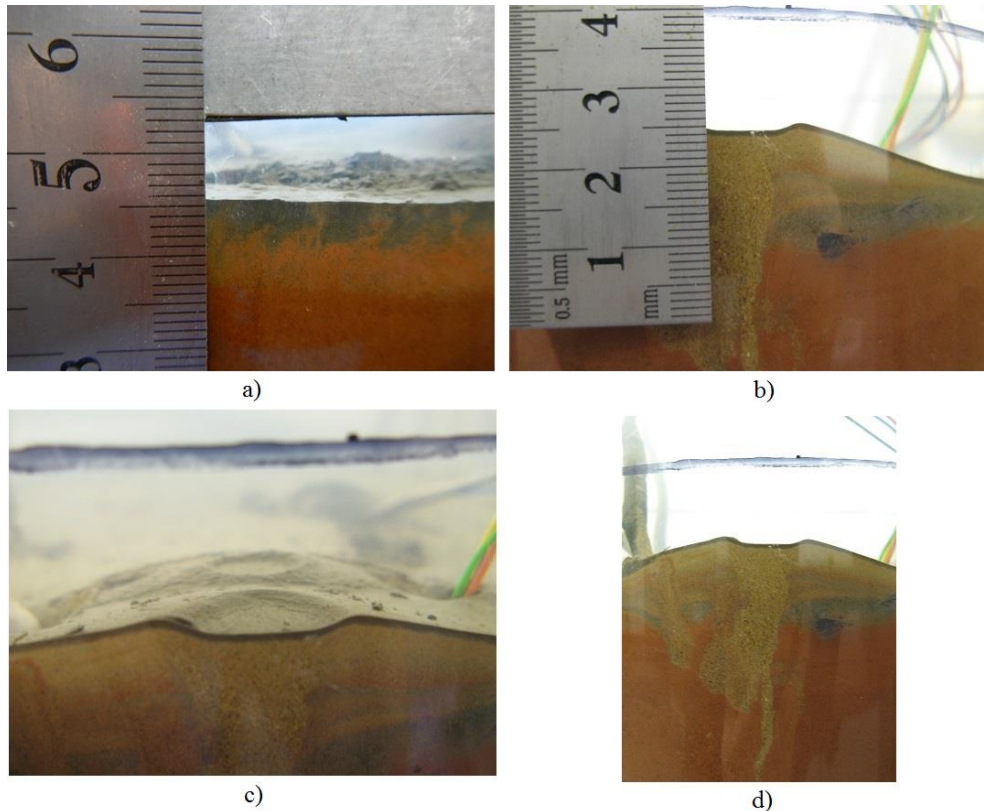


Figure 43: a) Fine grained layer of dark grey material covering the top of the sample, b) cross-section view of the mound that formed against the side of the cylinder, with grain sizes coarsening from the top down and laterally towards the centre of the mound, c) top view demonstrating the crater-like appearance of the mound, d) the "feeder pipe" of the mound extending into the top soil horizon.

Another feature depicted in Figure 45a and b, were approximately 1 mm wide cracks that were observed along the interface between the top soil and "softs" horizons. Longer, more continuous cracks were prevalent directly along the layer interface and smaller non-continuous cracks were observed directly above the interface in the top soil horizon. Both set of cracks display a jagged/wavy profile and have a broken appearance. While disassembling the model, a distinct difference in moisture content and consistency was noted between the top layer (first 10 mm) and the rest of the sample material. The upper 10mm of the sample was very wet and had a loose, sludge like appearance. The texture was also predominantly fine grained, with very little coarse material. Conversely, the rest of the sample material appeared to be dense and well compacted and was difficult to remove from the cylinder. The rest of the sample, in particular the "softs" and carbonaceous horizons, had a lower moisture content than the top of the sample.

5. Results

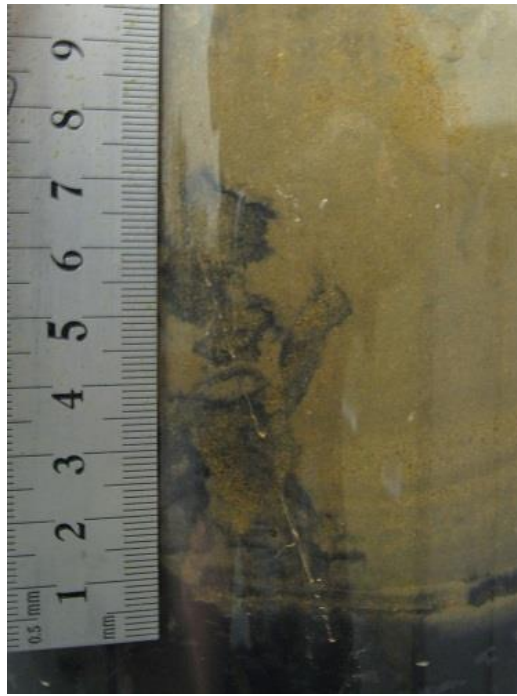


Figure 44: Plume of carbonaceous material that had been forced up into the "softs" horizon.

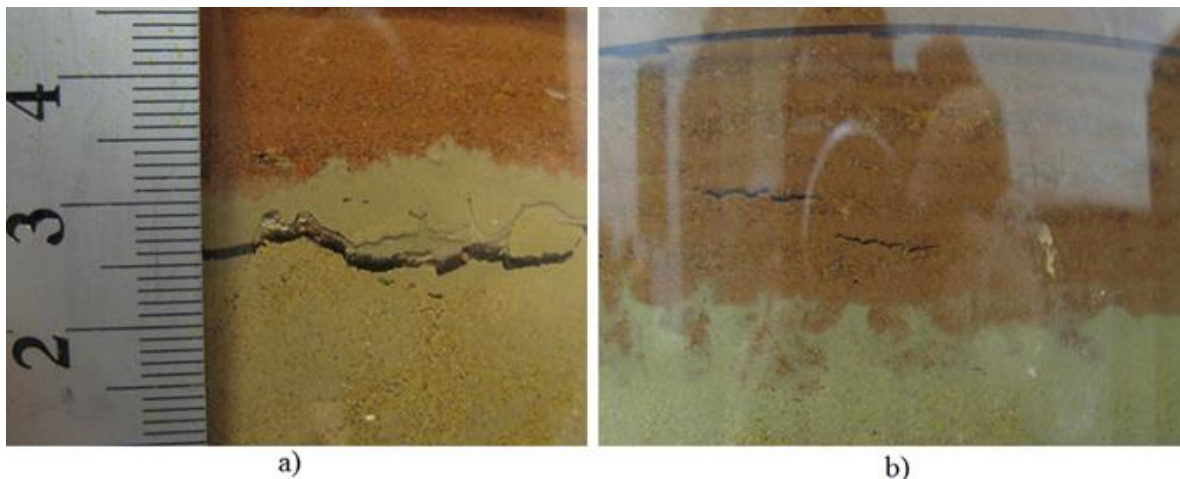


Figure 45: Cracks observed along the interface between the "softs" and top soil horizons.

5.3.3.4 ΔH calculation: 35g test

Pore pressure values were extracted from Figure 38 and used to calculate ΔH between each PPT for the 35g test. The results are presented in Table 27 below. Due to the anomalous behaviour of PPT 3 before the valves were opened, both h_{pz} and h_{ps} needed to be calculated. Using the calculated elevation heads and respective elevations of all the other PPTs, Figure 46 was plotted. By substituting the elevation of PPT 3 into the trend line formula of the graph, the elevation head (h_{pz}) for PPT 3 was calculated. Using a simple arithmetic manipulation of Equation 1 the calculated elevation head was used to determine the h_{ps} for PPT 3. Hence, the

5. Results

calculated h_{ps} and h_{pz} represent the values expected to be measured by PPT 3, should it not have behaved anomalously.

Table 27: The calculated change in total head between each PPT for the full scale test at 35g

PPT	Elevation (m)	Hydrostatic conditions			Steady state flow established			ΔH (kPa)
		h_{ps} (kPa)	H (kPa)	h_{pz} (kPa)	h_{pf} (kPa)	H_f (kPa)	h_{pz} (kPa)	
6	0.523	110.2	228.9	118.8	103.5	222.3	118.8	234.4
5	0.4565	128.5	228.9	100.4	117.8	218.2	100.4	4.051
4	0.3405	148.9	228.9	79.96	112.9	192.9	79.967	25.30
3	0.24	177.3	228.9	51.64	111.4	163.1	51.64	29.83
2	0.1275	202.4	228.9	26.56	99.45	126.0	26.56	37.08
1	0.035	228.9	228.9	0	-12.14	-12.14	0	138.2

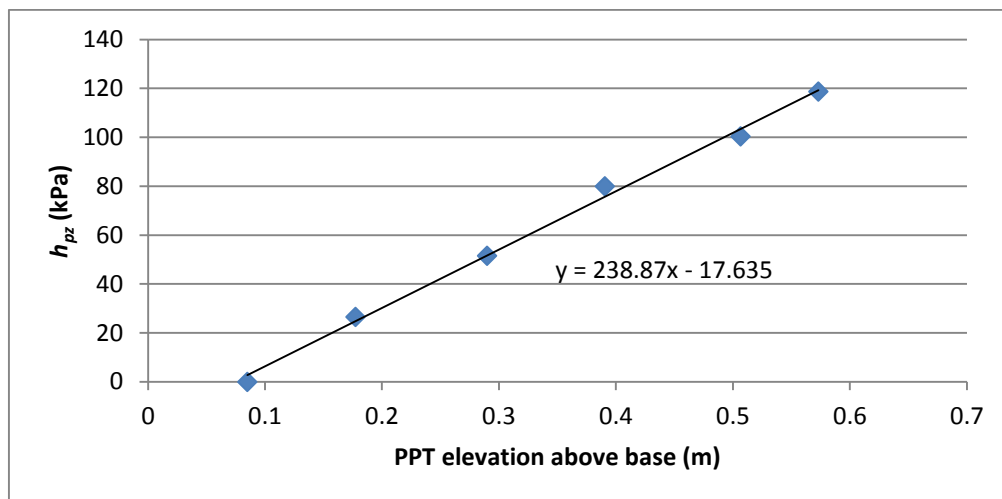


Figure 46: Plot of calculated h_{pz} and PPT elevation used to determine the h_{pz} of PPT 3.

As presented in Table 27, the difference in total head (ΔH) decreases with elevation. The smallest ΔH was calculated for the topsoil horizon between PPT 5 and 6 and the largest ΔH was calculated for the bottom portion of the carbonaceous horizon between PPT1 and 2. The upper (PPT 4 to 5) and lower (PPT 3 to 4) portions of the "softs" horizon have a similar ΔH . Similarly the ΔH of the upper portion (PPT 2 to 3) of the carbonaceous horizon does not differ significantly from that of the "softs" horizon. In contrast, the difference in total head of the lower (PPT 1 to 2) portion of the carbonaceous horizon differs significantly to the rest of the sample.

5.3.3.5 ΔH calculation: 70g test

Presented in Table 28 below are the calculated differences in total head (ΔH) between each PPT for the 70g test. Due to anomalous behaviour of PPTs 1 and 2, the hydrostatic pore pressure distributions were inaccurate and could not be used to determine the elevation heads of each PPT before the valves were opened. However, the final elevations of the PPTs at the end of the test are known and the steady state pore pressure distribution is considered to be reliable. Therefore, as with the 1g control test, the pore pressures measured during steady

5. Results

state flow can be converted from kPa to meters through division by the unit weight of water (9.81 kN/m^3). However, unlike the 1g test, the model was exposed to an elevated acceleration in the centrifuge and the elevation head needed to be calculated by multiplying the elevation by the average centrifugal acceleration (56g). With the units now all in metres ΔH between each PPT could be calculated.

Table 28: The calculated change in total head between each PPT for the full scale test at 70g

PPT	Elevation (m)	Steady state flow established				
		h_{pf} (kPa)	h_{pf} (m)	H_f (m)	h_{pz} (m)	ΔH (m)
6	0.456	227.0	23.14	48.68	25.54	46.77
5	0.39	251.9	25.67	47.51	21.84	1.166
4	0.275	238.9	24.35	39.75	15.40	7.763
3	0.21	236.3	24.09	35.85	11.76	3.906
2	0.115	164.9	16.81	23.25	6.440	12.59
1	0.03	2.257	0.2301	1.910	1.680	21.34

As with the 35g test, the maximum and minimum ΔH were again calculated for the lower portion of the carbonaceous horizon and the topsoil horizon respectively. As presented in Table 28, the ΔH decreases successively with elevation until the upper portion of the "softs" horizon. At this point there was a slight increase in ΔH before it decreased at the topsoil horizon again. In general, the calculated ΔH for the 70g test are distributed in a very similar way to that of the 35g test. The top soil and "softs" horizons do not differ by much and although slightly larger, the lower portion of the carbonaceous horizon is also similar to the overlying horizons. Additionally, the ΔH calculated for the lower portion of the carbonaceous horizon once again differs significantly from the rest of the sample.

5.3.2.6 Model permeability

Using the differences in total head between each PPT (Tables 27 and 28) and the volumetric discharge for each test, the permeability between each PPT was calculated. The results for both the 35g and 70g tests are presented in Table 29 below. As the results of the 70g test were all converted to metres, there was no need to use Equation 26. Instead, Darcy's law (Equation 3) was rearranged to solve for K and the values were then substituted into the formula. The configurations of the PPTs allowed for the comparison of both the intra and inter horizon permeability. For both the 35g and the 70g tests the permeability increases from the bottom of the sample to the top (with elevation). For the 35g test the permeability of both the upper portions in the carbonaceous and "softs" horizons, is greater than the lower portions. For the 70g test, the upper portion of the carbonaceous horizon is still greater than the lower portion. However, the upper portion of the "softs" horizon is now slightly less permeable than the lower portion. For both of the tests, the lower portion of the carbonaceous horizon had the lowest permeability and the top soil horizon had the highest permeability. The difference in permeability between the top and the bottom of the sample is more than an order of magnitude in both the 35g and 70g tests. In the middle of the layer sequence, the permeability of the "softs" horizon is slightly less than the top soil, but greater than the underlying carbonaceous horizon.



5. Results

Table 29: Calculated permeability between each PPT for the 35g and 70g tests using the pore pressure data from the PPTs.

Test	PPT	<i>l</i> (m)	<i>Q</i> (m ³ /s)	<i>A</i> (m ²)	γ_w (kN/m ³)	ΔH (kPa)	<i>K</i> (m/s)
Full scale profile 35g	1 to 2	0.0925	2.524E-07	0.0154	9.81	138.2	1.077E-07
	2 to 3	0.1125				37.08	4.878E-07
	1 to 3	0.205				175.2	1.881E-07
	3 to 4	0.1005				29.83	5.417E-07
	4 to 5	0.116				25.30	7.371E-07
	3 to 5	0.2165				55.13	6.314E-07
	5 to 6	0.0665				4.051	2.640E-06
	PPT	<i>l</i> (m)	<i>Q</i> (m³/s)	<i>A</i> (m²)	<i>i</i>	ΔH (m)	<i>K</i> (m/s)
Full scale profile 70g	1 to 2	0.085	2.482E-07	0.0154	251.1	21.34	6.419E-08
	2 to 3	0.095			132.5	12.59	1.216E-07
	1 to 3	0.18			188.5	33.94	8.549E-08
	3 to 4	0.065			60.09	3.906	2.682E-07
	4 to 5	0.115			67.50	7.763	2.388E-07
	3 to 5	0.18			64.83	11.67	2.486E-07
	5 to 6	0.066			17.66	1.17	9.125E-07

When comparing the 35g and 70g tests, it becomes evident that the permeability values are consistently higher for each horizon in the 35g test. As demonstrated by Table 30, the permeabilities estimated for the 35g test are on average 2.738 times greater than those of the 70g test. The most notable decreases are experienced by the upper portions of the carbonaceous and "softs" horizons respectively. In both cases the permeability is more than three times larger for the 35g test. The lower portion of the carbonaceous horizon is least affected and is only 1.677 times smaller in the 70g test.

Table 30: Comparison of the permeabilities calculated for the 35g and 70g test

PPT	K35g	K70g	K 35g/K 70g
1 to 2	1.077E-07	6.419E-08	1.677
2 to 3	4.878E-07	1.216E-07	4.012
3 to 4	5.417E-07	2.682E-07	2.020
4 to 5	7.371E-07	2.388E-07	3.087
5 to 6	2.640E-06	9.125E-07	2.893
Average	9.028E-07	3.210E-07	2.738

5.3.4. Validation of Darcy's law

The reliability of the permeabilities calculated for the centrifuge models is dictated by the assumption of Darcy's law being valid for fluid (water) flow in the centrifuge models. In order for Darcy's law to be valid viscous forces need to dominate and flow should be laminar as discussed in Section 2.1.1. To determine whether flow is predominantly laminar, Equation 5 can be used to calculate a Reynolds number for each centrifuge test. As described by Singh and Gupta (2000), for Darcy's law to be valid for fluid flow through soils (porous material), the calculated Reynolds number should not exceed unity.

Using the effective particle size of the backfill material, the cross-sectional area of the backfill sample and the measured volumetric discharge, a Reynolds number can be calculated for each centrifuge test conducted. Selecting an effective particle size for each individual test becomes a complicated task, as each of the backfill materials used will have different effective particle sizes. However, it has been mentioned (Section 2.2.3) that the overall permeability will be controlled by the finer fraction of material within the backfill. Consequently, the finer portion of particles in a sample are likely to have a greater overall effect on the nature of flow through the sample. Therefore, the effective particle size for all the centrifuge tests was taken as 0.002 mm. Considering that some of the model material had a smaller effective particle size (especially the slurry material), it was considered conservative to use 0.002 mm as an effective particle diameter for all materials used. By using the measured volumetric discharge and the cross-sectional area of the inside of the Perspex cylinder, the specific discharge could be calculated. Reynolds numbers were then calculated using the standard density and dynamic viscosity of water and are presented in Table 31 below.

Table 31: Calculated Reynolds numbers for each centrifuge test configuration.

Test	Reynolds Number
Control 23g	2.249E-03
Correlation 29g	9.968E-05
Full scale 35g	3.683E-05
Full scale 70g	3.622E-05

As demonstrated by Table 31, the Reynolds numbers calculated for each test all fall far below unity. Therefore, laminar flow prevailed during centrifugation, despite the increased flow velocities and Darcy's law has been demonstrated to be valid for all the centrifuge tests conducted.

6. Discussion

The results presented in Section 5 have been analysed and interpreted. In the following section the PSDs and the effect of the material downscaling have been discussed. The field permeabilities from the percolation tests have been interpreted and the reliability of the percolation tests are evaluated. A discussion of the theoretical pore pressure behaviour is presented and used to understand the pore pressure behaviour for each centrifuge test. Finally, the results of the three centrifuge tests are discussed and the model behaviour is interpreted.

6.1. Particle Size Distributions

As discussed in Section 4.3.4, the model material was prepared by downscaling the site material. To maintain the hydraulic properties of the backfill material, the model material needed to retain an adequate amount of similarity to the site material. The effect of the material preparation was interpreted through the comparison of the PSDs and particle size fractions presented in Section 5.

6.1.1. Control test material

The fine sand used in the control test had very little fines and was well sorted. Fetter (2001) and Knappette and Craig (2012) provide typical permeability values for unconsolidated sediments. According to the authors, the permeability of a well sorted very fine to medium sand should typical range between $1.00E-05$ m/s and $1.00E-03$ m/s. This provides a permeability range to compare the results of the respective centrifuge test with.

6.1.2. Correlation material

As the correlation test material was not prepared, the model and site material display almost identical PSDs despite slight differences in the relative particle size fractions. Therefore, as the site material was used in the model, it follows that the hydraulic properties of the model should be as similar as possible to those of the prototype. Provided the model material has a density in the centrifuge similar to the field density (state of consolidation) and tested under similar moisture conditions, then the behaviour of the model may be considered analogous to that of the prototype (Taylor, 1995).

6.1.3. Topsoil material

Compared to the site material, the increase in sand and silt content and reduction in gravel content in the model material can be attributed to the material preparation. As the larger gravel sized particles have been crushed and screened through a 4.75mm sieve, the model material has significantly less gravel content but more sand and silt than the site material. Despite these differences, the grading curves have a similar shape (up to the gravel fraction) and both materials have the greatest proportion of their particles within the sand fraction. Although the reduction of gravel in the model material may have slightly influenced the hydraulic characteristics of the material, this influence is considered to be negligible. As discussed in Section 2.2.3 the fine fraction of the material will control the hydraulic properties

6. Discussion

(including the permeability) of the material. Therefore, as the grading characteristics for both materials are similar for the sand, silt and clay fractions, the model material is considered to be an adequate representation of the site material in terms of hydraulic behaviour.

6.1.4. "Softs" material

As for the top soil material, the crushing of the gravel content during sample preparation can be attributed to the increase in sand and silt content in the "softs" model material. However, both the site and model materials once again retain the greatest portion of particles in the sand fraction and the grading curves have similar shapes. The same principal that was applied to the top soil can be applied to the "softs" model material. Consequently, the "softs" model material is considered to adequately represent the hydraulic characteristics of the site material.

6.1.5. Slurry

As a result of the significant differences between the grading curves and relative particles size fractions of the site and model material, the similarity between the model and the prototype hydraulic behaviour becomes questionable. Based on the material properties and position of the slurry in the backfill sequence, a degree of similarity between the model and prototype material can be reasonably claimed. The slurry was not sampled from a backfill sequence and the site material represents the slurry in its unaltered form. When placed into the backfill sequence (carbonaceous horizon in Figure 9) it will be subjected to significant amounts of overburden pressures. Most of the gravel content in the slurry is composed of soft coal fragments that are easily crushed. Therefore, the softer coal fragments forming part of the gravel fraction will be crushed and reduced to finer particle sizes. This will cause an overall reduction of the gravel fraction and general increase in the sand, silt and clay fractions, as observed in the model material. It is reasoned that the material preparation actually simulated the likely behaviour of the slurry in a backfill sequence. Although the extent of gravel content reduction in the sample preparation may be an extreme case, this cannot be confirmed due to the lack of a slurry sample from a backfill sequence. This means that the model material is considered to be the best possible representation of the hydraulic and grading characteristics of slurry material from a backfill sequence.

6.1.6. Discard material

The discard model material also displays an overall reduction in gravel content and increase in the content of the finer fractions (sand and silt). However, the gravel content has not been as drastically reduced as with the other model materials (top soil, "softs" and slurry) and the model material still retains the greatest portion of its material in the gravel fraction. This can be attributed to the harder shale fragments that make up the gravel fraction of the site discard material. When crushing the site material, the shale fragments are harder than the soft coal fragments of the slurry and are not broken up as easily. Even though the sand content of the model material increased, it still retained the largest portion of particles in the gravel fraction and similar portions in the silt and clay fractions. As with the slurry material, the discard material was not sampled from a complete backfill sequence. Instead, the site discard material was sampled from an open discard heap in an area that was at the beginning stages of backfilling. Therefore, the discard had not been subjected to any overburden pressures and subsequent

6. Discussion

crushing of larger particles. Consequently, as with the slurry, the material preparation is considered to replicate the process of crushing at the base of a backfill sequence and overall reduction in gravel content. The extent of the crushing cannot be confirmed due to the lack of a discard sample that had been subjected to typical overburden pressures in the backfill sequence. The model material is reasoned to adequately represent both the hydraulic and grading characteristics of discard material that has been placed into a backfill sequence.

6.1.7. Summary

For all of the materials used in the full scale test, there had been an overall reduction in the gravel content that is accompanied by an increase in the sand and silt content. This is to be expected as a result of the material preparation processes that were needed to downscale the site material for use in the model. Although this has resulted in a change of the material grading characteristics, it has been reasoned that due to particle crushing in an actual backfill sequence, a reduction of coarse particles and increase in fines is to be expected. As it was not possible to obtain a sample from a backfill sequence that had been in place for a period of time, the actual extent of this phenomenon cannot be positively confirmed. Hence, the material preparation is thought to replicate the actual grading characteristics of material in an actual backfill sequence as accurately as possible.

A major concern is the replication of the hydraulic properties of the site material in the centrifuge model. As explained in Section 2.2.3 the material preparation procedures were specifically aimed at including a larger portion of the material PSD by removing the coarsest material from the samples. Although there has been an increase in the sand content due to the crushing of the coarser gravel, the silt and clay contents have not changed significantly (except for the slurry). Furthermore, all the prepared material, with the exception of the slurry, retained the greatest portion of their particles in the same fraction as the site material. As the hydraulic behaviour is controlled by the fine portion of the material (Section 4.3.1) and the grading characteristics of the model material are thought to adequately represent the site material in a backfill sequence, the hydraulic characteristics of the site material were adequately simulated by the prepared model material.

6.2. Field Percolation Tests

The aim of the field percolation tests were to provide a base line field permeability values for comparison with an analogous centrifuge model of the test site. However, a number of issues with percolation tests are highlighted by Dippenaar *et al.* (2014). Firstly, complete saturation of the material below the auger hole is difficult to confirm. Furthermore, due to lateral dispersion below the auger hole, saturation is variable and will complicate the estimation of the hydraulic gradient. Therefore, the assumption of a hydraulic gradient as unity may result in an over estimation of the material permeability. Dippenaar *et al.* (2014) also state that further bias in the test results may be incurred due to the nature of the percolation test methods. As the auger holes can only be drilled in material soft enough to allow penetration, this may already imply a bias towards an area with more granular material or macropores. The auguring process is likely to loosen and disturb the surrounding material, thereby creating a more granular material at the test location. Due to these biases, the permeability estimated by the percolation tests is likely to be slightly higher than the natural in-situ values.

When interpreting the results of the percolation tests the above mentioned issues need to be taken into consideration. To arrive at a logical and representative field value for comparison with the centrifuge model, the effect of the percolation test procedures on the permeability values need to be analysed. As mentioned in Section 4.1.1, the use of the Perspex cylinder ensured more accurate measurement of the fall in head. Also the increased water pressure on the base of the hole is thought to have promoted a greater degree of saturation below the hole. Furthermore, consecutive test runs were conducted for each test and steady state flow was achieved. Although the depth of saturation below the hole cannot be confirmed, the tests reaching steady state flow intrinsically implies that at least a portion of the material below the hole was saturated. One can therefore assume that a hydraulic gradient of unity is reasonable.

Although the use of the Perspex cylinder was found to reduce the lateral seepage through the side wall of the auger hole, sealing and seating of the cylinder tightly against the bottom of the auger hole proved to be difficult. As the bottom of the auger holes were not completely smooth and flat, the cylinder may not have been tightly sealed against the bottom of the hole. This may have led to some seepage escaping through these spaces, resulting in the estimation of higher permeability values. An example of this is demonstrated by the higher permeability of test number three in Table 11. Due to an undulation in the floor of the test pit, the auger hole for test number three was drilled at a slight angle. Due to this angle, the cylinder may not have been adequately seated and sealed against the bottom of the hole and resulted in a faster fall in head as water escaped through the bottom of the cylinder. However, the higher permeability of test number three could also be explained by the presence of macropore in the auger hole. Test number three has therefore been omitted, as it is not considered to be representative of the in-situ site conditions.

As demonstrated by Table 11, the measured permeabilities for the remainder of the tests are very similar. As the tests were conducted in the same material with similar densities and the same test procedures were used for all tests, the estimated permeability values are considered to be representative of the site material at the time of testing and under the specific conditions of the test procedures. Based on the PSD the site material for the correlation test



6. Discussion

can be classified as a fine to medium grained silty sand. According to Fetter (2001) and Knappette and Craig (2012) the typical permeability of a silty sand ranges between $1.00E-08$ m/s and $1.00E-06$ m/s. Based on this observation it seems that the permeability of the site material has been slightly over estimated by the percolation tests. This can once again be attributed to the percolation test procedures. The excavation of the test pit and drilling of the auger holes undoubtedly caused some disturbance to the structural properties of the in-situ material. These procedures possibly loosened the material and resulted in the material becoming more granular and less dense than what it would be in its undisturbed state. Accordingly, when comparing the results of the percolation tests to permeability of the centrifuge model this needs to be considered when commenting on the accuracy of the centrifuge model and methodology.

6.3. Centrifuge Tests

Using the results for each centrifuge test, the following section discusses the findings of each centrifuge test. A discussion on the expected theoretical pore pressure distributions for both hydrostatic and flow conditions is presented and used to evaluate the results of the centrifuge tests. The reliability of the methodology is assessed and the hydraulic behaviour of the model is interpreted from the distributions of the measured pore pressures and total heads, the calculated permeabilities and physical observations for each test. Furthermore, the hydraulic behaviour of the prototype is inferred from the modelling results and the limitations when relating the model to the prototype are identified and discussed.

6.3.1. Theoretical pore pressure responses

To interpret the results of the centrifuge tests, the theoretical pore pressure response needs to be understood. As in Section 4.4.2, a theoretical example has been used to illustrate the expected pore pressure response for both hydrostatic and flow conditions (Figures 47 and 48). As illustrated in Figures 47 and 48, three PPTs (where the positions in the sample are represented by the numbers 1-3) have been spaced at fixed distances from one another in a homogenous sample and seepage is assumed to drain freely from the base of the model with no flow constrictions. In the example, the elevation head (h_z) of a PPT above a set datum is represented on the Y-axis and the pressure head (h_p) measured by each PPT is displayed on the X-axis. The total head ($h_z + h_p$) at each PPT for both hydrostatic and flow conditions has also been illustrated in the example. For both hydrostatic (Figure 47) and flow (Figure 48) conditions, the datum has been set at PPT 1. Consequently, the elevation head at PPT 1 will always be set to zero, increasing towards the top of the sample (PPT3) as illustrated by Figures 47 and 48 respectively.

Under hydrostatic conditions (before flow is initiated), the pressure head should theoretically increase linearly with depth below the water surface, due to the pressure exerted by the overlying water column (Figure 47). Consequently, PPT 1 and 3 should measure the highest and lowest pore pressures respectively. As there is no flow through the sample, the hydrostatic potential (or total head) should, in theory, be constant throughout the cylinder. Therefore, the total head will be equal to the maximum pore pressure measured in the sample (i.e. the pore pressure at PPT 1), irrespective of the individual PPT elevation. The hydrostatic total head (H_s), as demonstrated by Figure 47, will then plot as a straight vertical line with an X-intercept equal to the pore pressure measured at PPT1.

When the valves at the bottom of the cylinder are opened, water is immediately removed from the bottom of the sample and pore pressures are prevented from accumulating. As illustrated by Figure 48, the pressure head at PPT 1 should theoretically equalise with the pressure on the outside on the cylinder (roughly atmospheric) and decrease to zero. At the top of the sample (PPT 3), higher pore pressures should be maintained due to the pressure exerted by the water column directly above the sample. As a result, the pore pressures will decrease with depth while the outlet valves are open and steady state flow is established (Figure 48). Therefore, during steady state flow, both the elevation head and pressure head decrease with depth and it follows that the total head should theoretically decrease from the top to the bottom of the sample, as illustrated by Figure 48. Accordingly, Bernoulli's law

6. Discussion

(Section 2.2.1) is satisfied as flow will occur from high total head (potential) (at the top of the sample) towards a lower total head (potential) (bottom the bottom of the sample).

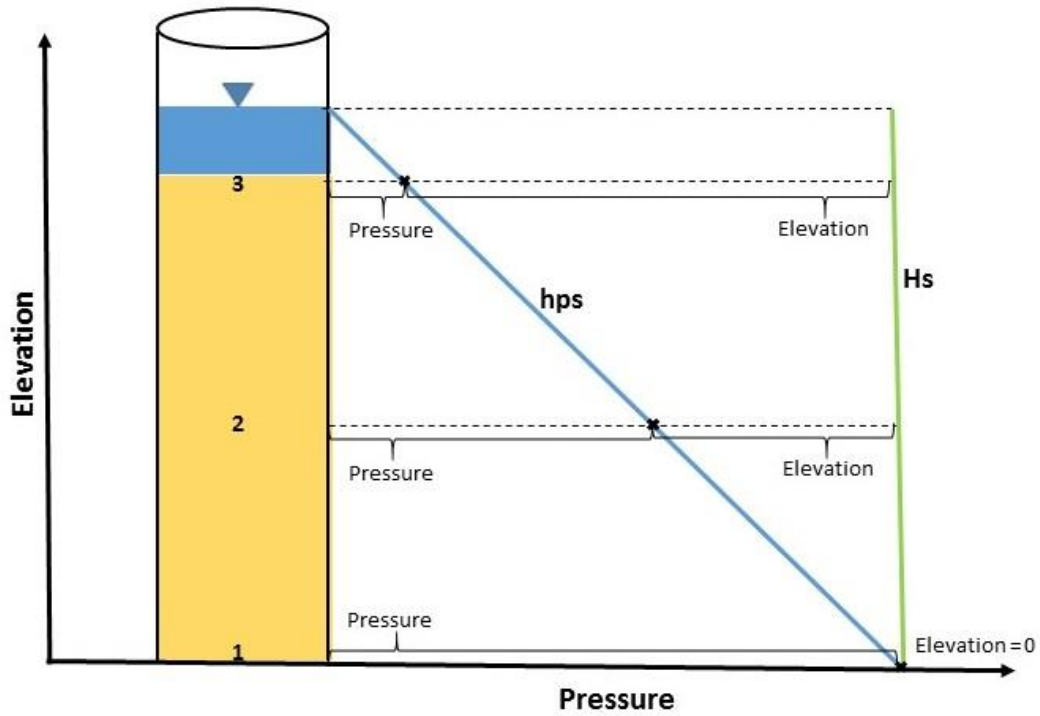


Figure 47: Theoretical pore pressure distribution under hydrostatic conditions, illustrating both the hydrostatic pressure (h_{ps}) and total head (potential) (H_s) distributions.

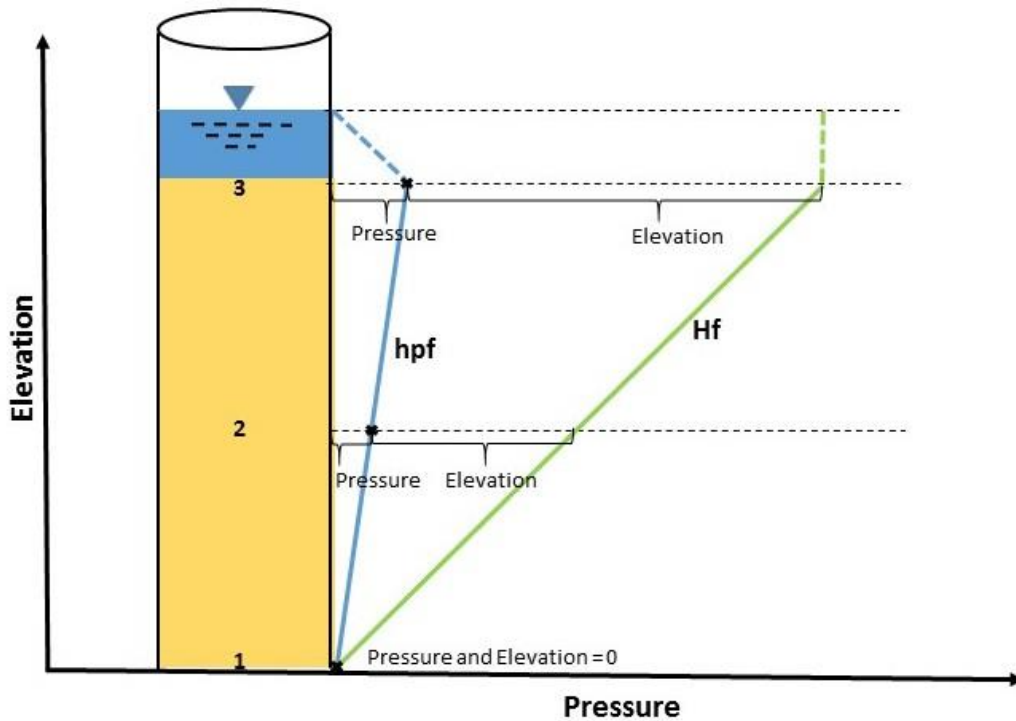


Figure 48: Theoretical pore pressure behaviour under steady state flow conditions, illustrating both the pressure (h_{pf}) and total heads (H_f) once steady state has been achieved after opening the outlet valves.

In summary, under hydrostatic conditions, the pressure head (h_{ps}) should increase with depth while the total head (H_s) remains constant throughout the sample. Conversely, for flow to occur from the top to the bottom of the sample, both the pressure head (h_{pf}) and total head (H_f) should decrease with depth. Also, assuming that the sample is incompressible and that the PPTs remain in a fixed position for the duration of the test, h_z will remain constant for each PPT under both hydrostatic and flow conditions. Therefore, any changes in total head are a direct result of the measured pore pressures which is a function of the material permeability.

6.3.2. Control test

The purpose of the control test was to validate and fine tune the test methodology by controlling as many variables as possible. Additionally, by conducting the test at regular gravitational acceleration (1g), the control test provided the opportunity to verify the scaling law for the modelling of permeability in a centrifuge. The following section provides an interpretation of the pore pressure data and model permeability and assesses the scaling law for permeability in the centrifuge.

6.3.1.1 Interpretation of pore pressure data

When analysing the pore pressure data of both the 23g and 1g tests it becomes apparent that the pore pressures display a similar distribution in both tests. The pore pressures stabilised almost instantly after the centrifuge reached 23g and the graphs of each PPT plot as parallel lines (Figure 34) before the valves were opened. Although the hydrostatic pressure distribution of both the 1g and 23g tests are similar, the plots of the 1g test are not as smooth as the 23g test and have a jagged appearance. Due to the lack of centrifugal force to drive the water through the sample, the pore pressures are much lower than the 23g test. Therefore, the PPTs are measuring pore pressures at the limit of their sensitivity and the slightest variation in pore pressure becomes noticeable on the plots. Hence, the spikes are a function of the measurement scale and instrument resolution and not as a result of highly variable pore pressures. In terms of response to the valves being opened, all three PPTs react rapidly in both tests and the pore pressures drop sharply. This may indicate that the sample is hydraulically well connected as the bottom and top of the sample respond in similar times. As the sample was composed of a fine sand, this connectivity is likely related to a higher sample permeability.

To visualise and compare the pore pressure distributions for both tests, the pore pressure (pressure head) (Figures 49a and 50a) and total head (Figures 49b and 50b) distributions have been plotted for hydrostatic and steady state flow conditions. The theoretical hydrostatic pressure heads were calculated using Equation 28, using the depth of each PPT below the water surface. These values were then plotted according to the respective PPT elevations (Figures 49a and 50a) and used to assess the accuracy of the measured hydrostatic pore pressures. As illustrated by Figures 49a and 50a the h_{ps} increases with depth and correlates well to the expected theoretical distributions. The H_s (Figures 49b and 50b) is also constant throughout the column for both the 23g and 1g tests. Therefore, the hydrostatic pore pressure responses are in line with the expected theoretical response and the measured pore pressures for both the 23g and 1g tests are considered to be accurate.

6. Discussion

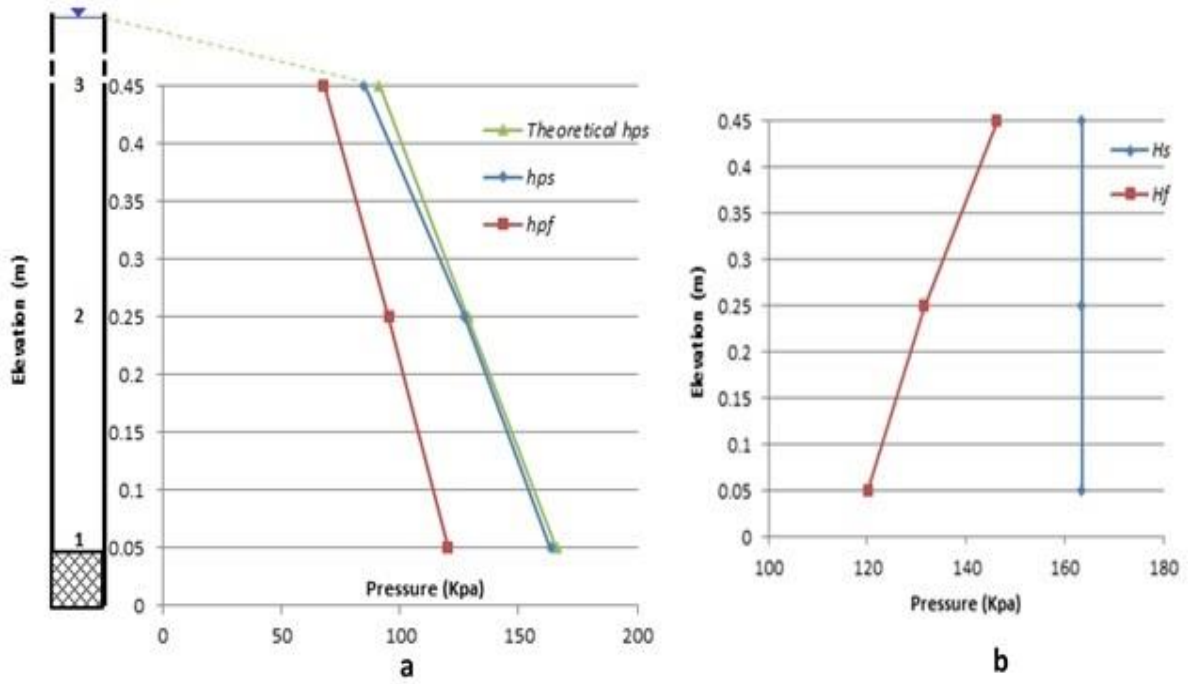


Figure 49: a) Distribution of the calculated theoretical h_{ps} , measured h_{ps} and h_{pf} and b) distribution of H_s and H_f at 23g.

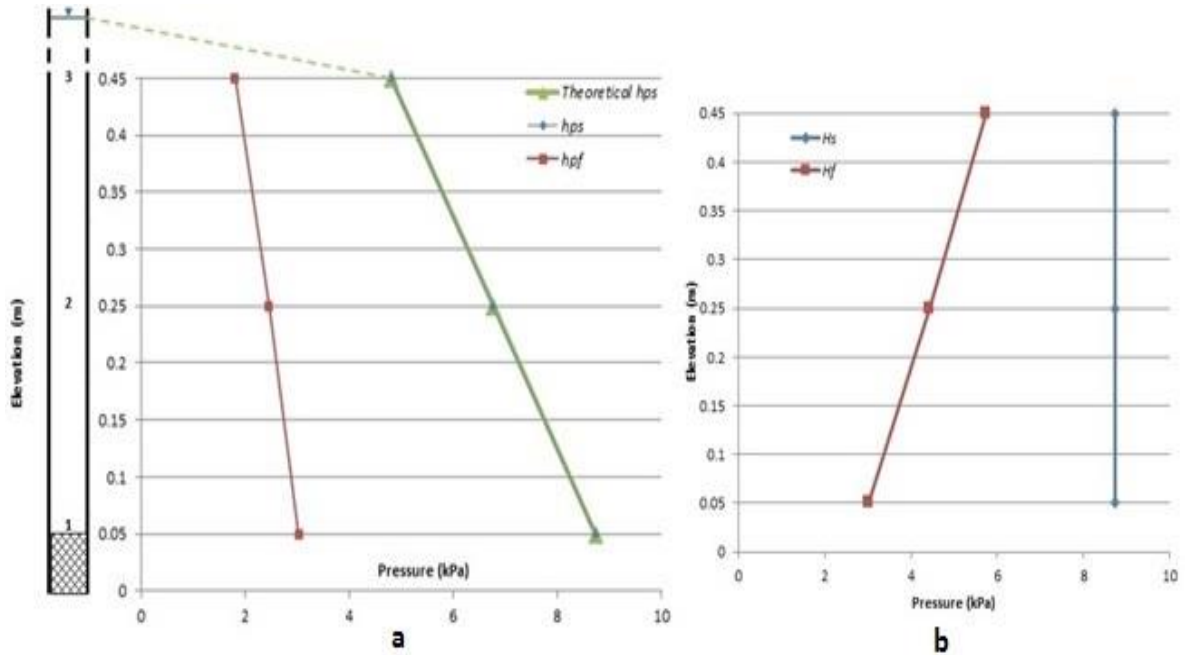


Figure 50: a) Distribution of the calculated theoretical h_{ps} , measured h_{ps} and h_{pf} and b) distribution of H_s and H_f at 1g.

However, for both the 23g and 1g tests h_{pf} increases with depth once flow was initiated (Figures 49a and 50a). The maximum and minimum values are still measured at the bottom (PPT1) and at an elevation of 0.40 m (PPT 3) respectively. As highlighted in Section 6.3.1, h_{pf} should decrease with depth and the measured response does not correlate to the expected theoretical response. If the sample was freely drained, the pore pressure at the bottom of the cylinder (closest to the outlet valves) should theoretically decrease to atmospheric pressure when the valves are opened. As demonstrated, this is not the case for the control tests.

6. Discussion

Due to the higher permeability of the sand used in the control test, the water could not flow fast enough through the outlet valves. This resulted in the valves posing as a flow constriction and caused a subsequent accumulation of pore pressures throughout the length of the sample. Therefore, it can be inferred that the tests were not freely draining and cannot be considered true falling head tests. Despite the constriction posed by the outlet valves, H_f for both the 23g and 1g tests decreases with depth (Figures 49b and 50b) and correlates to the expected theoretical response (Figure 48). Therefore, Bernoulli's law is satisfied and downward flow was maintained through the column.

6.3.1.2 Model permeability and scaling in the centrifuge

As highlighted in Section 6.1.1, the permeability of the control sand should typically range between 1.00E-05 m/s and 1.00E-03 m/s (Fetter, 2001 and Knappette and Craig, 2012). The calculated permeability for both the 23g and 1g tests falls well within this range. However, Equation 17 was specifically developed for falling head tests with low permeability samples where there are no flow constrictions. Therefore, Equation 17 cannot be applied to estimate the permeability of the control test. Hence, in this instance the two methodologies cannot be meaningfully compared. However, as the permeability calculated using the pore pressures is well within the acceptable range for a fine sand, the methodology appears to be promising and provides an accurate estimate of the sample permeability.

The discussion in Section 2.3.4 highlighted that flow in a centrifugal field was governed by the scaling law for seepage velocity (Equation 10). As mentioned by Thusyanthan and Madabhushi (2003) this scaling law can be satisfied by scaling either the permeability (K) or the hydraulic gradient (i) and has led to much controversy in the modelling of fluid flow in the centrifuge (see Section 2.3.4). The control test provided the opportunity to explore and understand these two opposing views. When comparing the time taken for the head to fall by 0.24m in each test, it is apparent that the 23g test took significantly less time than the 1g test. As expected the fluid velocity was substantially increased in the centrifuge and one would expect to calculate a higher permeability for the 23g test than the 1g test. However, as demonstrated by Table 16, the permeabilities calculated using the measured pore pressures at 1g and 23g only differ by the slightest of margins. The permeability of 23g test is on average only 1.233 times slower than the permeability of the 1g test. Therefore, the permeability appears to have been almost unaffected in the centrifuge and is not N times greater but only decreased slightly when exposed to an applied centrifugal force.

These findings contradict those of Singh and Gupta (2002) and can be explained by the authors not considering the increase in pressure head and only using the elevation head in their calculation of the permeability (Robinson, 2002). The hydrostatic pore pressures of the 23g and 1g test are compared in Table 32 below. As demonstrated, when h_{ps} at 23g is divided by the average centrifugal acceleration through the sample (N_r), the pressures are almost identical to the h_{ps} at 1g. Therefore, as proposed by Robinson (2002) water pressures in the centrifuge are increased N times at all points in the sample.

Table 32: Comparison of the measured hydrostatic pore pressures at 1g and 23g

PPT	Elevation (m)	h_{ps1g} (kPa)	h_{ps23g} (kPa)	$h_{ps 23g/N_r}$ (kPa)
1	0	8.732	163.4	8.600
2	0.2	6.485	127.1	6.689
3	0.4	4.804	85	4.474

The increase in pressure head can be accounted for in Equation 17 through substitution of the average centrifugal acceleration as illustrated by Equation 34 below (Robinson, 2002).

$$K_{cen} = \frac{L}{Nt} \ln \left(\frac{h_1}{h_2} \right) \quad (34)$$

Singh and Gupta (2002) argue that both the lengths of the soil and water columns are increased N times in the centrifuge. Therefore, the water column length over which the change in head must occur in the model is equal to that of the prototype and the hydraulic gradient is not increased in the centrifuge. The principles of centrifuge modelling are in opposition to this view. By accelerating the model to Ng in a centrifuge, linear dimensions are not physically increased to prototype proportions. The applied centrifugal acceleration creates a stress distribution in a model analogous to a prototype N times larger than the model (provided the prototype material is used in the model). Therefore, the lengths of the water and soil columns are not increased N times in the centrifuge but the stresses (pressures) are increased to a prototype scale. The results of the current investigation support this line of reasoning. By measuring the pore pressures throughout the model at both 1g and 23g it was demonstrated that the pore pressures are increased N times in the centrifuge. At Ng in the centrifuge, the induced prototype pressures need to change over a flow path length that has been condensed N times in the model. Therefore, it can be confirmed that the hydraulic gradient is modelled N times in the centrifuge and not the permeability. As mentioned by Robinson (2002), this proves that permeability is a material parameter that is unaltered in the centrifuge, assuming that the material does not compress.

As a result, the pore pressures measured by the PPTs during centrifugation represent the prototype pore pressures. The permeability calculated using the pore pressures during centrifugation can therefore represent the prototype permeability and do not need to be scaled N times. However, the permeability calculated for the 23g test was slightly less than the 1g test. This can be attributed to a slight densification of the sample in the centrifuge. The applied centrifugal acceleration causes the soil particles to be forced together and results in a slightly lower permeability in the centrifuge. The measured difference is insignificant in terms of seepage and can be considered to accurately represent the prototype. Furthermore, the calculated permeabilities of the 23g test all fall within the expected range for a fine sand and the test time was substantially reduced. Therefore, the centrifuge methodology is considered to be both accurate and efficient at measuring the permeability of a sample. Provided that Darcy's law is valid and the increase in pressure head is taken into consideration, the centrifuge provides a rapid means of estimating the permeability.

6.3.3. Correlation test

With the methodology proven and the applicable scaling laws now understood after the control tests, the ability of the model and methodology to replicate specific prototype conditions needed to be established. In order to do so, the correlation test was used to reproduce the conditions of a field site material with a measured permeability. The interpretation of the test pore pressure data and the comparison between the calculated model permeability and field permeability is presented below.

6.3.2.1 Interpretation of pore pressure data

Unlike the control test, the pore pressures of the correlation test slowly decrease after reaching their maximum values and only stabilise after a considerable amount of time. This is due to the excess pore pressures dissipating more slowly in the sample as it consolidates due to the lower permeability. The correlation test material is more poorly sorted than the control test material and has a greater fraction of fine material. Consequently, when exposed to a centrifugal acceleration the sample consolidates at a slower rate and the particles are rearranged into a denser packing. To achieve a denser packing, the pore spaces are reduced and any excess pore water that cannot be accommodated by the smaller pores needs to be expelled. Therefore, at the point where the pore pressures stabilise (h_{ps}) the sample has completely consolidated/settled. The consolidation time's decrease with elevation and pore pressures at the bottom of the sample take longer to stabilise. This is due to the sample having a lower permeability which increases the travel time for expelled pore water from the bottom to the top of the sample. Lower sample permeability can also be confirmed by the relationship between response time after the valves are opened and PPT elevation. When the valves are opened, PPTs with higher elevations take longer to respond than PPTs closer to the valves. Due to lower sample permeability it takes longer for water to flow from the top to the bottom of the sample, so that the pore pressures can re-equilibrate when flow is initiated. Subsequently, steady state flow is achieved faster at the bottom than at higher elevations in the sample. Opposed to the straight lines plotted for the control test, the curved/non-linear lines (Figure 36) of the correlation test are another indication of the time delay in pore pressure responses caused by the lower permeability of the sample.

In order to visualise the pore pressure distribution in the correlation test, the distributions of the calculated theoretical h_{ps} , the measured h_{ps} and h_{pf} and the total heads (H_s and H_f) have been plotted (Figure 51a and b). As illustrated by Figure 51a h_{ps} increased with depth and the maximum value is measured at the bottom of the sample (PPT 1) and minimum value at an elevation of 0.3 m (PPT 3). The measure and calculated h_{ps} also correlate well, with the theoretical h_{ps} being only marginally greater than the measures pressures. Additionally, H_s (Figure 51b) is equal to the pressure at PPT1 and is constant throughout the column. When the valves are opened and steady state is established, h_{pf} decreased with depth (Figure 51a). PPT 1 dropped to just below zero and the maximum pore pressure is now measured by PPT 3. Furthermore, H_f (Figure 51b) also decreases with depth and downward flow was maintained through the column. Due to the lower permeability of the correlation test material, the outlet vales did not pose any constrictions to flow. As a result, the pore pressure at the bottom of the sample equalised with atmospheric pressure. Therefore, the measured

6. Discussion

pore pressure response correlates to what was theoretically expected (Figures 47 and 49) and the measured pore pressures are considered to be accurate.

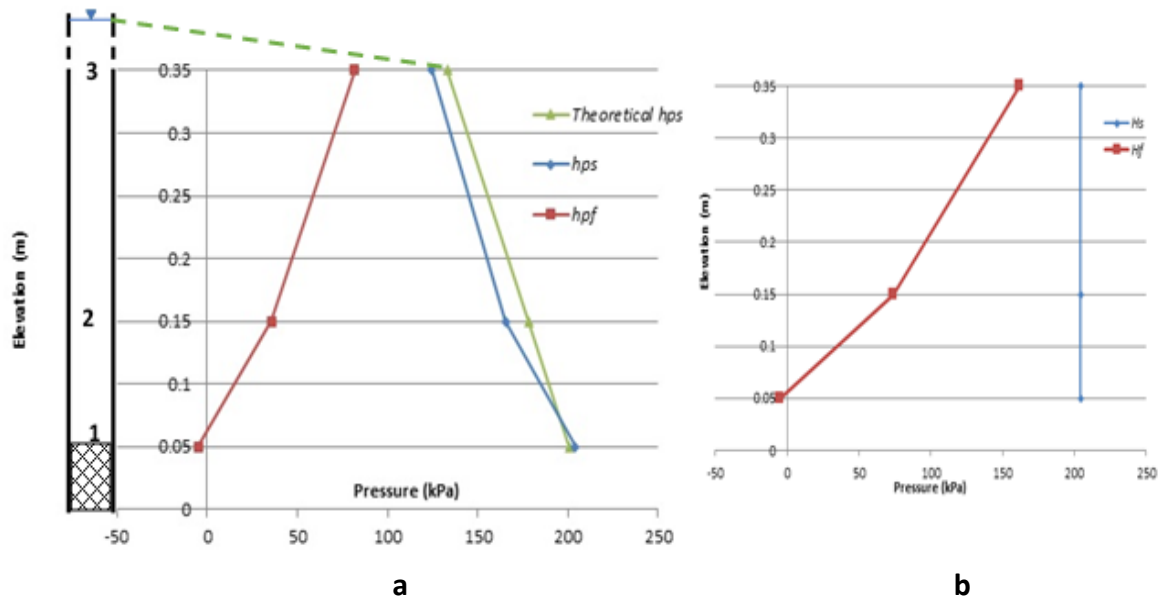


Figure 51: a) Distribution of the calculated theoretical h_{ps} , measured h_{ps} and h_{pf} and b) distribution of H_s and H_f at 29g.

6.3.2.2 Model permeability and correlation to field values

Based on the interpretation of the pore pressure data above, the permeability of the sample is expected to be significantly lower than the control test. This was confirmed when the physical test observations were analysed. The water head decreased by only 90.5 mm in 2142 seconds and suggests a slower flow velocity than the control test, despite the greater centrifuge acceleration for the correlation test. This and the grading curve of the correlation test material, all suggest a lower permeability.

Initially, the permeability calculated with the pore pressures seems to be rather low. However, when comparing the results of the centrifuge tests to the expected permeability of a silty sand (1.00E-08 m/s and 1.00E-06 m/s), it is apparent that the calculated values fall well within the acceptable range. The calculated centrifuge permeability should therefore be similar to the permeability measured with the percolation tests. However, as demonstrated by Table 23 this is not the case. The calculated average model permeability is two orders of magnitude less than the calculated field average. The centrifuge model appears to underestimate the permeability of the material and does not appear to be a reliable approximation of the prototype site. However, as mentioned in Section 6.2 the reliability of the field percolation tests need to be considered when making the comparison between the model and the prototype site.

Firstly, due to the intrinsic bias and test procedures involved with the percolation tests (Section 6.2) the accuracy of the field permeability needs to be questioned. The measured field values fall well outside the expected permeability of a silty sand and it is more than likely that the permeability has been overestimated due to test procedures and intrinsic test bias. Secondly, one needs to examine whether the field values are representative of the prototype that has been modelled in the centrifuge. At 29g the model simulates the stresses of a 13.8 m

6. Discussion

thick prototype in a completely saturated and consolidated state. Conversely, the percolation tests only measured the permeability of the uppermost portion of the "softs" horizon at an unknown state of consolidation. The measured field permeability cannot be considered to be representative of the entire "softs" horizon. Hence, the prototype modelled in the centrifuge is not adequately represented by the values measured in the field. Therefore, the permeability calculated by the centrifuge model should be related to field values calculated at similar depths (and degrees of saturation) in the prototype, where the in-situ stresses and consolidation state would be similar.

As the field permeability could only be measured for the uppermost portion of the "softs" horizon, the comparison of the model and percolation permeability does not allow the representativeness of the centrifuge model to be meaningfully interpreted. To meaningfully evaluate the reliability of the centrifuge model, more representative field permeability data is needed for comparison to the centrifuge results. However, based on the success of the control tests and the fact that the permeability of the correlation test falls within the expected range, the methodology is considered to be sound. Therefore, provided the model is an adequate representation of the prototype (and vice versa), one could confidently relate the model permeability to the respective prototype. Additionally, the model permeability and hydraulic behaviour can be related to a hypothetical prototype represented by the geometry of the centrifuge model. A fundamental understanding of the behaviour of specific hypothetical configurations can be gained from this approach.

6.3.4. Modelling full scale profile

The full scale test was designed to simulate the geometry and properties of a heterogeneous backfill prototype. The objective of accelerating the model in the centrifuge, was to measure the permeability and understand the hydraulic behaviour of the backfill under simulated prototype stresses. The following sections present the interpretation of the modelling results presented in Section 5.3.3.

6.3.3.1 Interpretation of pore pressure data

When analysing the pore pressure data of both the 35g and 70g tests it becomes apparent that the pore pressures display a similar behaviour to that of the correlation test. After attaining a maximum value after the maximum acceleration was reached, the pore pressures slowly decreased to a stable reading as excess pore pressures dissipated while the sample consolidated. As with the correlation test the consolidation time decreases with elevation while the PPT response time increases with elevation. This can be attributed to a low material permeability of the individual horizons in the sample.

The 35g and 70g tests share further similarities in their steady state pore pressure distributions but vary significantly in the distribution of the hydrostatic pore pressures for each test. To visualise and compare the pore pressure distributions for both tests, the distributions of the calculated theoretical h_{ps} , measured h_{ps} and h_{pf} (Figures 52a and 53a) and the total heads (H_s and H_f) (Figures 52b and 53b) have been plotted. As demonstrated by Figure 52a, h_{ps} increases with depth and the maximum and minimum pore pressures are measured at PPT 1 and 6 respectively. However, the h_{ps} for PPT 3 needed to be calculated due to a sudden

6. Discussion

decrease in pore pressure while the sample was consolidating as explained before. This sudden decrease in pore pressure can be explained by the loss of contact between PPT 3 and the sample due to the cable of PPT 3 being pulled tight. The coarser “softs” and top soil horizons overlying PPT 3 are likely to have consolidated quicker than the finer grained carbonaceous horizon. Consequently, these overlying horizons would have dilated slightly while the carbonaceous horizon was still consolidating. As a result, the cable of PPT 3 would have been gripped and pulled tight by the softs and top soil horizons, while PPT 3 was being pulled down as the carbonaceous horizon consolidated. When flow was initiated consolidation stopped and PPT 3 gradually recovers to an acceptable reading during steady state flow as its cable was no longer being pulled tight. By accounting for this anomalous behaviour, Figure 52a and b demonstrates that the pore pressure response correlates well to the expected theoretical behaviour (Figures 47 and 48) and the model was freely drained while downward flow was still maintained through the column.

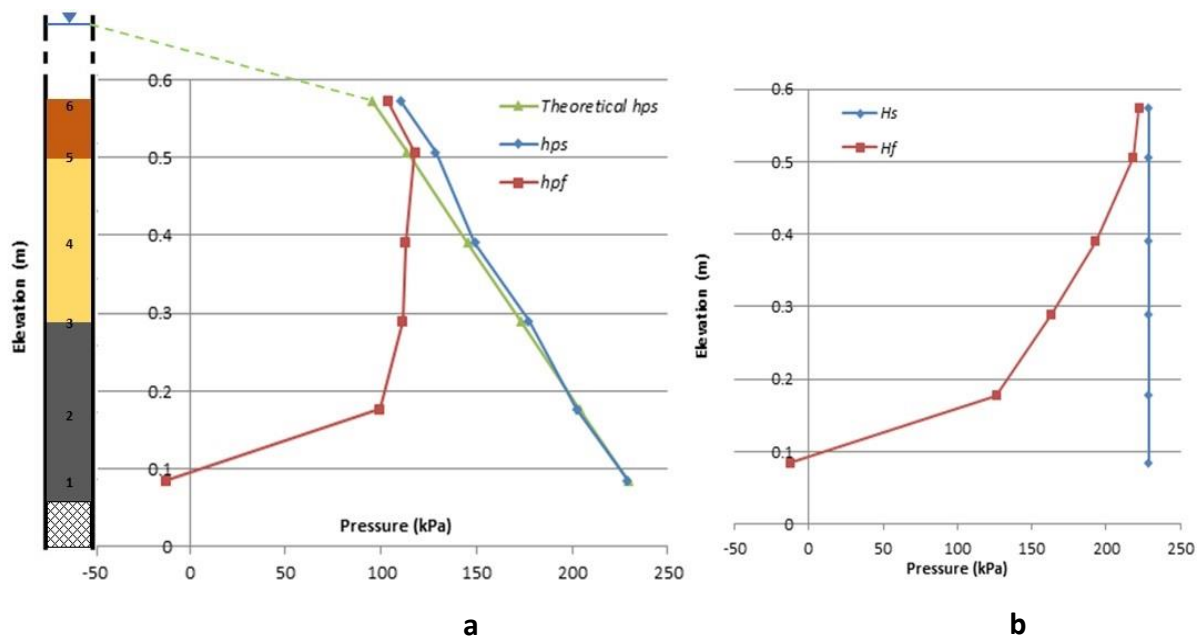


Figure 52: a) Distribution of the calculated theoretical h_{ps} , measured h_{ps} and h_{pf} and b) distribution of H_s and H_f at 35g.

The h_{ps} for the 70g test is considerably different from that of the 35g test. As illustrated by Figure 53a, PPT 1 and PPT 2 recorded the two lowest h_{ps} values and the measured hydrostatic pore pressure response does not correlate to the expected theoretical response (Figure 47) or the calculated theoretical h_{ps} (Figure 53a). The reason for the significantly lower readings from PPT 1 and PPT 2 can be attributed to the fine particles observed at the bottom of the strongbox after the test (Figure 42). During the 35g test some sample particles were inevitably expelled from the model. These particles may have been lodged inside the solenoid valves when they were closed. The solenoid valves could consequently not close completely and did not have a tight seal for the 70g test once the 35g test was completed. As a result, there was likely some flow taking place through the blocked solenoid valves while the sample was consolidating during the 70g test. Due to their proximity to the outlet valves, PPT 1 and 2 were most affected by this flow and their pore pressures did not reach the expected values. Consequently the measured h_{ps} values were considered to be unreliable and were not used.

6. Discussion

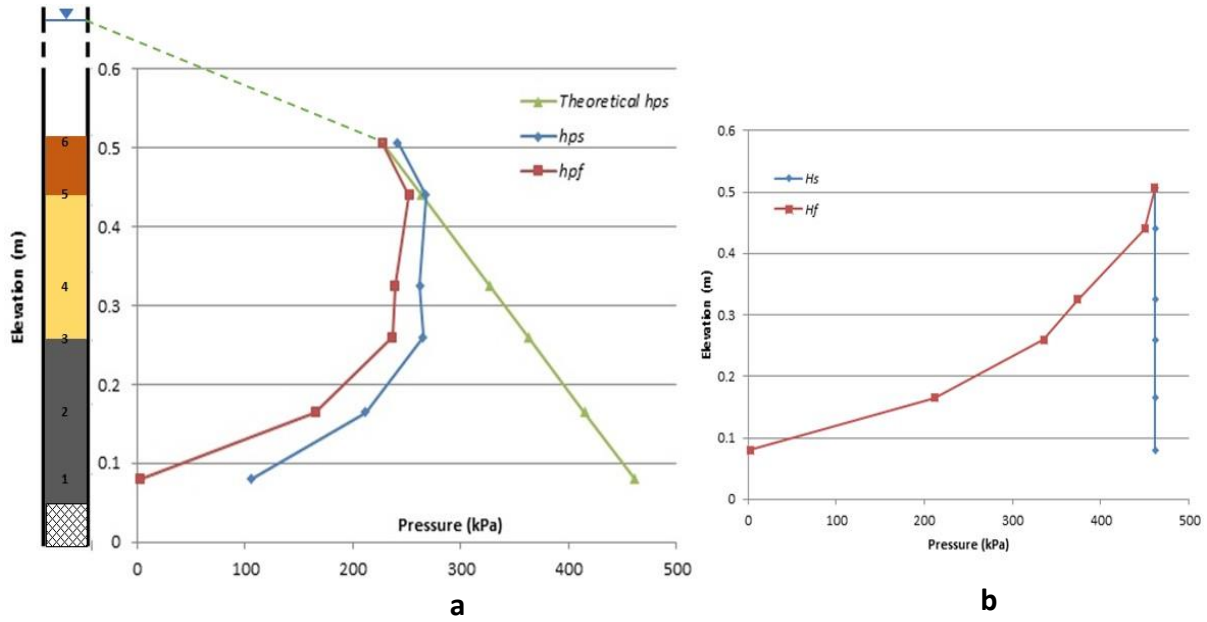


Figure 53: a) Distribution of the calculated theoretical h_{ps} , measured h_{ps} and h_{pf} and b) distribution of H_s and H_f at 70g.

When comparing the h_{pf} distribution of the 70g test to that of the 35g test (Figures 52a and 53a), it appears that the h_{pf} for the 70g test exhibits a similar response to the 35g test. When the valves are opened PPT 1 drops to the lowest pore pressure and PPT 5 now records the highest pore pressure. Therefore, with the exception of PPT 6, pore pressure decrease with depth. As with the correlation test, the steady state pore pressures suggest that there was no flow constriction at the outlet valves and that the test was freely draining. However, towards the end of the 70g test, the pore pressures of PPT1 and 2 started to increase slightly (Figure 39). This can again be attributed to soil particles gradually blocking the solenoid valves and slowing flow from the model slightly. As a result, the pore pressures at the bottom of the sample increased slightly. However, as illustrated by Figure 53b H_f still decreased with depth and downward flow was maintained through the column. This is likely due to the low permeability of the material ensuring that flow through the sample was slow enough to prevent any major flow constrictions at the outlet valves. The pore pressure response during steady state flow for the 70g test was similar to the theoretical response presented in Figure 48 and was used to assess the permeability and hydraulic behaviour of the model at 70g.

The steady state pore pressures (h_{pf}) and total head (H_f) distributions presented in Figures 52 and 53 provide further valuable insight to the hydraulic behaviour of each horizon in the sample at both 35g and 70g. For the 35g test the lower portion of the carbonaceous horizon (PPT 1 - 2) measures much lower pore pressures than the overlying horizons (Figure 52a). In the 70g test this is extended to the upper portion (PPT 2 - 3) and the carbonaceous horizon now measures pore pressures significantly lower than the overlying "softs" horizon (Figure 53a). As demonstrated by Figure 53a, this can be seen as the pore pressures rapidly decrease from the top to the bottom (PPT 3 - 1) of the carbonaceous horizon. Seepage from the overlying "softs" horizon is retarded at the interface with the carbonaceous horizon. As a result, pore pressures in the carbonaceous horizon decrease drastically as flow through the

6. Discussion

horizon interface is too slow to maintain higher pore pressures. This is supported by the distribution of H_f for both the 35g and 70g tests (Figures 52b and 53b). A steeper gradient for total head during flow (H_f) is indicative of a higher permeability. This allows the permeability of individual horizons to be compared and interpreted. In Figure 52b the gradient of H_f between PPTs 2 and 5 is much steeper than the gradient between PPTs 1 and 2 and the lower portion of the carbonaceous horizon has a lower permeability than the overlying upper portion (PPT 2 -3) and "softs" horizon. At 70g (Figure 53b) the gradient between PPT 2 and 3 is flattened out and the difference between the upper and lower portions of the carbonaceous horizon is less notable. However, there is now a more notable difference in gradient at the interface between the "softs" and carbonaceous horizons at PPT 3. Consequently, it appears that the carbonaceous horizon has a much lower permeability than the "softs" horizon.

In both the 35g and 70g tests h_{pf} in the top soil horizon increases with depth (Figures 52a and 53a). This increase can be explained by the layer of fine grained material that covered the top of the sample (Figure 43a) and the permeabilities of the top soil horizon itself and the underlying "softs" horizon. At increased gravitational accelerations in the centrifuge, this layer of fine grained material would have had a very low permeability. As a result thereof, flow from the water head to the top soil horizon was retarded by this layer. Also, as demonstrated by Figures 52b and 53b, the gradient of H_f is steepest between PPTs 5 and 6, suggesting that the top soil horizon had the highest permeability in the model. Consequently, seepage occurred faster through the top soil horizon than what it could be replaced by drainage from the overlying fine grained layer. This ensured that lower pore pressures were maintained at the top of the top soil horizon. In addition to this, the contact between the top soil and "softs" horizons may have further retarded downward seepage. As illustrated by Figures 52b and 53b, the gradient of H_f decreases between PPTs 5 and 3, indicating that the top soil is more permeable than the underlying "softs" horizon. Thus, seepage through the topsoil horizon occurred at a quicker rate than what it could drain into the "softs" horizon. This resulted in higher pore pressures being maintained at the interface between the two layers and an overall increase of h_{pf} from the top to the bottom of the top soil horizon.

When analysing the gradient of H_f (Figures 52b and 53b) for the "softs" horizon, it becomes apparent that the gradient changes at the interfaces between both the overlying top soil (PPT 5) and underlying carbonaceous (PPT 3) horizons. As established above, the gradient of H_f for the "softs" horizon (PPT 5 – 3) is less than the gradient of the top soil horizon, but greater than the gradient of the carbonaceous horizon. This suggests that the "softs" horizon is less permeable than the top soil horizon but more permeable than carbonaceous horizon. Consequently, the h_{pf} decreases slightly with depth in the "softs" horizon for both the 35g and 70g tests (as illustrated by Figures 52a and 53a). In summary, based on the measured H_f responses for both the 35g and 70g tests, it appears that the permeability of the sample decreases with depth. Furthermore, the accumulation of pore pressures (h_{pf}) at horizon interfaces suggests that vertical flow is somewhat retarded at these interfaces due to significant differences in material permeabilities.

6.3.3.2 Physical observations

The physical observations described in Section 5.3.3.3 are explained below and provide insight to the model behaviour during the test. The stratification of the sample in fine layers (Figure 41) was a result of the method used to place the sample into the cylinder. As the dry model material was placed directly into the deaired water, the larger particles settled first, followed by the smaller particles in the material. As this process was repeated it resulted in the stratification of the sample in layers of alternating coarse and fine grained material in each layer placed. The major concern associated with the stratification is that the fine layers in the sample would control the overall permeability of the sample. This becomes particularly evident at the interfaces between horizons. As described in the discussion above, seepage appears to be retarded at the horizon interfaces. This is likely due to a thicker layer of fine material accumulating at the top of each horizon while it was allowed to settle before the next horizon was placed on top of it (Section 4.3.6). The result is a reduction in the vertical hydraulic connectivity between the horizons in the sample as discussed above. However, despite the concerns, the sample stratification is reasoned to be somewhat representative of the heterogeneity in systematically graded end tipped backfill sequences, as illustrated by Figure 2.

The observations of Figures 43 and 44 are considered to be related to a single event. When settling/consolidating the excess pore water needs to be expelled from the sample. However, due to the reduction in vertical hydraulic connectivity between the horizons (due to lower permeability of the horizons), pore pressures build up within the sample. Under these conditions the effective stress would be very low and the material would consequently have very little strength. At a certain point, the excess pore pressure are suddenly dissipated during the liquefaction of the low permeability material (carbonaceous horizon). As the excess pore pressures are dissipated, the pore water is rapidly expelled from the bottom towards the top of the sample along the path of least resistance (vertically up along the inside of the cylinder and along the PPT cables). Evidence of this is displayed by the plume of carbonaceous material in Figure 44. This expulsion of the excess pore water was also thought to be responsible for the cloud of fine particles observed at the start of the 35g test and the observations illustrated in Figure 43. The forceful ejection of the excess pore water resulted in the crater like mound developing at the surface of the sample. When expelled, the excess pore water had entrained some of the finer sample material that was deposited into the water above the sample after being ejected. These fine particles resulted in the observed dark cloud of particles in the water head and the deposition of the layer illustrated in Figure 43a. As discussed in Section 6.3.3.1, this layer was associated with the increase of the measured h_{pf} with depth for the top soil horizon.

The cause of the cracks observed in Figure 45 is rather speculative and there is no single answer that definitively explains their presence at that specific position. A possible reason for their occurrence can be described by similar reasoning used to explain the anomalous behaviour of PPT 3 in Section 6.3.3.1. As it has been established that the top soil horizon is more permeable than the underlying horizons, it would have consolidated quicker, as mentioned above. This would have resulted in the build-up of effective stresses in this horizon and may have resulted in some horizontal dilation of the material. Consequently, some

6. Discussion

friction may have mobilised between the top soil material and the Perspex cylinder walls. This friction may have allowed the material to be held up somewhat while the rest of the sample was still consolidating below it. As a result the top soil horizon may have separated slightly from the rest of the sample along the contacts with cylinder wall, causing the isolated and irregular cracks seen in Figure 45. These cracks were likely only confined to the areas of the horizon interface that were in contact with the sidewalls, as the weight of the sample would have dragged it down towards the centre of the cylinder. Even if the horizons were completely separated, the effect would have been minimal, as the spaces would have been filled with water and all seepage would have been forced vertically down by the centrifugal acceleration and no seepage would have occurred parallel to the cracks. Although speculative, the reasons used to describe the formation of the cracks is considered to be logical and the impact of these cracks on the hydraulic behaviour of the sample has been demonstrated to be minimal. Therefore, the rate at which seepage occurred at the interface between the top soil and “softs” horizons was a function of the respective material permeabilities, irrespective of the presence or absence of cracks along the interface.

6.3.3.3 Model permeability

The interpretation of the h_{pf} and H_f responses discussed in Section 6.3.3.2, already gave an indication of the model permeability and how it changed throughout the sample. When analysing the data presented in Table 29, these interpretations are confirmed. For both the 35g and 70g tests the carbonaceous horizon had the lowest calculated permeability. Thereafter, the permeability increases with elevation and the greatest permeability was calculated for the top soil horizon. The permeability of the “softs” horizon was less than the top soil but greater than the carbonaceous horizons.

In total, the sample thickness was reduced by 139 mm due to consolidation settlement during the centrifuge tests. This total settlement was not distributed evenly among the three individual horizons. Also, the PSD and physical properties of each of the separate model materials differed significantly. Therefore, the calculated permeabilities can be associated with the material properties and recorded settlement of each horizon. Situated at the top of the model, the top soil horizon experienced the least amount of consolidation settlement. The horizon thickness only decreased by 4mm and the entire horizon appears to have moved down as the underlying horizons consolidated below it. Therefore, despite having a significant amount of fines (Table 7), the top soil maintained the lowest density throughout the tests. This was confirmed when the sample was removed from the cylinder. The top soil was the least compacted and easiest to remove from the cylinder. Due to the lower density, it is considered that the topsoil horizon maintained a greater void ratio throughout the test, which resulted in a higher permeability than the underlying “softs” and carbonaceous horizons. At the bottom of the model, the thickness of the carbonaceous horizon decreased by 56 mm and had the lowest permeability in the sample. Considering that the slurry and discard were combined for the model material (Section 4.3.4), the horizon contained a significant amount of fine material. Additionally, the slurry contained a high portion of soft coal fragments. At simulated prototype stresses in the centrifuge some of these fragments may have been crushed, thereby further increasing the amount of fines in the horizon. Consequently, there was a sufficient amount of fines to block the larger pore spaces and reduce the overall permeability of the carbonaceous

6. Discussion

horizon. On the other hand, the "softs" horizon experienced the most consolidation settlement but did not have the lowest permeability. This can be attributed to the greater proportion of sand in the "softs" material (Table 8). The combination of the sand and fine particles may have resulted in greater settlement due to the rearrangement of the fines between the sand particles. However, unlike the coal fragments of the carbonaceous horizon, the sand was composed of harder minerals that did not get crushed during the centrifuge tests. Consequently, the "softs" horizon retained a greater void ratio that resulted in a higher permeability than the carbonaceous horizon.

By conducting the full scale test at both 35g and 70g it afforded the opportunity to compare the model permeabilities at different states of consolidation. Although the amount of consolidation settlement for the 35g test cannot be confirmed, the dissipation of excess pore pressures indicates that the sample did indeed consolidate considerably during the test. Further consolidation settlement occurred when the model was accelerated to 70g, as there is once again the dissipation of excess pore pressures during the test. The effect of the state of consolidation can be noted in the calculated permeabilities. The calculated permeabilities for the 70g test are consistently lower than that calculated for the 35g test (Table 29). Therefore, the permeability decreases with increasing amounts of consolidation settlement, due to the overall densification of the sample.

Overall, the permeabilities calculated for the model at both 35g and 70g (Table 29) are low and seepage occurred very slowly through the model. It was noted that the interfaces between horizons retarded vertical flow and limited seepage from one horizon to the next. Therefore, the vertical permeability and hydraulic connectivity between individual horizons was low.

6.3.3.4 *Relating the model results to the prototype*

The aim of the investigation was to relate the results of the centrifuge model to the prototype backfill sequence it represents. In doing so the objective was to infer the permeability and hydraulic behaviour of the prototype based on the modelling results. As demonstrated by the control test, the permeabilities calculated from the centrifuge tests represent prototype permeabilities, as the permeability does not scale in the centrifuge when analysed correctly. Therefore, the permeabilities calculated from the centrifuge can be directly related to the prototype. However, as discussed in Section 6.3.2.2 the model needs to be an adequate representation of the prototype in order to relate the model results to the prototype. Consequently, the degree of similarity between the model and the prototype needs to be assessed before any interpretations of the prototype behaviour can be made from the modelling results.

To adequately represent the prototype, the model needed to simulate the geometry, and physical properties of the backfill sequence. Based on the assumptions discussed in Section 4.3.1 the interburden horizon was omitted from the backfill sequence and the prototype was simplified to three horizons with a combined thickness of 34 m. Using this geometry, a centrifuge model was developed. Based on the modelling height it was determined that an average acceleration of 56g would be needed to simulate prototype stresses in the model. To achieve this it was calculated that a centrifugal acceleration of 70g would be needed to achieve

6. Discussion

an average of 56g throughout the sample (Section 4.4.3). Therefore, it is considered that the centrifuge model provided an adequate representation of the backfill geometry and in-situ stresses at half scale (35g) and full scale (70g) tests in the centrifuge.

In terms of physical properties, the centrifuge model needed to simulate the material properties, structure, state of consolidation settlement and degree of saturation of the backfill sequence. Despite the material being prepared for the centrifuge model, care was taken to incorporate as much of the raw site material as possible. Where the PSD of the site material had been significantly altered due to the preparation processes, the material was logically argued to still represent the prototype (Section 6.1). To replicate the structure of the backfill at the site would require an in depth investigation to obtain field measurements that can be simulated in the model. As such values were not available for the investigation, the backfill structure at LCM was not clearly defined. However, as the backfill at LCM had been end tipped with haul trucks, it is reasonable to assume that the backfill may be partially systematically graded in layers of coarse and fine material as explained by Younger *et al.* (2000) (Figure 2). Therefore, the stratification of the sample in layers of fine and coarse material is considered to at least partially simulate the likely structure of the backfill prototype at LCM. The backfilling at the test site had been completed in the year 2000. Since then, the backfill would have undergone significant amounts of settlement and after 15 years it is reasonable to consider most of the settlement complete. However, settlement was not monitored and the backfill settlement state at LCM cannot be completely confirmed. In the centrifuge model, the backfill was allowed to completely consolidate at both 35g and 70g. Therefore, the centrifuge model represents the maximum consolidation settlement that can be experienced by the backfill, relative to the prototype stresses simulated by the level of acceleration in the centrifuge. Finally, the centrifuge model was completely saturated during the tests. The position of the water table in the backfill could not be confirmed and the extent of backfill saturation was not known. As the groundwater is still currently being drawn down for the current mining operations, groundwater rebound is likely to be minimal and the backfill is most probably sparsely and variably saturated. Consequently, the permeabilities calculated from the centrifuge model are representative of a backfill sequence that is completely saturated. As the entire backfill is unlikely to ever be completely saturated, the model permeabilities are considered to represent the maximum saturated permeability of the backfill.

The differences discussed above, leads to certain limitations when comparing the model results to the prototype. With the geometry, material properties and structure of the prototype considered to be adequately simulated by the centrifuge model, it is only the degree of settlement and saturation in the prototype that become questionable. However, once the mine has closed and the groundwater has rebounded, the degree of saturation will inevitably increase. Furthermore, additional collapse settlement is often associated with the reestablishment of the water table in the backfill (Section 2.2.2.). Under these conditions the model is thought to more accurately represent the permeability and hydraulic behaviour of the backfill sequence. The results of the centrifuge model should therefore be related to the long term behaviour of the prototype backfill sequence.

The limitations of the centrifuge model have been described above and allow for a better understanding of how to relate the model results to the prototype. Despite these limitations, the model results provided valuable insight into the long term behaviour of the backfill. Relating the model results to the prototype, several predictions of the long-term backfill behaviour can be made. Based on the interpretation of the model results in Sections 6.3.3.1 to 6.3.3.3, the permeability of the backfill is likely to decrease over time due to the overall reduction in void ratio as the backfill settles. Furthermore, the permeability of the backfill sequence has been demonstrated to decrease with depth. The highest permeabilities were calculated at the top and the lowest at the bottom of the backfill. This is in contrast to what has been described by Ferguson (1984) and Younger *et al.* (2000). Due to the carbonaceous horizon being more coarsely graded and the higher fines content of the top soil, one would expect the permeability to increase with depth. This may be the case directly after the backfill has been placed. However, crushing of softer coal fragments in the carbonaceous horizon is likely to reduce the permeability over time. Finally, the vertical permeability between the horizons is expected to be very low. A combination of contrasting material properties and accumulations of finer material at the interfaces between horizons results in poor vertical hydraulic connectivity between the horizons. Consequently, when vertical seepage intersects a horizon interface it is likely to be diverted laterally along the interface. This could potentially lead to concentrated flow at these boundaries that may eventually lead to piping along the horizon interfaces over time.

6.3.5. Summary

The results of three centrifuge test have been interpreted. The control test provided valuable insight to the modelling methodology. It was demonstrated that permeability is a material parameter that is not scaled in the centrifuge when interpreted correctly. Instead, it was determined that the hydraulic gradient is increased N times and that the calculated permeabilities from the centrifuge model were representative of prototype values. The comparison of the correlation test permeabilities to the field percolation tests did not provide a meaningful correlation. However, the calculated permeabilities were within the expected range for the material and the test methodology displayed significant potential for simulating prototype conditions. The full scale tests provided the opportunity to simulate and interpret the behaviour of a preselected prototype backfill sequence. From the results it was demonstrated that the model was an adequate representation of a completely saturated and settled backfill prototype. Consequently, the model results were related to the long term behaviour of the backfill. It was demonstrated that over time the backfill permeability will decrease and the bottom of the backfill sequence is likely to have the lowest permeability. Furthermore, the vertical permeability between the horizons was very low and lateral flow was thought to dominate at the boundaries between horizons in an actual backfill profile.

7. Conclusions

With the aim of developing a small scale centrifuge model to replicate the permeability and hydraulic behaviour of a heterogeneous coal mine backfill sequence, an extensive literature review was conducted. The basic concepts of fluid mechanics in porous media have been discussed and an overview of seepage flow and the associated formulae and laws was presented. To better understand the relationship between the settlement and hydraulic behaviour of opencast backfill, the mechanisms of backfill settlement were discussed and the typical hydraulic behaviour was assessed. Furthermore, a detailed overview of centrifuge modelling was presented. The basic concepts associated with centrifuge modelling were discussed and the fundamental scaling laws and modelling principles were outlined. Water flow in a centrifugal field was discussed and the associated scaling laws were presented. The opposing views of whether it is the hydraulic gradient or the permeability that is scaled in the centrifuge was investigated. Based on the reviewed literature, it was determined that it is currently accepted that the permeability is scaled N times in the centrifuge. Finally, the modelling of permeability in the centrifuge was investigated and the reviewed case studies provided valuable insight to the aim of the current investigation and aided in the approach to developing a functional and representative centrifuge model.

To develop a centrifuge model, Leeupan coal mine (LCM) was selected as an appropriate study area. The climate and surface water drainage and regional geology and hydrogeology of the area was subsequently described. The geometry and material properties of the backfill at LCM were characterised and a prototype backfill sequence was defined based on these characteristics. Based on the falling head centrifuge model of Singh and Gupta (2000) and the geometry of the defined backfill prototype, the centrifuge model was developed. Material for each of the respective horizons in the centrifuge model was sampled from LCM and prepared for the centrifuge model. Percolation tests were conducted to establish an in-situ permeability for the backfill material for comparison to an analogous centrifuge model. To measure the permeability of the model, small pore pressure transducers were placed at known distances from each other at discrete positions in the sample. Using the measured volumetric discharge, the cross-sectional area of the sample and distance between each pore pressure transducer, the measured pore pressures were used to calculate the permeability of the sample between any two transducers in the sample. Furthermore, the investigation outlined the construction of the centrifuge model, the configurations of the three centrifuge tests and the analysis methods used to calculate the permeabilities and required centrifugal accelerations.

To determine the effects of material preparation the grading curves of the site and model material were compared. It was demonstrated that there had been an overall reduction in the gravel content and increase in the sand and silt content for the prepared model material. Despite these differences, the model material was shown to still be an adequate representation of the prototype material. Consequently, it was reasonable to assume that the hydraulic behaviour of the material was minimally affected by the material preparation.

7. Conclusions

To validate the test methodology and assess the scaling law for permeability in the centrifuge a control test was conducted at 1g and a centrifugal acceleration of 23g. The calculated model permeability was well within the expected range for the control test material and the test methodology was considered to be accurate and reliable. The permeabilities calculated for the two tests were compared and only differed by the slightest of margins. The permeability for the 1g test was on average only 1.233 times greater than the permeability of the 23g test. The slight decrease in calculated permeability at 23g was attributed to the densification of the sample at elevated acceleration in the centrifuge. Additionally, by measuring the pore pressures in the model it was demonstrated that the pressure head is increased N times in the centrifuge. Based on these results it was concluded that the permeability is a material parameter that is not scaled N times in the centrifuge. Instead, as the pressure head is increased N times and the flow path length is condensed N times in the model, it is the hydraulic gradient that is increased N times in the centrifuge. Therefore, the permeabilities calculated with the centrifuge model could be directly related to the prototype it represents without the need to be downscaled.

The correlation test was composed of material sampled from the percolation test auger holes and was configured to represent the "softs" horizon where the percolation tests were conducted. To assess the reliability of the centrifuge methodology in simulating the field conditions, the results of the correlation test were compared to the percolation test permeabilities. The centrifuge appeared to under estimate the permeability and the calculated average of the percolation tests was two orders of magnitude greater than the calculated centrifuge average. However, the accuracy of the percolation tests was questioned and it was considered that the percolation tests most likely overestimated the material permeability because of assumptions on the degree of material saturation, inherent material bias and disturbances caused by the test methodology. Furthermore, the sample in the centrifuge test was completely saturated and consolidated and represented the full thickness of the "softs" horizon. As the percolation tests were only conducted in the uppermost portion of the horizon and saturation during these test is questionable, the percolation test values are not considered to represent the same prototype simulated by the centrifuge model. Therefore, it was concluded that the model reliability could not be meaningfully interpreted through the comparison of the correlation test results and the percolation test permeability.

The results of modelling the full scale profile presented the opportunity for the interpretation of the backfill permeability and hydraulic behaviour at centrifuge accelerations of 35g (half scale) and 70g (full scale) respectively. The recorded pore pressures and calculated permeabilities for each test were compared and interpreted. Irrespective of the level of acceleration, the highest permeability was calculated for the top soil horizon. Despite having a large portion of fine particles, the top soil experienced the least amount of consolidation settlement and maintained a greater void ratio throughout the tests. The lowest permeability was calculated for the carbonaceous horizon for both the 35g and 70g tests. The horizon had consolidated significantly during the tests and it is believed that the void ratio was significantly reduced by the crushing of soft coal fragments in this horizon.

7. Conclusions

During steady state flow, there was a notable decrease in pore pressures below each horizon interface. It is believed that due to the retardation of flow at the interfaces, water is drained faster through each horizon than what is replaced at horizon interfaces. This was confirmed through the interpretation of the gradient of the total head during flow (H_i). Consequently, the vertical hydraulic connectivity between each horizon in the backfill is considered to be poor.

At each level of acceleration a greater degree of backfill settlement was simulated. The effect of settlement on the permeability of the backfill could be interpreted through the comparison of the permeabilities calculated at 35g and 70g respectively. The permeabilities for the 70g test are consistently lower than those calculated for the 35g test. Therefore, the permeability of the backfill decreases with increasing amounts of consolidation settlement, due to the overall densification of the sample.

The model material was completely saturated and settled during the test, however the degree of saturation and settlement in the prototype could not be confirmed. Consequently, it was considered that the centrifuge model best represented the long-term permeability and hydraulic behaviour of the backfill prototype. The results of the centrifuge model were used to make reasonable predictions on the permeability and hydraulic behaviour of the backfill. The modelling results suggested that the permeability of the backfill is likely to decrease over time due to an overall reduction in void ratio as the backfill settles. The upper portions of the backfill are likely to experience less settlement than the underlying horizons and are expected to maintain a higher permeability. Over time the larger coal fragments in the carbonaceous horizon are expected to be crushed and reduced to finer particle sizes as the backfill settles. As a result, the bottom of the backfill sequence is expected to have the lowest permeability after the backfill has settled completely. The contrasting material properties and accumulations of finer material at horizon interfaces are expected to result in poor vertical permeability between the horizons in the backfill sequence. As a result, lateral seepage is likely to be concentrated along the horizon interfaces and may lead to piping of the backfill over time.

With the geometry and material properties of the backfill adequately replicated, the centrifuge provided a means of replicating the prototype stress distribution and the model was considered to be a reasonable representation of the prototype backfill sequence. Furthermore, the centrifuge decreased the test time dramatically. The applied centrifugal force ensured that the long term settlement was rapidly simulated and that flow through the low permeability backfill material was accelerated during the tests. Overall, the centrifuge methodology provided a unique means of modelling the long term permeability and hydraulic behaviour of the backfill sequence.

8. References

- Barry, D.A., Lisle, I.G., Li, L., Prommer, H., Parlange, J.-Y., Sander, G.C., Griffioen, J.W., (2001), *Similitude applied to centrifugal scaling of unsaturated flow*, Water Resources Research, (37), pp 2471-2479.
- Basha, H.A. and Mina, N.I., (1999), Estimation of the unsaturated hydraulic conductivity from the pressure distribution in a centrifugal field, Water Resources Research, (35), pp 469-477.
- Bear, J., (1988), Dynamics of fluid flow in porous media, Chapter 3: *Pressure and piezometric head*, Dover Publications, New York, pp 59-64.
- Charles, J.A., Hughes, D.B., Burford, D., (1984), *The effect of a rise of water table on the settlement of backfill at Horsley restored opencast coal mining site, 1973 -1983*, Third Conference on Large Ground Movements and Structures, University of Wales Institute of Science and Technology, Cardiff, pp 423-442.
- Chikatamarla, R., Laue, J., Springman, S.M., (2006), *Centrifuge scaling laws for guided free fall events including rock falls*, International Journal of Modelling in Geotechnics, (2), pp 15-26.
- Culligan-Hensley, P.J. and Savvidou, C., (1995), *Environmental geomechanics and transport processes*, In: Taylor, R.N., Geotechnical centrifuge technology (Ed.), Blackie Academic and Professional, Glasgow, pp 196-264.
- Day, P. and Wardle, G., (1996), *Effect of water on settlement of opencast pit backfill: case histories of investigation and performance*, SAICE seminar on hydrology of made ground, Johannesburg, pp -8.
- Dell' Avanzi, E. and Zornberg, Z.G., (2002), *Scale factors for centrifuge modelling of unsaturated flow*, In: Jucá, J.F.T., de Campos, J.M.P., Marinho, F.A.M. (Eds.), Unsaturated soils, Vol. 1, A.A. Balkema Publishers, Lisse, pp 425-430.
- Dippenaar, M.A., van Rooy, J.L., Breedt, N., Huisamen, A., Muravha, S.E., Mahlangu, S., Mulders, J.A., (2014), *Vadose zone hydrology: Concepts and techniques*, WRC Report No. TT584/13, pp 83-84.
- Duncan, A.R. and Marsh, J.S. (2006). *The Karoo igneous province*. In: Johnson, M.R., Anhaeusser, C.R. and Thomas, R.J. (Eds.). The Geology of South Africa. The Geological Society of South Africa. Johannesburg/Council for Geoscience. Pretoria. pp 501—520.
- Eriksson, P.G., Altermann, W., Hartzler, F.J. (2006). *The Transvaal Supergroup and its precursors*. In: Johnson, M.R., Anhaeusser, C.R. and Thomas, R.J. (Eds.). The Geology of South Africa. The Geological Society of South Africa. Johannesburg/Council for Geoscience. Pretoria. pp 237—260
- Ferguson D., (1984), *Reclaimed and backfilled areas*, Third Conference on Large Ground Movements and Structures, University of Wales Institute of Science and Technology, Cardiff, pp 443-462.

8. References

- Fetter, C.W., (2001), Applied hydrogeology, 4th Ed., Chapter 4: *Principles of groundwater flow*, Prentice-Hall, Upper Saddle River, pp 113-124.
- Gamerding, A.P. and Kaplan, D.I., (2000), *Application of continuous-flow centrifugation method for solute transport in disturbed, unsaturated sediments and illustration of mobile-immobile water*, Water Resources Research, (36), pp 1747-1755.
- Garnier, J., Gaudin, C., Springman, S.M., Culligan, J.P., Goodings, D., Konig, D., Kutter, B., Phillips, R., Randolph, M.F., Thorel, L., (2007), *Catalogue of scaling laws and similitude questions in geotechnical centrifuge modelling*, International Journal of Physical Modelling in Geotechnics, (3), pp -23
- Grobbelaar, R., Usher, B., Cruywagen, L.M., de Necker, E., Hodgson, F.D.I. (2004). *Long-term impact of intermine flow from collieries in the Mpumalanga coalfields*. WRC Report No. 1056/1/04. pp 11-15.
- Gaudin, C., White, D.J., Boylan, N., Breen, J., Brown, T. and De Catania, S. 2010. *A miniature high speed data acquisition system for geotechnical centrifuges*. Proceedings of 7th International Conference on Physical Modelling in Geotechnics 2010, Zurich, Switzerland, Taylor & Francis Group, London, 229 - 234.
- Hills, C.W.W., (1994), *The examination and prediction of opencast backfill settlement*, PhD thesis, University of Nottingham, <http://etheses.nottingham.ac.uk/1501/>, pp -264.
- Jacobsz, S.W., (2013), *Centrifuge modelling of a soil nail retaining wall*, Journal of the South African Institution of Civil Engineers, (55), pp 85-93.
- Jacobsz, S.W., Kearsley, E.P., Kock, J.H.L., (2014), *The geotechnical centrifuge facility at the University of Pretoria*, To be published.
- Johnson, M.R., van Vuuren, C.J., Visser, J.N.J., Cole, D.I., de V. Wickens, H., Christie, A.D.M.m., Roberts, D.L., Brandl, G. (2006). *Sedimentary rocks of the Karoo Supergroup*. In: Johnson, M.R., Anhaeusser, C.R. and Thomas, R.J. (Eds.). The Geology of South Africa. The Geological Society of South Africa. Johannesburg/Council for Geoscience. Pretoria. pp 461—499.
- Jones, B.R., (2014), *Geotechnical centrifuge modelling of the behaviour of a compressible clay horizon underlying a reinforced sand foundation*, MSc Thesis, University of Pretoria, pp-93
- Joseph, P.G. and Einstein, H.H., (1988), *Rock modelling using the centrifuge*, Massachusetts Institute of Tech., Dept. of Civil Engineering, Report Nr. ESL-TR-87-22, pp -50.
- Kenny, T.C., Lau, D., Ofoegbu, G.I., (1984), *Permeability of compacted granular materials*, Canadian Geotechnical Journal, (21), pp 726-729.
- Knappette, J.A. and Craig, R.F., (2012), *Craig's soil mechanics*, 8th Ed., Chapter 2: *Seepage*, Spon Press, Oxon, pp 39-78.
- Kruger, A.C., (2004), *Climate of South Africa, climate regions*, WS45, South African Weather Service, Pretoria, South Africa.

8. References

- Le Roux, P., (2012), Soil suction in platinum tailings, Unpublished Beng project report, University of Pretoria.
- MaCarthy, T.S. (2006). *The Witwatersrand Supergroup*. In: Johnson, M.R., Anhaeusser, C.R. and Thomas, R.J. (Eds.). *The Geology of South Africa*. The Geological Society of South Africa. Johannesburg/Council for Geoscience. Pretoria. pp 237-260.
- Nakajima, H. and Stadler, A.T., (2006), *Centrifuge modelling of one-step outflow tests for unsaturated parameter estimations*, Hydrogeology and Earth System Sciences, (10), pp 715–729.
- Nimmo, J.R., Rubin, J., Hammermeister, D.P., (1987), *Unsaturated flow in a centrifugal field: measurement of hydraulic conductivity and testing of Darcy's law*, Water Resources Research, (23), pp 124-134.
- Nimmo, J.R., (1990), *Experimental testing of transient unsaturated flow theory at low water content in a centrifugal field*, Water resource research, (26), pp 1951-1960.
- Nimmo, J.R. and Mello, K.A., (1991), *Centrifugal techniques for measuring saturated hydraulic conductivity*, Water Resources Research, (27), pp 1263-1269.
- Nimmo, J.R., Akstin, K.C., Mello, K.A., (1992), *Improved apparatus for measuring hydraulic conductivity at low water content*, Soil Science Society of America Journal, (56), pp1758-1761.
- Nimmo, J.R., Stonestrom, D.A., Akstin, K.C., (1994), *The feasibility of recharge rate determination using the steady state centrifuge method*, Soil Science Society of America Journal, (58), pp149-56.
- Pietersen, K., Beekman, H.E., Holland, M., (2011), *South African groundwater governance case study*, WRC Report No. KV 27311, pp 39-46.
- Robinson, R.G., (2002), *Modelling hydraulic conductivity in a small centrifuge: Discussion¹*, Canadian Geotechnical Journal, (39), pp 486-487.
- Singh, N. and Gupta, A.K., (2000), *Modelling hydraulic conductivity in a small centrifuge*, Canadian Geotechnical Journal, (37), pp 1150-1154.
- Singh, N. and Gupta, A.K., (2002), *Modelling hydraulic conductivity in a small centrifuge: Reply¹*, Canadian Geotechnical Journal, (39), pp 488-489.
- Simuneuk, J. and Nimmo, J.R., (2005), *Estimating soil hydraulic parameters from transient flow experiments in a centrifuge using parameter optimization technique*, Water Resources Research, (41),W04015, pp-9
- SANS [South African National Standards]. (1993). *Code of practice: Water supply and drainage for buildings. Part 2: Drainage installations for buildings*. SANS 10252-2. South African Bureau of Standards. Pretoria.
- SPI [Standard Practice Instruction]. (2014). *Procedure to maintain slope stability*. Leeuwan Coal Mine. Exxaro Resources Ltd. Pretoria.

8. References

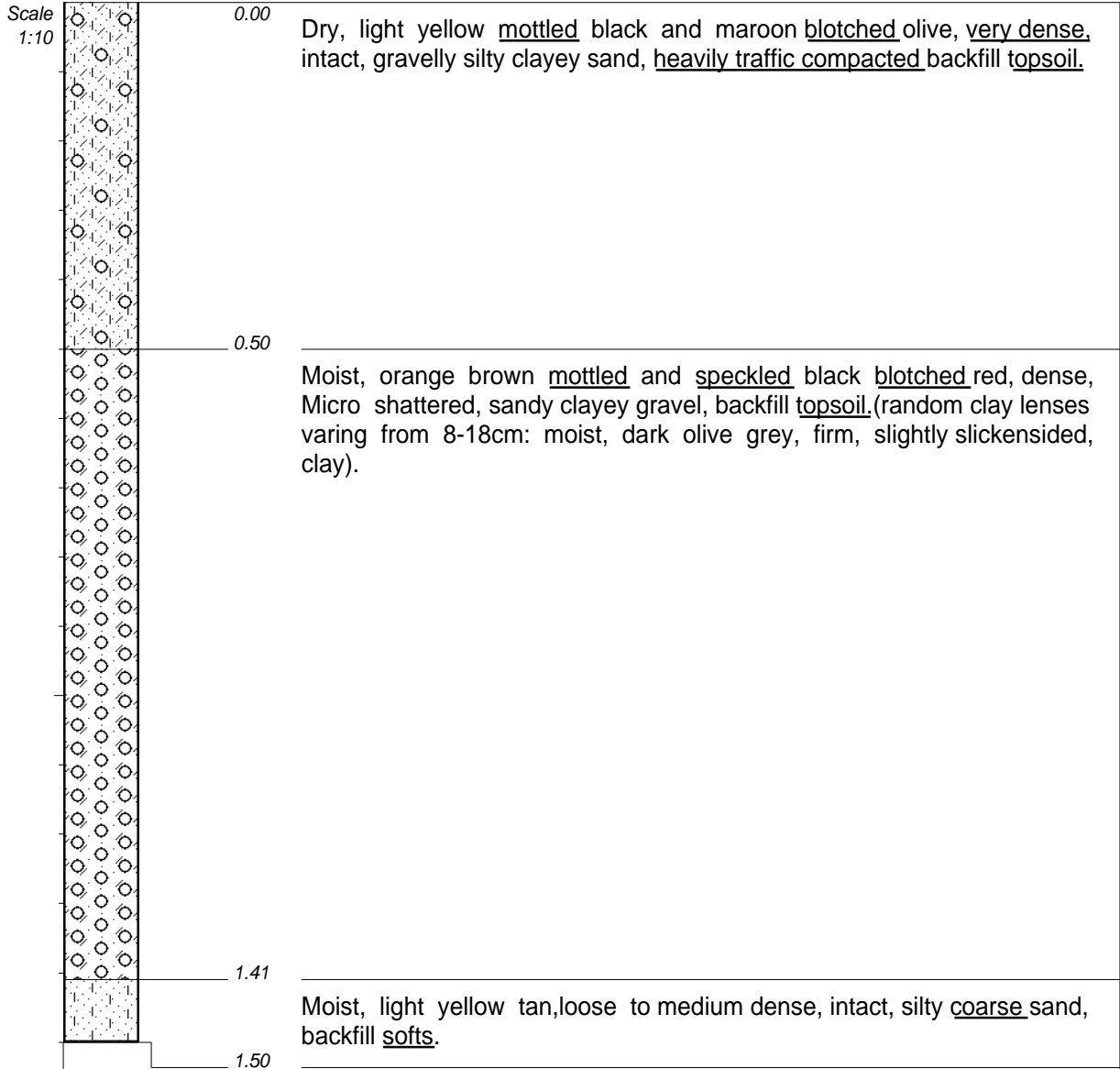
- Taylor, R.N. (1995), *Centrifuges in modelling: principles and scale effects*, In: Taylor, R.N. (Ed.), *Geotechnical centrifuge technology*, Blackie Academic and Professional, Glasgow, pp 19-34.
- Thusyanthan, N.I. and S.P.G.Madabhushi, S.P.G., (2003), *Scaling of seepage flow velocity in centrifuge models*, Cambridge University Engineering Department, Report Nr, CUED/D-SOILS/TR326, pp -12.
- van Rooyen, J. (2014). *Leeuwpans colliery hydrogeological investigation*. Report compiled by GCS, 63 Wessels Road, Rivonia, South Africa. pp 16-32.
- Younger, P.L., Banwart, S.A., Hedin, R.S., (2002), *Mine water: hydrology, pollution, remediation*, Springer Science + Business Media, Dordrecht, pp 29-48 and 218-226.
- Zornberg, J.G. and McCartney, J.S., (2010), *Centrifuge permeameter for unsaturated soils. 1: theoretical basis and experimental developments*, *Journal of Geotechnical and Geoenvironmental Engineering*, (136), pp 1051-1063.



Appendix

Photograph of the test pit sidewall profile





NOTES

- 1) Test pit stopped at 1.5m due to mine health and safety regulations.
- 2) Four bulk samples taken of softs material from auger holes drilled at the bottom of the testpit.

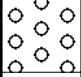

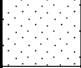



CONTRACTOR :
MACHINE :
DRILLED BY :
PROFILED BY : Warren van Tonder
TYPE SET BY :
SETUP FILE : STANDARD.SET

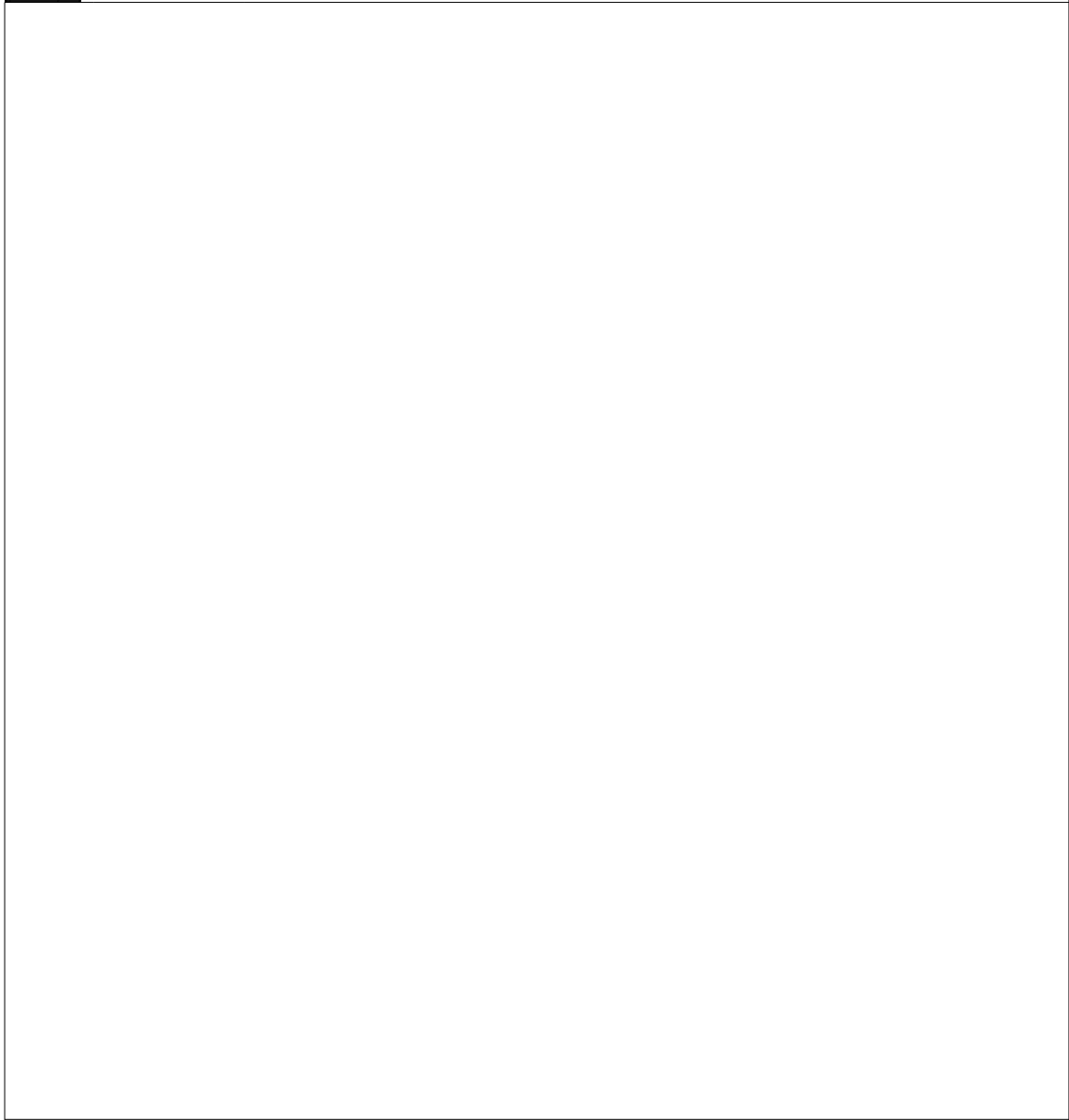
INCLINATION :
DIAM :
DATE :
DATE : 24/06/2014
DATE : 10/07/2014 12:34
TEXT : ..ktop\TestPitLeeuwpan.txt

ELEVATION :
X-COORD : 2896339.253
Y-COORD : 26806.117

HOLE No: TP01
Leeuwpan Coal Mine, Delmas, Mpumalanga



	GRAVEL	{SA02}
	GRAVELLY	{SA03}
	SAND	{SA04}
	SANDY	{SA05}
	SILTY	{SA07}
	CLAYEY	{SA09}



CONTRACTOR :
MACHINE :
DRILLED BY :
PROFILED BY :

INCLINATION :
DIAM :
DATE :
DATE :

ELEVATION :
X-COORD :
Y-COORD :

TYPE SET BY :
SETUP FILE : STANDARD.SET

DATE : 10/07/2014 12:34
TEXT : ..ktop\TestPitLeeuwpan.txt

Percolation Test Data

Test 1

Test 1: Measured time for each 10 mm of drawdown for three test runs.

Drawdown	Time 1 (seconds)	Time 2 (seconds)	Time 3(seconds)
0mm	0	0	0
10mm	592	557	545
20mm	1122	1095	1111
30mm	1653	1658	1698
40mm	2169	2198	2259
50mm	2752	2800	2879

Test 1: Calculated discharge for each test run.

Drawdown	Discharge 1(mm ³ /s)	Discharge 2(mm ³ /s)	Discharge3(mm ³ /s)
10mm	298.504	317.261	324.27
20mm	315	322.766	318.118
30mm	320.716	319.749	312.217
40mm	325.891	321.592	312.908
50mm	321.066	315.562	306.903

Test 1: Calculated permeability for each test run

Drawdown	K-1(mm/s)	K-2(mm/s)	K-3(mm/s)
10mm	0.01689	0.01795	0.01835
20mm	0.01783	0.01827	0.018
30mm	0.01815	0.01809	0.01767
40mm	0.01844	0.0182	0.01771
50mm	0.01817	0.01786	0.01737
Average	0.017896	0.018074	0.01782

Test 2

Test 2: Measured time for each 10 mm of drawdown for three test runs.

Drawdown	Time 1 (seconds)	Time 2 (seconds)	Time 3 (seconds)
0mm	0	0	0
10mm	453	427	451
20mm	888	841	903
30mm	1350	1298	1366
40mm	1790	1757	1848
50mm	2198	2210	2293

Test 2: Calculated discharge for each test run.

Drawdown	Discharge 1(mm ³ /s)	Discharge 2(mm ³ /s)	Discharge3(mm ³ /s)
10mm	390.098	413.852	391.828
20mm	398.006	420.249	391.394
30mm	392.699	408.431	388.099
40mm	394.893	402.31	382.499
50mm	401.99	399.807	385.335

Test 2: Calculated permeability for each test run.

Drawdown	K-1(mm/s)	K-2(mm/s)	K-3(mm/s)
10mm	0.02208	0.02342	0.02217
20mm	0.02252	0.02378	0.02215
30mm	0.02222	0.02311	0.02196
40mm	0.02235	0.02277	0.02165
50mm	0.02275	0.02263	0.02181
Average	0.022384	0.023142	0.021948

Test 3

Test 3: Measured time for each 10 mm of drawdown for four test runs.

Drawdown	Time 1 (seconds)	Time 2 (seconds)	Time 3 (seconds)	Time 4 (seconds)
0mm	0	0	0	0
10mm	67	86	93	85
20mm	141	169	178	162
30mm	224	257	268	249
40mm	305	338	367	345
50mm	383	424	457	436

Test 3: Calculated discharge for each test run.

Drawdown	Discharge 1(mm ³ /s)	Discharge 2(mm ³ /s)	Discharge 3(mm ³ /s)	Discharge 4(mm ³ /s)
10mm	2637.531	2054.821	1900.157	2078.995
20mm	2506.59	2091.297	1985.557	2181.662
30mm	2366.713	2062.816	1978.148	2129.091
40mm	2317.568	2091.297	1926.045	2048.865
50mm	2306.979	2083.898	1933.42	2026.543

Test 3: Calculated permeability for each test run.

Drawdown	K-1(mm/s)	K-2(mm/s)	K-3(mm/s)	K-4(mm/s)
10mm	0.14925	0.11628	0.10753	0.11765
20mm	0.14184	0.11834	0.11236	0.12346
30mm	0.13393	0.11673	0.11194	0.12048
40mm	0.13115	0.11834	0.10899	0.11594
50mm	0.13055	0.11793	0.10941	0.11468
Average	0.137344	0.117524	0.110046	0.118442

Test 4

Test 4: Measured time for each 10 mm of drawdown for three test runs.

Drawdown	Time 1 (seconds)	Time 2 (seconds)	Time 3 (seconds)
0mm	0	0	0
10mm	552	570	560
20mm	1081	1099	1130
30mm	1640	1690	1664
40mm	2168	2209	2192
50mm	2705	2778	2747

Test 4: Calculated discharge for each test run.

Drawdown	Discharge 1(mm ³ /s)	Discharge 2(mm ³ /s)	Discharge3(mm ³ /s)
10mm	320.135	310.026	315.562
20mm	326.947	321.592	312.769
30mm	323.258	313.695	318.596
40mm	326.042	319.99	322.472
50mm	326.644	318.061	321.65

Test 4: Calculated permeability for each test run.

Drawdown	K-1(mm/s)	K-2(mm/s)	K-3(mm/s)
10mm	0.01812	0.01754	0.01786
20mm	0.0185	0.0182	0.0177
30mm	0.01829	0.01775	0.01803
40mm	0.01845	0.01811	0.01825
50mm	0.01848	0.018	0.0182
Average	0.018368	0.01792	0.018008